

# APPLICATION OF ODT TO TURBULENT COMBUSTION PROBLEMS IN INCOMPRESSIBLE AND COMPRESSIBLE REGIMES

Von der Fakultät für Maschinenbau, Elektro- und Energiesysteme der Brandenburgischen Technischen Universität Cottbus-Senftenberg zur Erlangung des akademischen Grades eines

Doktors der Ingenieurwissenschaften  
(Dr.-Ing.)

genehmigte Dissertation vorgelegt von

Master of Science  
Zoltan Jozefik

geboren am 16.07.1981 in Budapest, Ungarn

Vorsitzender	Prof. Dr.-Ing. Ennes Sarradj	BTU Cottbus-Senftenberg
Gutachter	Prof. Dr.-Ing. Heiko Schmidt	BTU Cottbus-Senftenberg
Gutachter	Prof. Dr.-Ing. Christian O. Paschereit	TU Berlin

Tag der mündlichen Prüfung: 10. Mai 2016



APPLICATION OF ODT TO TURBULENT COMBUSTION PROBLEMS IN  
INCOMPRESSIBLE AND COMPRESSIBLE REGIMES

MSC ZOLTAN JOZEFIK

University:

Brandenburg University of Technology Cottbus-Senftenberg

Faculty:

Mechanical Engineering, Electrical and Energy Systems

Department:

Chair of Numerical Fluid and Gasdynamics

MSc Zoltan Jozefik:

*Application of ODT to turbulent combustion problems in incompressible and compressible regimes,*

© May 2016

CHAIR OF SUPERVISORY COMMITTEE:

Prof. Dr.-Ing. Ennes Sarradj

SUPERVISORS:

Prof. Dr.-Ing. Heiko Schmidt

Dr. rer. nat. Alan R. Kerstein

REVIEWERS:

Prof. Dr.-Ing. Heiko Schmidt

Prof. Dr.-Ing. Christian O. Paschereit

LOCATION:

Cottbus

TIME FRAME:

May 2016

## ABSTRACT

---

The one-dimensional turbulence (ODT) model is applied to a reactant - to - product counterflow configuration as well as to a shock tube configuration in non-reactive flow and in deflagration and detonation regimes. The model employed herein solves conservation equations for momentum, energy, and species on a one dimensional (1D) domain corresponding to the line spanning the domain between nozzle orifice centers in the counterflow configuration and corresponding to the tube length in the shock tube configuration. The effects of turbulent mixing are modeled via a stochastic process, while the Kolmogorov and reactive length and time scales are explicitly resolved.

In the counterflow configuration, comparisons between model and DNS results for spatial mean and root-mean-square (RMS) velocity, temperature, and major and minor species profiles are shown. The ODT approach shows qualitatively and quantitatively reasonable agreement with the DNS data. Scatter plots and statistics conditioned on temperature are also compared for heat release rate and all species. ODT is able to capture the range of results depicted by DNS. However, conditional statistics show signs of underignition.

To carry out the shock tube simulations, the ODT methodology is extended to include an efficient compressible implementation and a model for capturing shock-induced turbulence is presented. The necessary algorithmic changes to include compressibility effects are highlighted and the model for capturing shock-turbulence interaction is presented. To validate the compressible solver, results for Sod's shock tube problem are compared against a finite volume Riemann solver. To validate the model for shock-turbulence interaction, comparisons for a non-reactive and a reactive case are presented. First, results of a shock traveling from light (air) to heavy ( $\text{SF}_6$ ) with reshock have been simulated to match mixing width growth data of experiments and turbulent kinetic energy results from LES. Then, for one-step chemistry calibrated to represent an acetylene/air mixture, the interaction of a shock wave with an expanding flame front is simulated, and results with 2D simulation (2D-sim) data for flame brush formation and ensuing deflagration-to-detonation transitions (DDT) are compared. Results for the Sod shock tube comparison show that the shock speed and profile are captured accurately. Results for the non-reactive shock-reshock problem show that interface growth at all simulated Mach numbers is captured accurately and that the turbulent kinetic energy agrees in order of magnitude with LES data. The reactive shock tube results show that the flame brush thickness compares well to 2D-sim data and that the approximate location and timing of the DDT can be captured. The known sensitivity of DDT characteristics to details of individual flow realizations, seen also in ODT, implies that model agreement can be quantified only by comparing flow ensembles, which are presently unavailable other than in an ODT run-to-run sensitivity study that is reported herein.

## ZUSAMMENFASSUNG

---

Das one-dimensional turbulence (ODT) Modell wird für die Simulation (1) eines Gegenstrom-Systems, in dem eine von links kommende Strömung mit unverbrannten Reaktanten auf eine von rechts kommende Strömung mit verbrannten Reaktionsprodukten trifft, und (2) einer nicht reaktiven und reaktiven Stoßrohr-Konfiguration angewendet. Hierbei werden Gleichungen für Impuls, Energie und Spezies auf einer 1D Linie durch das Strömungsgebiet gelöst, die der Mittellinie zwischen den beiden Düsen in der Gegenstrom-Konfiguration bzw. der Mittellinie des Rohres in der Stoßrohr-Konfiguration entspricht. Die turbulente Mischung der großen Skalen ist durch einen stochastischen Ansatz modelliert, während die kleinsten physikalischen Skalen, Kolmogorov-Skalen, sowie die reaktiven Längen- und Zeitskalen explizit aufgelöst sind.

Die ODT-Ergebnisse für die Gegenstrom-Konfiguration wurden mit DNS Ergebnissen verglichen. Räumliche Mittel und quadratische Mittel der Geschwindigkeit, Temperatur sowie Major- und Minorspezies zeigen eine vernünftige qualitative und quantitative Übereinstimmung mit den DNS-Daten. Außerdem wurden Streudiagramme und Statistiken der Wärmefreisetzung in Abhängigkeit von der Temperatur und alle Spezies verglichen. Mit dem ODT-Ansatz konnte die Mehrzahl von DNS-Ergebnissen nachgebildet werden, dennoch zeigen einige Statistiken eine gewisse Unterschätzung in der Zündungsrate.

Um die Stoßrohr-Simulationen ausführen zu können, wurde die inkompressible ODT-Implementierung um einem effizienten algorithmus für kompressibel Strömung erweitert und ein Modell zur Repräsentation schockgenerierter Turbulenz wurde entwickelt. Die benötigten Änderungen der Implementierung werden hervorgehoben und das entwickelte Modell wird beschrieben. Zur Validierung des kompressiblen Löser werden Ergebnisse für das von Sod beschriebene Riemann-Problem mit Ergebnissen eines Riemann-Löser verglichen. Für die Validierung des Modells zur Darstellung Schock-generierter Turbulenz werden Ergebnisse für nicht reaktive sowie reaktive Fälle gezeigt. Zuerst wird ein nicht reaktives Stoßrohr mit Reschock betrachtet, in dem ein Schock aus einer Mischung geringer Dichte (Luft) in eine Mischung hoher Dichte (Schwefelhexafluorid) läuft. Die ODT-Parameter sind entsprechend der Mischzonen ausbreitung aus Versuchsdaten und entsprechend turbulenter kinetischer Energie aus LES-Daten abgestimmt. Als zweites Beispiel wird ein reaktives Stoßrohr inklusive reflektive Schock simuliert. Eine Flamme wird in der Mitte des Rohrs initialisiert und beginnt sich auszubreiten während ein Schock auf sie zukommt. Ergebnisse für die Bildung der Mischzone und schließlichem Deflagrations-Detonations-Transition (DDT) wurden mit hoch aufgelösten 2D Simulationen (2D-Sim) verglichen. Vergleiche für Sods Stoßrohr zeigen, dass die Verdichtungsstoßgeschwindigkeit und das Schockprofil gut wiedergegeben werden. Vergleiche für das nicht reaktive Stoßrohr zeigen,

dass die Ausbreitung der Mischzonen für die betrachteten Mach-Zahlen korrekt erfasst werden und, dass die turbulente kinetische Energie der Größenordnung nach mit LES-Daten übereinstimmt. Vergleiche für die reaktiven Stoßrohrergebnisse zeigen, dass die Ausbreitung der Mischzonen über die Zeit korrekt erfasst wird und, dass die ungefähre Zeit und Position für DDT in ODT mit denen der 2D-sim übereinstimmt. Da DDT stark von der Feinheiten der einzelnen Simulationen abhängt, kann ODT nur durch einzelne Simulationen validiert werden, nicht durch ein Ensemble von Simulationen.





## PUBLICATIONS FROM THIS PHD RESEARCH

---

### **Journal publications:**

Z. Jozefik, A. R. Kerstein, H. Schmidt, Simulation of shock-turbulence interaction in non-reactive flow and in turbulent deflagration and detonation regimes using one-dimensional turbulence, *Combust. Flame*, 164:53-67, 2016.

Z. Jozefik, A. R. Kerstein, H. Schmidt, S. Lyra, H. Kolla, J. H. Chen, One-dimensional turbulence modeling of a turbulent counterflow flame with comparison to DNS, *Combust. Flame*, 162:2999-3015, 2015.

E. I. Monson, D. O. Lignell, M. A. Finney, C. Werner, Z. Jozefik, A. R. Kerstein, R. S. Hintze, Simulation of ethylene wall fires using the spatially-evolving one-dimensional turbulence model, in: *Fire Technology, Special Issue on Validation and Fire Modelling*, 2014. DOI 10.1007/s10694-014-0441-2

### **Conference proceedings:**

Z. Jozefik, A. R. Kerstein, H. Schmidt, Towards a compressible reactive multi-scale approach based on One-Dimensional Turbulence, in: *Papers Contributed to the Conference "Active Flow and Combustion Control 2014"*, Berlin, Germany, Springer series Notes on Numerical Fluid Mechanics and Multidisciplinary Design, September 10 - 12 2014. DOI 10.1007/978-3-319-11967-0\_13

### **Conference presentations:**

Z. Jozefik, A. R. Kerstein, H. Schmidt: Incorporation of acceleration effects into the one-dimensional-turbulence model, with application to turbulent combustion and shock-turbulence interactions, 15th International Conference on Numerical Combustion, April 19 - 22, 2015, Avignon, France.

Z. Jozefik, C. Jiménez, H. Schmidt: Detailed numerical simulation of forced planar premixed hydrocarbon flames, 12th Conference on Modeling Fluid Flow, September 04 - 07, 2012, Budapest, Hungary.

Z. Jozefik, C. Jiménez, H. Schmidt: Detailed numerical simulation of forced planar premixed flames, 34th International Symposium on Combustion, July 29 - August 3, 2012, Warsaw, Poland.



## ACKNOWLEDGMENTS

---

This dissertation could not have come to fruition without the help and support of many people.

I am very grateful to my advisor Prof. Heiko Schmidt for giving me the opportunity to begin this doctorate study and for giving me the freedom to pursue topics and directions that were of interest for me. I am indebted for his guidance and for the countless hours of discussions that we had often extending into the late evenings, particularly in the beginning as I went through a *re-booting* phase after having worked in industry for a number of years before returning to the university.

I would like to express my deep gratitude to Dr. Alan Kerstein who also advised me through out this dissertation. I am very thankful to Dr. Kerstein for always being available for discussion as well as for the general mentoring that he provided. After our meetings I felt motivated and inspired, and his guidance contributed significantly to the successful conclusion of this research.

I wish to thank Prof. David Lignell for several discussion on ODT and for providing his code for use.

Further, I am thankful to my colleges Falko Meiselbach, Eckhard Dietze, Christoph Glawe and Mark Simon Schöps for all discussions about turbulence, numerics, programming, and general Linux and Latex usage.

Finally, I would like to thank my Mother for her support in all things that I have embarked on through out the years.



# CONTENTS

---

Abstract	v
Zusammenfassung	vi
Publications	ix
Acknowledgments	xi
List of Figures	xvi
List of Tables	xvii
Acronyms	xviii
Nomenclature	xix
<b>I THEORY</b>	<b>1</b>
1 INTRODUCTION	3
1.1 Outline of thesis . . . . .	5
2 TURBULENT PREMIXED COMBUSTION	7
2.1 Turbulent flows . . . . .	7
2.2 Premixed flames . . . . .	9
2.3 Turbulent premixed combustion regimes . . . . .	11
2.4 Combustion chemistry . . . . .	13
3 MODELING BASICS	15
3.1 DNS, RANS, LES . . . . .	15
3.2 ODT . . . . .	17
3.2.1 ODT governing equations . . . . .	18
3.2.2 Eddy events . . . . .	18
<b>II INCOMPRESSIBLE ODT</b>	<b>25</b>
4 INTRODUCTION	27
5 ODT	29
5.1 Mathematical formulation . . . . .	29
5.2 Turbulence model . . . . .	30
5.3 Counterflow submodels . . . . .	31
5.3.1 Advection model . . . . .	31
5.3.2 Dilatation model . . . . .	32
5.3.3 Darrieus-Landau instability model . . . . .	33
6 COUNTERFLOW CONFIGURATION	35
6.1 ODT set-up . . . . .	35
6.2 DNS physical and numerical parameters . . . . .	37
7 RESULTS	39
7.1 Laminar flame results . . . . .	39
7.2 Turbulent flame results . . . . .	41
7.2.1 Spatial comparisons . . . . .	41
7.2.2 Scalar dissipation rate comparisons . . . . .	43
7.2.3 Flame attenuation . . . . .	43
7.2.4 Scatter plot comparisons . . . . .	45

7.2.5	Superadiabaticity test . . . . .	46
7.2.6	Differential diffusion effects . . . . .	49
7.2.7	State-space comparisons . . . . .	50
7.3	Parameter sensitivity study . . . . .	51
8	CONCLUSIONS	55
9	OUTLOOK	57
9.1	Cambridge stratified burner setup . . . . .	57
9.2	ODT modeling approach . . . . .	58
9.2.1	Inlet velocities and domain length . . . . .	59
9.2.2	Reactant and product inlet mixtures and temperatures	59
9.3	Results . . . . .	61
9.4	Conclusions . . . . .	64
<b>III</b>	<b>COMPRESSIBLE ODT</b>	<b>65</b>
10	INTRODUCTION	67
11	MODELING APPROACH	69
11.1	Overview . . . . .	69
11.2	Governing equations . . . . .	70
11.3	Chemical source terms . . . . .	71
11.4	Mesh adaption . . . . .	72
12	TURBULENCE MODEL	73
12.1	Reference-frame acceleration in ODT . . . . .	73
12.1.1	Darrieus-Landau-instability model . . . . .	74
12.1.2	Shock-turbulence-interaction model . . . . .	74
12.1.3	ODT adjustable parameters . . . . .	76
13	RESULTS	77
13.1	Sod's shock tube problem . . . . .	77
13.2	Non-reactive RM instability with reshock . . . . .	80
13.3	Reactive RM instability with reshock . . . . .	84
13.3.1	Reactive RM instability: Ma=1.50 case . . . . .	84
13.3.2	Reactive RM instability: Ma=1.63 case . . . . .	90
14	CONCLUSIONS	95
15	OUTLOOK	97
<b>IV</b>	<b>APPENDIX</b>	<b>99</b>
A	THERMODYNAMICS RELATIONS	101
A.1	1st Law of Thermodynamics . . . . .	101
A.2	Ideal gas relations . . . . .	101
A.3	Enthalpy . . . . .	103
A.4	Specific heat . . . . .	103
A.5	2nd Law of Thermodynamics . . . . .	104
B	RT, RM, AND DL INSTABILITIES	107
B.1	Rayleigh-Taylor and Richtmyer-Meshkov instability . . . . .	107
B.2	Darrieus-Landau instability . . . . .	110
C	NORMAL SHOCK THEORY	115
C.1	Shock equations . . . . .	115

c.2	Rankine-Hugoniot relations . . . . .	117
c.3	Limit of an infinitely strong shock . . . . .	118
c.4	Basics of detonation theory . . . . .	118
c.4.1	Zel'dovic-Neumann-Döring detonation theory . . . . .	119
c.4.2	Chapman-Jouget detonation theory . . . . .	121
D	REFERENCE-FRAME ACCELERATION IN ODT	123
E	DETAILS OF COMPRESSIBLE NUMERICAL IMPLEMENTATION	125
E.1	Balance equations . . . . .	125
E.2	Spatial discretization . . . . .	126
E.3	Temporal discretization . . . . .	127
F	SHOCK-TURBULENCE INTERACTION IN ODT	131
F.1	Time scales . . . . .	132
F.2	Eddy implementation for compressible flow . . . . .	133
	Bibliography	135

## LIST OF FIGURES

---

Figure 1.1	Caveman making fire. . . . .	3
Figure 2.1	Structure of a stationary premixed lean CH <sub>4</sub> /air flame. . . . .	10
Figure 2.2	Modified premixed combustion regime diagram. . . . .	13
Figure 3.1	ODT line of sight domain through a 3D turbulent flow . . . . .	17
Figure 4.1	Strained flame configurations . . . . .	28
Figure 5.1	Shape function for pressure source term . . . . .	32
Figure 5.2	Preliminary and final dilatation velocity profiles . . . . .	33
Figure 6.1	Schematic of the investigated counterflow burner . . . . .	36
Figure 7.1	1D laminar strained flame vs. bulk strain rate . . . . .	40
Figure 7.2	Laminar strained flame results. . . . .	41
Figure 7.3	Favre mean and RMS of the velocity, temperature, and species vs. axial distance. . . . .	44
Figure 7.4	Favre averaged scalar dissipation rate. . . . .	45
Figure 7.5	Left: hr vs. p.v. for the 1D strained laminar flame. Right: pdf of hr conditioned on the p.v. . . . .	45
Figure 7.6	Scatter plots of hr and major species vs. temperature . . . . .	47
Figure 7.7	Scatter plots of minor species vs. temperature . . . . .	48
Figure 7.8	Equilibrium calculation for input states from DNS and ODT results. . . . .	49
Figure 7.9	Scatter plot of element O and element H mixture fraction vs. Bilger’s mixture fraction. . . . .	50
Figure 7.10	ODT scatter plot of hr vs. temperature with Lewis number of all species equal to 1. . . . .	50
Figure 7.11	Temperature conditioned mean and RMS of the hr . . . . .	51
Figure 7.12	Temperature conditioned mean and RMS of mass fractions for all species . . . . .	52
Figure 7.13	Sensitivity of the ODT results to the eddy frequency parameter C, maximum allowed eddy size L <sub>max</sub> , and stagnation point location. . . . .	54
Figure 9.1	Cambridge burner setup. . . . .	58
Figure 9.2	ODT energy spectrum vs. wave number . . . . .	61
Figure 9.3	Scatter plot of mass fraction CH <sub>4</sub> , H <sub>2</sub> O, and O <sub>2</sub> vs. temperature for flame SwB9 . . . . .	62
Figure 9.4	Scatter plot of mass fraction CO, CO <sub>2</sub> , and H <sub>2</sub> vs. temperature for flame SwB9. . . . .	63
Figure 9.5	Mean mass fraction vs. temperature for ODT and experimental data for SwB1, SwB5 and SwB9. . . . .	64
Figure 12.1	Incident shock propagating to the right. . . . .	74
Figure 13.1	Sod’s shock tube problem at 0.4 ms . . . . .	78
Figure 13.2	Sod’s shock tube problem at 2.6 ms . . . . .	79
Figure 13.3	Geometry of the ODT 1D simulation domain. . . . .	81
Figure 13.4	Laminar wave diagram for Ma=1.50 (air/SF <sub>6</sub> ) . . . . .	81



Figure 13.5	TMZ width and TKE vs. time for the Ma=1.50 . . . . .	83
Figure 13.6	TMZ width vs. time for the Ma=1.24, 1.43, 1.50 and 1.98	83
Figure 13.7	Geometry of the ODT 1D simulation domain. . . . .	85
Figure 13.8	Laminar space-time density evolution for Ma=1.50 . . . . .	86
Figure 13.9	Laminar hr vs. time for Ma=1.50 . . . . .	86
Figure 13.10	Turbulent space-time density evolution for Ma=1.50 . . . . .	87
Figure 13.11	Turbulent hr vs. time for Ma=1.50 . . . . .	88
Figure 13.12	Pressure vs. time at x=12.8 cm, 19.2 cm and 25.6 cm . . . . .	89
Figure 13.13	Variation 1 for the Ma=1.50 case. . . . .	90
Figure 13.14	Variation 2 for the Ma=1.50 case. . . . .	91
Figure 13.15	Variation 3 for the Ma=1.50 case. . . . .	91
Figure 13.16	Turbulent space-time density evolution for Ma=1.63 . . . . .	92
Figure 13.17	Turbulent hr vs. time for Ma=1.63 . . . . .	93
Figure B.1	Initial configuration of the RT and RM instability . . . . .	107
Figure B.2	Baroclinic vorticity for L/H and H/L interface . . . . .	108
Figure B.3	Schlieren images of the RM instability: L/H interface . . . . .	108
Figure B.4	Schlieren images of the RM instability: H/L interface . . . . .	109
Figure B.5	Kelvin-Helmholtz instability . . . . .	109
Figure B.6	RT instability . . . . .	110
Figure B.7	Deflection of streamlines through a curved flame front. . . . .	111
Figure B.8	Schematic illustration of the DL instability mechanism. . . . .	112
Figure B.9	High speed film images of the DL instability . . . . .	112
Figure C.1	Flow model of a normal shock propagating to the left. . . . .	115
Figure C.2	Entropy-temperature plot for Fanno and Rayleigh lines . . . . .	117
Figure C.3	P-v diagram for Hugoniot curves . . . . .	120

## LIST OF TABLES

---

Table 6.1	Numerical and physical parameters . . . . .	36
Table 9.1	Operating conditions for Cambridge stratified burner. . . . .	57
Table 9.2	Cambridge burner physical parameters . . . . .	59
Table 9.3	ODT parameters . . . . .	60
Table 12.1	ODT adjustable parameters. . . . .	76
Table 13.1	Simulated Mach numbers and their corresponding test conditions. . . . .	81
Table 13.2	Post shock and post reshock TMZ growth rates for ODT and VS. . . . .	84

## ACRONYMS

---

AEA	activation-energy asymptotics
CFD	computational fluid dynamics
CFL	Courant-Friedrichs-Lewy
CJ	Chapman-Jouguet
DD	differential diffusion
DDT	deflagration to detonation transition
DL	Darrieus-Landau
DNS	direct numerical simulation
EE	eddy event
HCCI	homogeneous-charged compression-ignition
LEM	linear eddy model
LES	large eddy simulation
LESODT	large eddy simulation with ODT as a sub-grid-scale model
LHS	left hand side
LII	laser induced incandescence
ODT	one-dimensional turbulence
ODTLES	one-dimensional turbulence with a 3D coupling
PDF	probability density function
PLIF	planar laser induced fluorescence
RANS	Reynolds averaged Navier-Stokes
RHS	right hand side
RM	Richtmyer-Meshkov
RMS	root-mean-square
RT	Rayleigh-Taylor
STI	shock-turbulence interaction
TKE	turbulent kinetic energy
TMZ	turbulent mixing zone
VS	Vetter-Sturtevant
ZND	Ze'ldovich-von Neumann-Döring

NOMENCLATURE

---

Dimensionless parameters

At	Atwood number	$At = \frac{\rho_- - \rho_+}{\rho_- + \rho_+}$
Da	Damköhler number	$Da = \frac{\tau_t'}{\tau_c} = \frac{l'/u'}{\delta_f/S_u^L}$
Ka	Karlovitz number	$Ka = \frac{\tau_c}{\tau_\eta} = \frac{\delta_f/S_u^L}{\eta/u'}$
Ka <sub>r</sub>	Karlovitz number-reactive zone	$Ka_r = \frac{\tau_r}{\tau_\eta} = \frac{Ka}{100}$
Ma	mach number	$Ma = \frac{u}{\sqrt{\gamma P/\rho}}$
Re <sub>t</sub>	turbulent Reynolds number	$Re_t = \frac{u'l'}{\nu}$

Uppercase latin characters

C	-	ODT model constant: eddy rate constant
C <sub>j</sub>	-	pre-exponential constant for Arrhenius reaction rate
C <sub>s</sub>	-	STI model shock energy scaling factor
C <sub>rs</sub>	-	STI model reshock energy scaling factor
D	m	diameter
D	m <sup>2</sup> /s	diffusion coefficient
D <sub>th</sub>	m <sup>2</sup> /s	thermal diffusivity: $D_{th} = \frac{\lambda}{\rho c_p}$
E <sub>j</sub>	J/kmol	activation energy constant for Arrhenius reaction rate
E <sub>kin</sub>	J	ODT kinetic energy
E <sub>pe</sub>	J	ODT potential energy
E <sub>pe</sub> <sup>DL</sup>	J	ODT potential energy from DL model
E <sub>pe</sub> <sup>STI</sup>	J	ODT potential energy from STI model
E <sub>vp</sub>	J	ODT viscous penalty energy
J	m	ODT kernel transformation
K	m	ODT kernel transformation
L <sub>x</sub>	m	length of domain
L <sub>p</sub>	m	most probable size of an eddy
L <sub>min</sub>	m	minimum allowed size of an eddy
L <sub>max</sub>	m	maximum allowed size of an eddy
M	kg/kmol	molecular weight
Q	L/min	volumetric flow rate

$R$	J/kmol K	universal gas constant
$\bar{R}$	J/kg K	specific gas constant
$R$	-	autocorrelation function
$S_u^L$	m/s	laminar flame speed calculated for the unburnt mixture
$T$	K	temperature
$T_{ij}$	-	ODT energy redistribution tensor
TKE	$m^2/s^2$	turbulent kinetic energy
$V$	$m^3$	volume
$V_{cv}$	$m^3$	control volume
$X_s$	-	mole fraction of species $s$
$Y_s$	-	mass fraction of species $s$
$Z$	-	ODT model constant: eddy viscous penalty constant

### Lowercase latin characters

$a$	1/s	bulk strain rate
$a_{DL}$	$m/s^2$	acceleration term for Darrieus-Landau energy model
$a_{STI}$	$m/s^2$	acceleration term for shock-turbulence interaction energy model
$b_i$	1/s	constant for kernel addition J
$c_i$	1/s	constant for kernel addition K
$c_p$	J/kg K	specific heat at constant pressure
$c_v$	J/kg K	specific heat at constant volume
$e_{ij}$	1/s	strain rate tensor
$f$	-	ODT probability density function for $x_0$
$g$	-	ODT probability density function for $l$
$h$	J/kg	specific enthalpy
$hr$	$J/m^3 s$	heat release rate
$j_s$	$kg/m^2 s$	species diffusive flux
$k_j^b$	$kmol/m^3 s$	backward reaction rate of reaction $j$
$k_j^f$	$kmol/m^3 s$	forward reaction rate of reaction $j$
$l$	m	size of an eddy
$l'$	m	integral length scale
$p$	$N/m^2$	pressure
$p_e$	-	ODT probability of an eddy occurring
$q$	J/kg	heat of reaction/ heat flow
$q$	$W/m^2$	heat flux
$r$	-	random number
$s$	J/kg K	specific entropy

$t$	s	time
$u$	m/s	velocity
$u_i$	m/s	ODT velocity vector
$u_i^A$	m/s	advection velocity
$u_i^D$	m/s	dilatation velocity
$\hat{u}_i^D$	m/s	preliminary dilatation velocity
$u'$	m/s	velocity of integral length eddy
$v$	m <sup>3</sup> /kg	specific volume
$w$	J/kg	work done
$x$	m	location along ODT 1D line
$x_0$	m	starting location of an eddy on the ODT line

### Greek characters

$\alpha$	-	ODT parameter defining the energy redistribution
$\alpha$	-	fraction of added volume that is kept on the ODT line
$\beta$	-	ODT pressure source term
$\beta_j$	-	temperature exponent for Arrhenius reaction rate
$\gamma$	-	ratio of specific heats
$\delta$	m	turbulent mixing zone width
$\delta_r$	m	reactive layer thickness
$\delta_f$	m	laminar flame thickness
$\delta_{ij}$	-	Kronecker-Delta function
$\epsilon$	m <sup>2</sup> /s <sup>3</sup>	energy dissipation rate
$\eta$	m	Kolmogorov length scale
$\theta$	J/kg	specific internal energy
$\theta_{DL}$	-	delay time constant for Darrieus-Landau dominated eddies
$\theta_{STI}$	-	delay time constant for shock-turbulence interaction dominated eddies
$\lambda$	W/m K	thermal conductivity
$\lambda$	1/m <sup>2</sup> s	ODT rate distribution for eddy sampling
$\Lambda$	1/s	ODT total rate distribution of all eddies
$\mu$	kg/m s	dynamic viscosity
$\nu$	m <sup>2</sup> /s	kinematic viscosity
$\nu''_{js}$	-	backward molar stoichiometric coefficient of species s in reaction j
$\nu'_{js}$	-	forward molar stoichiometric coefficient of species s in reaction j
$\rho$	kg/m <sup>3</sup>	density
$\sigma_{ij}$	kg/m s <sup>2</sup>	deviatoric stress tensor
$\tau$	s	time scale of an eddy

$\tau'$	s	integral time scale
$\tau_c$	s	chemical time scale
$\tau_\eta$	s	time scale of Kolmogorov eddy
$\tau_r$	s	time scale of the reactive layer
$\tau_R$	s	residence time of flow
$\tau'_t$	s	turbulent integral time scale (turn over time of an eddy)
$\dot{\omega}$	kg/m <sup>3</sup> s	reaction rate
$\phi$	-	equivalence ratio

### Mathematical symbols

$\nabla$	nabla operator $\nabla = \frac{\partial}{\partial x_i}$
$\frac{D}{Dt}$	material derivative $\frac{D}{Dt} = \frac{\partial}{\partial t} + u_i \frac{\partial}{\partial x_i}$
S	source terms

### Diacritics

$\tilde{\Phi}$	Favre average of $\Phi$
$\bar{\Phi}$	mean of $\Phi$

### Subscripts and superscripts

$\Phi_-$	property take from the negative x-direction of the interface
$\Phi_+$	property take from the positive x-direction of the interface
$\Phi_b$	burnt gases
$\Phi_j$	$\Phi$ of reaction j
$\Phi_{max}$	maximum value of $\Phi$
$\Phi^0$	$\Phi$ at elevated temperature where fast chemistry begins
$\Phi_{rms}$	root mean square of $\Phi$
$\Phi_s$	$\Phi$ of species s
$\Phi_u$	unburnt gases

Part I

THEORY





INTRODUCTION

---

Combustion is the oldest technology of mankind and has been around for about 1 000 000 years. Today, approximately 90 % of the worlds energy supply is based on the burning of fossil and bio-fuels (wood, plant residues, dung, etc...) [102]. This shows that society continues to rely heavily on combustion processes for transportation, commerce, and power generation. Just in the

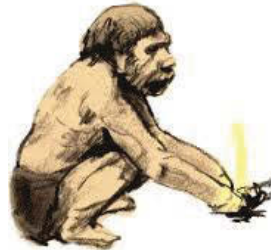


Figure 1.1: Caveman making fire.

segment of personal vehicles, sixty million cars (spark-ignition or diesel) were made in 2012, which is a 50 % increase to over a decade ago [95]. Associated with this massive oil use is the accompanying emission of pollutants, including nitric oxides ( $\text{NO}_x$ ) and particulates (soot), as well as the production of carbon dioxide ( $\text{CO}_2$ ). These pollutants have serious environmental and health implications and contribute to greenhouse gases which leads to climate change. Arrhenius described the role of  $\text{CO}_2$  as a greenhouse gas and its relation to global temperature rise as early as 1896 [4]. For these reasons, many governments have imposed and are continually tightening their emissions regulations [102]. As combustion is at the center of our energy need, even small efficiency gains can have a large impact on global emission levels. The formation of  $\text{CO}_2$  is unavoidable in burning of hydrocarbon based fuels and therefore the reduction of it is an efficiency question. The formation of  $\text{NO}_x$  and carbon monoxide ( $\text{CO}$ ) for example are avoidable and are signs of imperfect combustion.

So why do we still use a technology that's as old as Methuselah? Energy generated through the burning of fuels (spark-ignition, diesel, gas-turbines, furnaces) are compact, reliable and a portable form of energy. Consider that the kinetic energy of a 1 000 kg automobile traveling a 60 mph has about the same amount of energy as a teaspoon of gasoline or diesel fuel [95]. Or, that to match the energy in 1 kg of liquid fuel, 35 kg of the most advance battery is needed. According to a 2011 U.S. National Research Council report [1], internal combustion engines will be the dominant prime movers for light-duty vehicles for many years, probably decades. For medium- and heavy-duty commercial vehicles the estimates are even longer [95] and in the aerospace industry a half a century is estimated before small commercial airplanes can be powered by batteries for short distance flights. For these reasons, combustion research is very relevant today and will continue to remain so. Additionally, combustion research is not only important for achieving efficiency in man made applications, but also for safety reasons such as understanding fire prop-

agation in forest and buildings, preventing gas explosions in mines or hindering deflagration to detonation transition in closed environments.

The problems are being studied by experimentalists, theoreticians, and modelers. Advances in laser-based diagnostic equipment such as Planar Laser Induced Fluorescence or Incandescence (PLIF and LII) now permit characterization of combustion temperatures and species concentrations including combustion intermediates, radicals and particulates [95]. In combustion theory, Williams has identified the development of activation-energy asymptotics (AEA) as a cornerstone of conceptual and quantitative progress today and points to the need for reduced chemistry mechanisms going forward [119]. Modelers have benefited greatly from the continually increasing computer performances and efficient numerical tools that extend the realm of problems that can be tackled by computational fluid dynamics (CFD). However, the existence of a wide range of length and time scales in high Reynolds number (a measure of the degree of turbulence) flows representative of practical applications and the number of chemical species involved in combustion of hydrocarbon fuels makes direct numerical simulations (DNS), spatially and temporally resolved simulations of the governing equation, still computationally intractable [86]. Thus, a major goal of combustion research is to develop accurate, tractable, predictive models for combustion phenomena occurring in combustion devices [90].

Most current approaches to modeling turbulent combustion can be categorized as flamelet-like or probability distribution function (PDF) -like [90]. A key requirement for robust turbulent combustion modeling is that the model must be able to access a sufficient portion of the chemical-state manifold [90]. PDF models are advantageous in this regard, but are subject to significant limitations because they do not resolve flame structure and a mixing model is needed to account for mixing by molecular diffusion [10]. Flamelet models provide such resolution, but they rely on low-dimensional chemical manifolds. Thus, neither of these leading approaches to turbulent combustion modeling is fully satisfactory. Similar considerations apply to other commonly used approaches.

In this thesis an alternative approach is employed, mainly a model that reduces three dimensional (3D) turbulence to a one dimensional (1D) line of sight problem. One-dimensional turbulence (ODT), first proposed by Kerstein in [48], resolves flame structure in 1D without compromising chemical-state accessibility, and achieves major cost reduction relative to DNS through reduced spatial dimensionality. ODT is a fully resolved, unsteady stochastic simulation model that emulates turbulence. ODT has two key features. First, the properties of the flow reside on a one-dimensional domain. This 1D formulation allows full resolution of the interaction between large scales and molecular transport scales within computationally affordable simulations. Second, because vortical overturns cannot occur on a 1D domain, turbulent advection is represented using mapping events whose occurrences are governed by a random process. Unlike the Reynolds-averaged Navier-Stokes (RANS) model and large-eddy simulation (LES), which model the small scale phenomena and

retain the 3D representation of the flow, ODT resolves all the scales of motion but models 3D turbulence. Hence, ODT cannot capture geometrical effects and coherent flow structures, other than the so-called eddy events of ODT. In ODT, velocity components are transported and are used to determine the eddy frequency and eddy-size distribution, thereby providing a phenomenologically sound basis for driving turbulence.

The main objective of this thesis is to apply the ODT methodology (1) to a low-Mach number turbulent reactant-to-product counterflow flame and (2) to shock-turbulence interaction in non-reactive flows and in turbulent deflagration and detonation regimes. The strategy of incorporating acceleration induced instabilities into ODT is presented and specifically the instability arising from thermal expansion across a burning front and a shock traveling over an interface between two different gases is modeled. For the counterflow configuration, application specific submodels needed to address 3D dilatation and advection phenomena on the 1D line are developed. For the finite-Mach number applications, the currently used incompressible solver is extended to an efficient compressible solver. The necessary validation of submodels and intermediate steps are performed and results for application (1) and (2) are validated against DNS, LES, and experimental data.

## 1.1 OUTLINE OF THESIS

This doctoral dissertation is divided into four parts. In the present part, Sec. 1 provides a general introduction to this thesis. Sec. 2 introduces the basic concepts of turbulence and combustion and Sec. 3 discusses the main modeling approaches and motivates the use of ODT along with providing the detailed formulation of ODT. Part II and part III are designed to be self containing. They motivate, present model development and validation, and give a summary and outlook for the counterflow and the shock-tube application respectively. In the Appendix, part IV, mathematical details and background theory that are too cumbersome to be placed in the main body of the text are presented.



In turbulent premixed combustion a wide range of length and times scales exist. In this section the representative scales are presented and different turbulence regimes for premixed combustion based on the combination of flow and combustion scales are identified.

## 2.1 TURBULENT FLOWS

One of the key statistical tools used in turbulence theory is the spatial velocity autocorrelation function  $R$  defined as

$$R(\mathbf{x}, \mathbf{r}, t) = \frac{\overline{\mathbf{u}'(\mathbf{x}, t) \cdot \mathbf{u}'(\mathbf{x}+\mathbf{r}, t)}}{\overline{\mathbf{u}'(\mathbf{x})^2}}, \quad (2.1)$$

where  $\mathbf{x}$  is the position vector,  $t$  is the time,  $\mathbf{r}$  a vector indicating an offset in position, and  $\mathbf{u}'(\mathbf{x}, t) = \mathbf{u}(\mathbf{x}, t) - \overline{\mathbf{u}(\mathbf{x})}$  is the velocity fluctuation where  $\overline{\mathbf{u}(\mathbf{x})}$  is the mean velocity at location  $\mathbf{x}$ . The quantity  $R$  is equal to 1 when  $\mathbf{r} \rightarrow 0$  and decreases asymptotically to zero for large  $\mathbf{r}$ . If  $R$  does not depend on time, the turbulence is said to be stationary, if  $R$  does not depend on  $\mathbf{x}$ , the turbulence is homogeneous, and if  $R$  is identical in all direction, the turbulence is isotropic. Considering steady homogeneous isotropic turbulence, Eq. (2.1) becomes only a function of  $r$ , which could be a temporal or spatial variable, and is written as

$$R(r) = \frac{\overline{\mathbf{u}' \cdot \mathbf{u}'(r)}}{\overline{\mathbf{u}'^2}}. \quad (2.2)$$

Using the velocity autocorrelation function, the integral length scale  $l'$  is defined as

$$l' \equiv \int_0^\infty R(r) dr, \quad (2.3)$$

which can be interpreted as the distance for which two points have a considerably uncorrelated velocity. Using Taylor's hypothesis, also known as the frozen turbulence approximation, a relation for the integral time scale is written as

$$\tau' = \frac{l'}{\bar{u}}. \quad (2.4)$$

This method is applicable to statistically stationary flows in which the turbulence intensity  $u'$  is small compared with the mean velocity  $\bar{u}$  [89]. More

typically however, in turbulence studies the turnover time of an eddy (also termed turbulent integral time)  $\tau'_t$  is used and is defined as

$$\tau'_t \equiv \frac{l'}{u'}. \quad (2.5)$$

The turbulent Reynolds number  $Re_t$ , based on the integral length scale characteristics, is expressed as

$$Re_t \equiv \frac{u'l'}{\nu} \quad (2.6)$$

where  $\nu$  is the kinematic viscosity. Finally, the specific turbulent kinetic energy (TKE) is defined as

$$TKE = \frac{1}{2} \overline{u'_i \cdot u'_i}, \quad (2.7)$$

with subscript  $i \in \{1, 2, 3\}$  and Einstein summation over repeated indices  $i$  is implied.

In fully developed turbulence, most of the TKE is in the integral length scale. The energy transfers from the large scale structures by an essentially inviscid process to the smaller scales. This process continues producing a cascade of eddies until the smallest scales, known as the Kolmogorov scale  $\eta$ , dissipate the energy through viscosity and convert it to heat. At the smallest scales, viscous forces balance the inertial forces and the Reynolds number  $Re = u_\eta \eta / \nu$  is equal to unity. As formalized by Kolmogorov [55, 56], the energy transfer from the large eddies down to the smallest eddies occurs in the inertial sub-range of turbulence, and it happens locally such that the energy breaks down it steps. Turbulent eddies of size  $l$  and turnover velocity  $u$  are pictured to break down over the eddy turnover time  $\tau = l/u$ . Due to the locality of the transfer, the energy transfer rate (energy dissipation rate)  $\epsilon$  is independent of the length scales of the eddies and therefore is constant along the inertial sub-range. Based on dimensional reasoning,  $\epsilon$  can then be written as

$$\epsilon \sim \frac{u^2}{\tau} = \frac{u^3}{l}. \quad (2.8)$$

These concepts are stated formally in Kolmogorov's first and second similarity hypothesis:

- Kolmogorov's 1<sup>st</sup> similarity hypothesis: *In every turbulent flow at sufficiently high Reynolds number, the statistics of the small-scale motions have a universal form that is uniquely determined by  $\nu$  and  $\epsilon$ .*
- Kolmogorov's 2<sup>nd</sup> similarity hypothesis: *In every turbulent flow at sufficiently high Reynolds number, the statistics of the motions of scale  $l$  in the range  $l' \gg l \gg \eta$  have a universal form that is uniquely determined by  $\epsilon$ , independent of  $\nu$ .*

## 2.2 PREMIXED FLAMES

The applications in this thesis consider premixed flames. However, for completeness the difference between non-premixed and premixed flames are first mentioned. Then, to provide a foundation for later presented turbulent premixed flame results, the simplest premixed flame configuration, a planar laminar flame propagating in one direction, is presented.

In non-premixed flames (e.g. Diesel-engine, airplane turbine), fuel and oxidizer mix as they burn and the burning rate is controlled by the rate of reactant diffusion [67]. For this reason, non-premixed flames are also commonly referred to as diffusion flames. These flames are considered safer than premixed ones because fuel and oxidizer are kept separate up to the point of burning. However, because prior to burning the fuel and oxidizer might not have been mixed completely, non-premixed flames are also less efficient as they have lower burning rates and lead to higher pollution levels as they have higher local maximum temperatures [86]. For these reasons, in applications that use non-premixed flames, a great effort is made to mix fuel and oxidizer as fast as possible.

Premixed flames (e.g. Otto-engine, stationary gas turbine) are more intense and pollute less. They are also more dangerous because any high temperature point in the premixed gas can lead to ignition. Although in premixed combustion the fuel and oxidizer are mixed prior to burning on a molecular level, diffusion of temperature and species also has an important role. Temperature diffusion is important for preheating low temperature fuel and oxidizer to an elevated temperature for initiating fast chemical activity. Diffusion of intermediate species like O, H and OH are important for initiating decomposition of the fuel. However, as Arrhenius type chemical reaction rates are more sensitive to temperature changes than to species concentrations, a purely thermal flame theory usually suffices to account for finite-rate chemistry effects, except when autoignition, extinction or pollutant issues are involved [17].

In Fig. 2.1, the structure of a stationary laminar premixed lean methane/air flame is shown. Three main zones are identified: preheat zone, reactive layer and oxidation layer. Unburnt gases reach the flame from the left side with velocity equal to that of the laminar flame speed  $S_{\text{u}}^{\text{L}}$  (the speed at which the laminar flame front propagates normal to itself). In the preheat zone the temperature begins to rise from the unburnt temperature  $T_{\text{u}}$  to a temperature, denoted by  $T^0$ , large enough to enable chemical reaction and a balance between convection and diffusion is obtained. Chemical reaction occurs in the reactive layer, where a balance between reaction and diffusion is obtained. Finally, oxidation layer is the zone in which oxidation takes place (e.g. CO oxidizes to  $\text{CO}_2$ ).

Characterizing lengths for the flame are the flame thickness  $\delta_{\text{f}}$  and reaction layer thickness  $\delta_{\text{r}}$ . Several relationships have been proposed for estimating the flame thickness. Williams [118] estimates the flame thickness based on energy and mass balance considerations. The total heat released by the flame per unit area per second is  $q\dot{\omega}\delta_{\text{f}}$ , where  $q$  is the heat of reaction

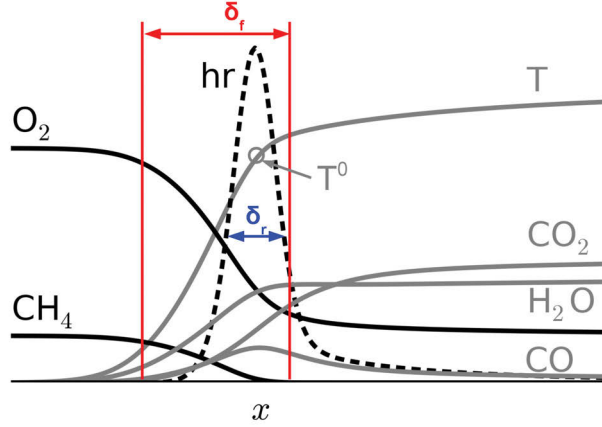


Figure 2.1: Structure of a computed stationary premixed lean  $\text{CH}_4/\text{air}$  flame. The thermal and reaction layer thicknesses are shown in red and blue respectively. Magnitudes have been scaled to exhibit qualitative trends.

and  $\dot{\omega}$  is the reaction rate. The heat conduction rate upstream is roughly  $\lambda^0 dT/dx \approx \lambda^0 (T_b - T_u)/\delta_f$ , where  $\lambda^0$  is the thermal conductivity of the gas evaluated at  $T = T^0$  and  $T_b$  is the temperature of the burnt products. Assuming adiabatic conditions (no heat loss) the energy conversion implies that  $q = c_p^0 (T_b - T_u)$ , where  $c_p^0$  is the specific heat at constant pressure of the mixture at  $T = T^0$ , and that the entire heat released must be conducted upstream. That is,  $q\dot{\omega}\delta_f = \lambda^0 (T_b - T_u)/\delta_f$ . Plugging in for  $q$  and solving for the flame thickness gives

$$\delta_f \approx \sqrt{\frac{\lambda^0}{c_p^0 \dot{\omega}}}. \quad (2.9)$$

The reaction rate term in Eq. (2.9) can be eliminated by solving for the laminar flame speed. The mass of combustible material per unit area per second flowing into the flame is  $\rho_u S_u^L$ , where  $\rho_u$  is the density of the unburnt mixture. The flame consumes these reactants at a rate  $\dot{\omega}\delta_f$ . Mass conservation then implies that  $\rho_u S_u^L = \dot{\omega}\delta_f$ . Eliminating  $\dot{\omega}$  in Eq. (2.9) gives

$$\delta_f \approx \frac{\lambda^0}{c_p^0 \rho_u S_u^L}. \quad (2.10)$$

For an order of magnitude estimate, [Sánchez et al. \[101\]](#) estimated the thermal diffusivity coefficient in Eq. (2.10) from the burnt products

$$\delta_f \approx \frac{D_{th,b}}{S_u^L} = \frac{\lambda^b}{c_p^b \rho_b S_u^L}, \quad (2.11)$$



where  $D_{th,b}$  is the thermal diffusion coefficient of the burnt products and Poinso et al. [87] used the kinematic viscosity  $\nu$  as

$$\delta_f \approx \frac{\nu}{S_u^L}. \quad (2.12)$$

Peters [85] proposed a definition based on the maximum temperature gradient as

$$\delta_f \approx \frac{T_b - T_u}{(\nabla T)_{max}}. \quad (2.13)$$

### 2.3 TURBULENT PREMIXED COMBUSTION REGIMES

To simplify the complexity of turbulent reacting flows, physical processes have been separated into categories that relate to fluid dynamics and those that relate to the flame. In this concept, the flame-turbulence interaction is reduced to the simple situation where a single turbulent eddy, mimicked by a spherical vortex, interacts with a laminar flame front [19]. Vortex-flame interaction constitutes a fundamental problem in combustion theory and is the basis of the laminar flamelet concept (see review by Renard et al. [96]).

The turbulence can be described by the velocity scale  $u'$ , the integral length scale  $l'$  and the Kolmogorov length scale  $\eta$ . The flame is described by its laminar flame speed  $S_u^L$ , laminar flame thickness  $\delta_f$  and the reactive layer thickness  $\delta_r$ . In typical flames, Peters [85] estimates  $\delta_r \approx 0.1\delta_f$ . Regimes of combustion are then described in terms of these six physical quantities. A choice can be made to draw a diagram with non-dimensional length ( $l'/\delta_f$ ) and velocity scale ( $u'/S_u^L$ ) ratio coordinates.

To characterize the relation between the chemical and fluid dynamical process, the Damköhler and the Karlovitz numbers are defined next. The turbulent Damköhler number  $Da$  is defined for the largest eddies and corresponds to the ratio of the turbulent integral time scale  $\tau_t'$  to the chemical time scale  $\tau_c$

$$Da \equiv \frac{\tau_t'}{\tau_c} = \frac{l'/u'}{\delta_f/S_u^L} = \frac{l' S_u^L}{\delta_f u'}. \quad (2.14)$$

The Karlovitz number  $Ka$  corresponds to the smallest eddies and is the ratio of the chemical time scale to the Kolmogorov time scale

$$Ka \equiv \frac{\tau_c}{\tau_\eta} = \frac{\delta_f/S_u^L}{\eta/u'} = \left(\frac{l'}{\delta_f}\right)^{-1/2} \left(\frac{u'}{S_u^L}\right)^{3/2} = \left(\frac{\delta_f}{\eta}\right)^2. \quad (2.15)$$

Equivalently, a second Karlovitz number can be defined based on the reactive zone thickness

$$Ka_r \equiv \frac{\tau_r}{\tau_\eta} = \left(\frac{\delta_r}{\eta}\right)^2 \approx \frac{Ka}{100}. \quad (2.16)$$

It can be shown, that the turbulent Reynolds, Karlovitz and Damköhler numbers are linked by the relation

$$\text{Re}_t = \text{Da}^2 \cdot \text{Ka}^2. \quad (2.17)$$

Two characteristic scales are defined to bound the flow structure ( $\eta$  and  $l'$ ) and two for the flame structure ( $\delta_f$  and  $\delta_r$ ). Depending on the order of magnitude of the Karlovitz number, different burning regimes are identified.

- Thin flame region ( $\text{Ka} < 1$ ): At low  $\text{Ka}$  numbers the flame timescale is faster than the timescale of the smallest eddy. Turbulence does not enter the flame structure and the flame is essentially wrinkled by the turbulence with curvature radius remaining larger than the flame thickness. This region can be further divided into two sub regions, depending on the velocity ratio  $u'/S_u^L$ :
  - Wrinkled flamelet regime ( $u' < S_u^L$ ): The speed of turbulent motions is too slow to wrinkle the flame front. Therefore interaction between two different flame fronts is not seen.
  - Corrugated flamelet regime ( $u' > S_u^L$ ): As the turbulent motion velocities increase, turbulence is able to wrinkle the flame such that interaction between two opposed flame fronts becomes possible. This leads to the formation of unburnt and burnt pockets of gas.
- Thin reaction zone ( $1 < \text{Ka} < 100$ ): Eddies can enter the preheat zone but not the reactive layer, the flame is hence thickened. The region can be further divided into two subregions based on the  $\text{Da}$  number.
  - $\text{Da} > 1$  ( $\tau_\eta < \tau_c < \tau_t'$ ): The chemical time scale is faster than the integral time scale but slower than Kolmogorov vortices. The notion of flame structure and laminar-burning velocity are less meaningful, but the inner reaction zones that are smaller than the flame thickness persist [96].
  - $\text{Da} < 1$  ( $\tau_r < \tau_c < 100\tau_\eta$ ): The chemical reaction is slower than turbulent mixing. All the eddies of the turbulence spectrum are able to disrupt the inner reaction regions. The reactants are well mixed and the reaction rate is controlled by chemistry.
- Broken reaction zones ( $100 < \text{Ka}$ ): The eddy time scale is a lot faster than the chemical time scale and the smallest eddies can penetrate the reactive layer. This leads to locally extinguished and distributed flame fronts. The turbulent flame fronts can not be represented by an ensemble of stretched laminar flames, hence the region is also referred to as the non-flamelet regime.

Fig. 2.2 shows the described premixed combustion diagram. In using the diagram, it is noted that classification of the described regions have been based

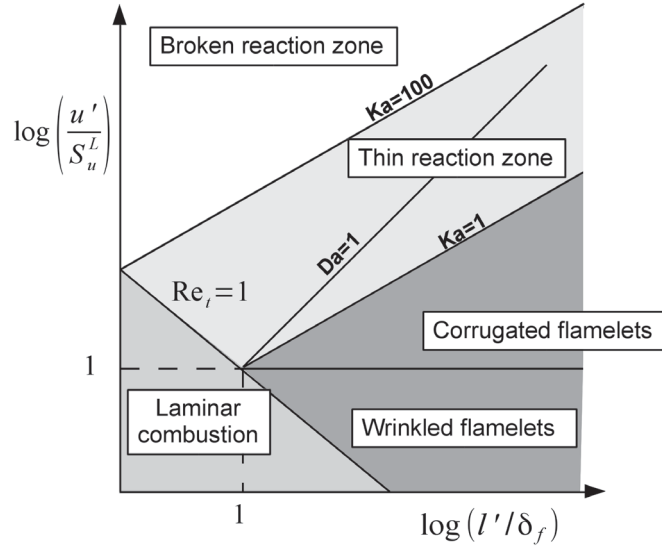


Figure 2.2: Modified premixed combustion regime diagram proposed by Peters [84]

on orders of magnitude considerations and therefore limits define only approximate values. For scaling purposes, the following additional assumptions have also been made:

- The turbulence is statistically steady, homogeneous and isotropic. Real turbulent flows may not follow this behavior,
- Unsteadiness is neglected. The flame response however depends on how long it is submitted to the vortex stretch and how fast the vortex is dissipated by viscous effects.
- Chemistry is modeled by a global single step reaction. In real flames, the chemical kinetics features a range of time scales.

## 2.4 COMBUSTION CHEMISTRY

Combustion is a high-temperature exothermic chemical reaction between a fuel and an oxidant and is described by a complicated sequence of elementary radical reactions of the form



where  $X_1 - X_4$  are the mole fractions, and  $v_1 - v_4$  are the molar stoichiometric coefficients. This can be written generically for the  $j^{\text{th}}$  elementary reactions and  $n_s$  number of species as



where  $X_s$  is the mole fraction of species  $s$ ,  $k_j^f$  and  $k_j^b$  are the forward and backward reaction rates of reaction  $j$  respectively, and  $v_{j_s}'$  and  $v_{j_s}''$  are the forward and backward molar stoichiometric coefficients of species  $s$  in reaction  $j$  respectively. The net chemical source term of species  $s$  depends on all reactions in which species  $s$  is involved in and is written as

$$\dot{\omega}_s = \sum_{j=1}^{n_r} (v_{j_s}'' - v_{j_s}') \cdot \omega_j \quad \text{for } s \in [1, n_s]. \quad (2.20)$$

The chemical reactions conserve total mass, which can be expressed as  $\sum_{s=1}^{n_s} \dot{\omega}_s = 0$ . In Eq. (2.20)  $\omega_j$  is the reaction rate of elementary reaction  $j$  which can be expressed as

$$\omega_j = k_j^f \prod_{s=1}^{n_s} X_s^{v_{j_s}'} - k_j^b \prod_{s=1}^{n_s} X_s^{v_{j_s}''} \quad \text{for } j \in [1, n_r]. \quad (2.21)$$

The reaction rate of a forward or backward reaction is expressed by Williams [119] as a modified Arrhenius expression

$$k_j = C_j T^{\beta_j} \exp\left(\frac{-E_j}{RT}\right) \quad \text{for } j \in [1, n_r], \quad (2.22)$$

where  $C_j$  is the pre-exponential constant,  $\beta_j$  the temperature exponent,  $E_j$  the activation energy,  $R$  the universal gas constant, and  $T$  the temperature.

The equations describing the evolution of a fluid have been known for some time now. Using the laws of mechanics put forth by Newton, Bernoulli analyzed the way fluids moved when subjected to various forces. Following this, Euler formulated a set of equations describing the motion of a hypothetical viscosity-free fluid. In 1822, Navier amended Euler's equations to cover the more realistic case of a fluid having viscosity. Although Navier's equations were correct, they were based a flawed reasoning and it was Stokes a few years later who provided the correct derivation and the equations became known as the Navier-Stokes equations [24]. The problem however is, that a solution to these equations does not (yet) exist. In fact, these equations are on a short list of the most important unsolved mathematical problems in human history [24]. Hence the need for numerical simulations.

With the advent of computers in the 1960's, numerical solutions of the governing equations became feasible and the practice of using computers to solve the equations of fluid mechanics has grown into its own branch of science called computational fluid dynamics (CFD). The basic idea is to approximate a continuous field with a discrete set of points distributed in space and advanced in time.

### 3.1 DNS, RANS, LES

Intuitively it makes sense that the more discrete points and smaller time steps that are used, the better the approximation will be. When resolving the full range of spatial and temporal scales in a turbulent flow, the simulation is called a direct numerical simulation (DNS). DNS is capable of providing a wealth of data, and although it will never replace experiments, it has greatly enhanced the understanding of the phenomenology of turbulence. For example, flow visualizations can be performed to examine turbulent structures, and multi-time, multi-point statistics can be extracted. However, computing costs grow with the flow turbulent Reynolds and Damköhler numbers. For DNS of non-reacting flows, to resolve every flow scale, based on dimensional reasoning, the scaling law reads  $Re_t^{3/4} \approx l'/\eta = N$ , where  $N$  is the number of cells in each direction. For reactive flows, the chemical scales set another condition on the simulation. It has been shown that for a one-step irreversible reaction, the flame structure needs approximately 20 grid points ( $Q \approx 20$ ) for adequate resolution [88]. This gives a spatial resolution requirement of  $\delta_f/Q$ . The size of the domain  $L_x$  in one spatial direction is then constrained by the number of cells  $N$  that the computer can handle and the resolution requirement as  $L_x = N \cdot \delta_f/Q$ . Noting that the domain size  $L_x$  is equal to the integral length scale  $l'$ , the equation can be rewritten as  $l'/\delta_f = N/Q$ . It

can then be shown that the spatial scaling for turbulent reactive flows is constrained by the product of the turbulent Reynolds number and the Damköhler number as  $Re_t Da \approx (N/Q)^2$ , where Eq. (2.12) was used to approximate the flame thickness in the Damköhler number given by Eq. (2.14). The application of DNS to a reactive problem is therefore limited by two ratios: the turbulent to flame thickness ratio,  $l'/\delta_f$ , and the turbulent to chemical speeds,  $u'/S_u^L$ . Current DNS simulations can cover only simple configurations which are used for model validations and understanding of fundamentals of turbulent reacting flows. Practical applications remain out of reach because of the high Reynolds number,  $O(10^8)$ , and the highly energetic fuels yielding  $l'/\delta_f$  to be of the order 10 to 1 000 and  $u'/S_u^L$  to range from 0.5 to 500 depending on the application [29].

As shown, the computational cost needed to capture the physics of the flow increases exponentially with  $Re_t$  and  $Da$ . The computational work becomes disproportionately weighted to the small scales such that approximately 99 % of the computational workload goes into resolving the small-scale energy, which however make up only 20 % of the total energy [89]. To be able to simulate practical applications, the strategy was developed to model the small scales and thereby reduce the spatial and temporal resolution requirements. One such strategy is based on separating the flow field into mean and overlaying fluctuation values,  $\phi = \bar{\phi} + \phi'$ . This is called the Reynolds decomposition and when applied to the fluid mechanics conservation laws the result is known as the Reynolds averaged Navier-Stokes (RANS) equations. Reynolds averaged, also known as time or ensemble averaged, mass-conservation equation is identical to the instantaneous equations. However, when the momentum equation is Reynolds averaged, the correlation term  $\overline{u'_i \cdot u'_j}$  appears. This is a time-averaged rate of momentum transfer due to the turbulence [117]. This term is known as the Reynolds-stress tensor and produces six new unknown quantities that need to be modeled to be able to close the equations. For a detailed description of major models for the Reynolds-stress tensor see Wilcox [117]. For reactive flows, the averaged equations for energy and species give similar correlation terms that require additional models. Solving these equations provide averaged quantities corresponding to averages over time for stationary mean flows. In other words, fluctuations are removed from the flow.

As computation power increased and greater resolution was afforded, there was an increased demand to not only solve for mean values but to also resolve some fluctuations in the flow. Large eddy simulations (LES) explicitly calculate time dependent large scales and model the effects of smaller ones using sub-grid closure rules. For non-reacting flows, sub-grid scale velocity models impose that the scale separation or filter cut-of frequency lies in the integral range of the turbulent spectrum enabling simulation of flows with approximately 500 times larger  $Re_t$  than DNS [29]. Evaluating the proper scaling for turbulent reacting LES remains unclear and depends on the turbulent combustion model used to close the sub-grid models [29].

Ideally, LES is best suited for applications where the chemical time scales and the fluid motion time scales do not overlap, such as in flames that do not

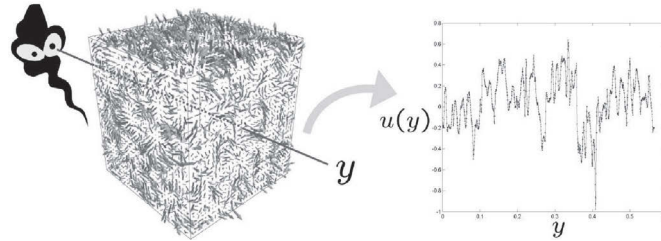


Figure 3.1: Left: The box represents a 3D turbulent flow and the  $y$ -axis represents the ODT line of sight domain. Right: The instantaneous velocity field along the  $y$ -axis. The figure is adopted from [75].

have significant extinction and reignition. In such cases, it is reasonable to separate the chemistry from the flow and solve it separately. The decoupled chemistry is then implemented in the simulation in the form of a look-up table constructed prior to the simulation using simple flame configurations such as a perfectly stirred reactor, laminar premixed flames, or laminar opposed flow flames. The turbulence-chemistry interactions are accounted for by a mixing model, which is generally a presumed PDF of the transported parameters. For a more detailed description of LES of turbulent reactive flows see Liu et al. [69].

### 3.2 ODT

Opposed to LES and RANS, the one-dimensional turbulence (ODT) model takes the approach of resolving the small scales and modeling the large scales. This approach was first introduced in 1999 by Kerstein [48]. Capturing the dynamics of the small scales is critical for proper treatment of species transport and reaction in order to capture such phenomena as extinction and reignition. Hence, the ODT domain is a discrete set of points along a 1D line that notionally represents a line of sight through a fully resolved 3D flow field (see Fig. 3.1). ODT is an outgrowth of the Linear Eddy Model (LEM) [45, 46, 47, 76], but unlike LEM, where frequency and eddy-size distribution of the events are based on a predefined kinetic energy spectrum (hence no feedback from the local flow to the random process governing the determination of eddy events), ODT includes the solution of the local velocity field to determine the rate and size of eddy occurrence.

In stand-alone applications, ODT is applicable in situations where a direction of predominant large-scale gradient is present, such as in shear-driven flows, buoyancy-driven flows, etc. As a stand-alone model, ODT has been used to simulate homogeneous turbulent non-reacting [5, 48, 50, 103, 104, 121] and reacting flows [27, 37, 38, 65, 93]. Notably, for non-premixed combustion ODT has provided fundamental insights concerning the spatio-temporal features of extinction-reignition [38] and yields overall agreement, in considerable detail, with state-space statistics obtained from DNS of temporally developing jet diffusion flames [65, 91]. For stand-alone modeling of turbulent flows using ODT, one must define the dominant direction of mean property varia-

tion. For complex flows which may not have a single dominant direction, ODT has been used as a sub-grid scale model in both RANS [92, 93] and LES [13] to provide closure for reacting scalars in combustion. An alternative multi-dimensional approach called ODTLES is discussed in [31, 32, 33, 34, 104].

The ODT model consists of two primary ingredients:

- The governing equations written in terms of two independent variables,  $(x, t)$  for ‘temporal’ ODT formulations and  $(x, y)$  for ‘spatial’ ODT formulation.
- Discrete ‘eddy events’ that occur at various points in  $(x, t)$  or  $(x, y)$ .

In ODT, the turbulent motions are modeled through a series of stochastic rearrangement events. These events may be interpreted as the model analog of individual turbulent eddies which are referred to as ‘eddy events’ or simply ‘eddies’. Each eddy event interrupts the time advancement of other processes and an instantaneous transformation is applied to the property profiles over some spatial interval  $[x_0, x_0 + l]$ , where  $x_0$  represents the eddy starting location and  $l$  is the eddy length.

According to Wilcox [117], an ideal model should introduce the minimum amount of complexity while capturing the essence of the relevant physics. In the development of ODT this has been the guiding principle.

### 3.2.1 ODT governing equations

The evolution of the 1D field is governed by the Navier-Stokes equations with the nonlinear advective term being replaced by a stochastic mapping model. Without the advection term, the Navier-Stokes equations become a diffusion equations with source terms where applicable and can be written in an ODT representation as

$$\frac{\partial \rho u_i}{\partial t} + EE(u_i) = \frac{\partial}{\partial x} \left( \mu \frac{\partial u_i}{\partial x} \right) + S_{u_i}, \quad (3.1)$$

$$\frac{\partial \rho \phi}{\partial t} + EE(\phi) = \frac{\partial}{\partial x} \left( D_\phi \frac{\partial \phi}{\partial x} \right) + S_\phi. \quad (3.2)$$

$EE$  represents the stochastic eddy process,  $\rho$  the density,  $\phi$  an arbitrary scalar,  $D_\phi$  the scalar diffusion coefficient,  $u_i$  with  $i \in \{1, 2, 3\}$  are the three ODT velocity components,  $x$  is the ODT line direction, and  $S_{u_i}$  and  $S_\phi$  represent source terms in the momentum and scalar equations respectively.

### 3.2.2 Eddy events

The eddy event is central to the ODT modeling approach. It models the effects of a three-dimensional eddy using a 1D rearrangement. Eddy events are intended to be qualitatively similar to turbulence in that they have the effect of



increasing gradients, redistributing fluid elements to increase mixing and are guided by the principle of scale locality. That is, turbulence breaks down in steps and that fluid elements can mix only with other fluid elements that are near each other. A complete definition of the model for an eddy event requires specification of:

- the procedure for selecting the candidate eddy starting location  $x_0$  and length  $l$ ,
- triplet mapping the spatial interval  $[x_0, x_0 + l]$ ,
- the kernel transformation procedure,
- the eddy rate distribution.

In ODT, each eddy is an instantaneous event and does not interact directly with other eddies. Rather, the interaction is indirect, in that over an eddy the flow properties change and influence the likelihood of acceptance of future eddies.

In ODT it is not implied that a specific eddy event represents any one specific eddy in the 3D flow, but rather that by choosing an ensemble of eddy events the statistical properties of 3D turbulence can be built up. An analogy can be made to Fourier analysis in that any arbitrary function can be reproduced by taking a collection of sine waves of particular periods, phase shifts and amplitudes. In ODT the period can be thought of as the eddy length, the phase shift as the eddy starting location, and the amplitude as the frequency of occurrence of a particular eddy.

### 3.2.2.1 Eddy starting location and length

At the start of an eddy event, an eddy length  $l$  and location  $x_0$  are selected from randomly generated numbers and set constants. The eddy length is defined as

$$l = \frac{-2L_p}{\ln\left(\frac{2L_p r}{c_e}\right) + \ln\left(\frac{2L_p}{L_{\min}}\right)}, \quad (3.3)$$

where  $r$  is a random number between 0 and 1,  $L_p$  and  $L_{\min}$  are set constants defining the most probable and smallest allowed eddy size respectively, and  $c_e$  is given by

$$c_e = \frac{2L_p}{\exp\left(\frac{-2L_p}{L_{\max}}\right) - \exp\left(\frac{-2L_p}{L_{\min}}\right)}, \quad (3.4)$$

where  $L_{\max}$  is a set constant defining the largest eddy size allowed. The eddy length could as well be selected from a uniform distribution, however Eq. (3.3)

provides an efficient means of selecting eddies that are most likely to be accepted. The eddy starting location is then given by

$$x_0 = r \cdot (L_x - l) \quad (3.5)$$

where  $L_x$  is the 1D domain length.

### 3.2.2.2 Triplet map

The functional form chosen for the triplet map is the simplest of a class of mappings that satisfy the physical requirements of

- measure preservation: all integral properties (e.g., mass, momentum, and energy) are the same before and after the triplet map
- continuity: no introduction of discontinuities by the mapping
- scale locality: at most order-unity changes in property gradients and immediate neighbor cells are placed no more than 3 cells apart from each other over the eddy interval.

The triplet map is conveniently represented by its inverse  $f(x)$ , such that the map moves fluid at location  $f(x)$  to location  $x$ , where  $f(x)$  is of the form [48]

$$f(x; x_0, l) \equiv x_0 + \left\{ \begin{array}{ll} 3(x - x_0) & \text{if } x_0 \leq x \leq x_0 + \frac{1}{3}l \\ 2l - 3(x - x_0) & \text{if } x_0 + \frac{1}{3}l \leq x \leq x_0 + \frac{2}{3}l \\ 3(x - x_0) - 2l & \text{if } x_0 + \frac{2}{3}l \leq x \leq x_0 + l \\ x - x_0 & \text{otherwise} \end{array} \right\}. \quad (3.6)$$

This mapping takes a line segment  $[x_0, x_0 + l]$  shrinks it to a third of its original length, and then places three copies on the original domain. The middle copy is reversed, which ensures that property fields remain continuous and introduces the rotational folding effect of turbulent eddy motion. All quantities outside the  $[x_0, x_0 + l]$  interval are unaffected.

### 3.2.2.3 Kernel transformation

The kernel transformation  $c_i K(x)$  is applied to redistribute energy from each velocity component among the three velocity components. This procedure is also called pressure scrambling and enables the model to simulate the tendency of turbulent eddies to drive the flow toward isotropy. For constant density formulations,  $\int K(x) dx = 0$  assures that the kernel  $c_i K(x)$  changes the energy of velocity component  $i$  while also conserving moment. However, for the variable density formulation, density is a function of  $x$  and momentum conservation is not anymore given if  $c_i K(x)$  is added. Therefore, a second kernel  $b_i J(x)$  needs to be applied to ensure momentum conservation [5, 50]. In this context, the effect of an eddy can be represented as

$$u_i(x) \quad \longrightarrow \quad u_i(f(x; x_0, l)) + c_i K(x) + b_i J(x), \quad (3.7)$$

for the velocity components and for an arbitrary scalar as

$$\phi(x) \quad \longrightarrow \quad \phi(f(x; x_0, l)), \quad (3.8)$$

where

$$K(x) = x - f(x; x_0, l), \quad J(x) = |K(x)|. \quad (3.9)$$

The triplet map of the velocity components is augmented by a kernel transformation to enforce momentum and energy conservation for the variable density flow and to redistribute kinetic energy among the velocity components due to the reorientation of the velocity vector during the eddy motion due to the pressure gradients acting on it. Both  $c_i K(x)$  and  $b_i J(x)$  are nonzero within the eddy interval, but while the kernel  $c_i K(x)$  integrates to zero over the eddy interval,  $b_i J(x)$  does not. This is due to the energy that is either removed from or added to each velocity component. The amplitudes of the kernel function ( $c_i$  and  $b_i$ ) are determined individually for each eddy based on the kernel function used in the vector formulation of ODT in [5, 50].

To determine the values  $c_i$  and  $b_i$ , first the kinetic energy change for a given component due to the mapping and the subsequent kernel transformation is written. Linear momentum conservation implies

$$\begin{aligned} & \int_{x_0}^{x_0+l} \rho(f(x)) [u_i(f(x)) + b_i J(x) + c_i K(x)] dx \\ &= \int_{x_0}^{x_0+l} \rho(f(x)) [u_i(f(x))] dx. \end{aligned} \quad (3.10)$$

The left hand side (LHS) of Eq. (3.10) represents the integrated momentum after the application of the triplet map and kernel transformation and the right hand side (RHS) of the equation represents the integrated momentum after the application of the triplet map alone. The mapped profile is used on the RHS instead of the original initial profile so that the representation in Eq. (3.10) looks at the contribution of the pressure scrambling alone instead of the combined effects of the triplet map and pressure scrambling operation [57]. Since the triplet map is measure preserving, it does not change the integrated momentum. Due to the measure preserving property of the triplet map, Eq. (3.10) reduces to

$$b_i \int \rho(f(x)) J(x) dx = -c_i \int \rho(f(x)) K(x) dx. \quad (3.11)$$

The integral limits have been dropped because by definition, the integral of the kernel vanish outside the eddy interval. The following relationship is then obtained

$$b_i = -c_i \frac{\rho_K}{\rho_J} \quad (3.12)$$

where

$$\rho_K \equiv \frac{1}{l^2} \int \rho(f(x))K(x)dx, \quad (3.13)$$

and

$$\rho_J \equiv \frac{1}{l^2} \int \rho(f(x))J(x)dx. \quad (3.14)$$

The change in kinetic energy for a given component is then given by

$$\begin{aligned} \Delta E_i &= b_i \int \rho(f(x))u_i(f(x))J(x)dx \\ &+ c_i \int \rho(f(x))u_i(f(x))K(x)dx \\ &+ \frac{1}{2}b_i^2 \int \rho(f(x))J^2(x)dx \\ &+ b_i c_i \int \rho(f(x))J(x)K(x)dx \\ &+ \frac{1}{2}c_i^2 \int \rho(f(x))K^2(x)dx. \end{aligned} \quad (3.15)$$

Using Eq. (3.12) and noting that  $J^2(x) = K^2(x)$ , after some manipulation

$$\Delta E_i = P_i c_i + S c_i^2, \quad (3.16)$$

where

$$P_i \equiv l^2(u_{i,\rho K} - A u_{i,\rho J}) \quad (3.17)$$

$$S \equiv l^3\left(\frac{1}{2}(A^2 + 1)\rho_{KK} - A\rho_{JK}\right) \quad (3.18)$$

$$u_{i,\rho K} \equiv \frac{1}{l^2} \int \rho(f(x))u_i(f(x))K(x)dx \quad (3.19)$$

$$u_{i,\rho J} \equiv \frac{1}{l^2} \int \rho(f(x))u_i(f(x))J(x)dx \quad (3.20)$$

$$\rho_{KK} \equiv \frac{1}{l^3} \int \rho(f(x))K^2(x)dx \quad (3.21)$$

$$\rho_{JK} \equiv \frac{1}{l^3} \int \rho(f(x))J(x)K(x)dx \quad (3.22)$$

$$A = -\frac{b_i}{c_i}. \quad (3.23)$$

Plotting Eq. (3.16),  $\Delta E_i$  vs  $c_i$ , gives a parabola with positive curvature. The maximum available energy to extract is given by differentiating the equation with respect to  $c_i$

$$Q_i \equiv -\Delta E_i |_{\max} = \frac{P_i^2}{4S}. \quad (3.24)$$

Given the constraints  $\sum_i \Delta E_i = Q_i$  and  $\Delta E_i \geq -Q_i$ , and requiring that the formulation be invariant under an exchange of indices (90 degree rotations of the reference frame) then the energy change for  $i$  is given by a symmetric transformation of  $Q_i$  [75]. That is  $\Delta E_i = \alpha T_{ij} Q_j$  and  $T_{ij}$  is symmetric and defined as

$$T_{ij} \equiv \begin{bmatrix} -1 & \frac{1}{2} & \frac{1}{2} \\ \frac{1}{2} & -1 & \frac{1}{2} \\ \frac{1}{2} & \frac{1}{2} & -1 \end{bmatrix}. \quad (3.25)$$

The free parameter  $\alpha$  then has the physically realizable range  $\alpha \in [0, 1]$ , with  $\alpha = 2/3$  being the preferred model [49] and resulting in equipartition of energy in the pressure scrambling model. Now plugging in and solving Eq. (3.16) for  $c_i$  gives

$$c_i = \frac{1}{2S} \left[ -P_i + \text{sgn}(P_i) \sqrt{P_i^2 + \alpha T_{ij} P_j^2} \right]. \quad (3.26)$$

#### 3.2.2.4 Eddy selection/eddy rate distribution

The eddy selection process is stochastic and follows the variable density formulation of Ashurst and Kerstein [5, 6]. Based on dimensional relationships applied to turbulence, for events defined in ODT, a relationship between an eddy's size  $l$ , turn over time  $\tau$  and kinetic energy can be formulated as

$$\frac{1}{\tau} = C \sqrt{\frac{2K_0}{\rho_0 l^3} (E_{kin} - ZE_{vp} - E_{pe})}. \quad (3.27)$$

where  $E_{kin}$  is a measure of kinetic energy as in [5],  $\rho_0 = \int \rho K^2(x) dx$ , and  $K_0 = \int K^2(x) dx$  where  $K(x)$  is the kernel function as in [5].  $E_{vp}$  is a viscous penalty defined using scaling arguments as  $E_{vp} = \frac{1}{2} \bar{\mu}^2 / \bar{\rho} l$ , where  $\bar{\rho}$  and  $\bar{\mu}$

are the average density and harmonically averaged [27] viscosity in the eddy region and  $E_{pe}$  is a potential energy change. The adjustable model parameter  $C$  represents turbulence intensity and  $Z$  represents a viscous penalty factor, a lower limit on the minimum energy required for an eddy to be accepted. In principle this is not necessary and could be set to zero, since eddies with small energies are typically small eddies that have negligible effect on the physical evolution of the system.  $Z$  is therefore used for efficiency purposes, to neglect implementing eddies that have no influence on the system. The evaluation of  $\tau$  depends on the instantaneous flow state, so eddy occurrences are responsive to unsteadiness resulting from transient forcing or statistical fluctuations inherent in the eddy-sampling process. The eddy occurrences thus depend on the effects of prior eddies and affect future eddy occurrences. These dependencies induce spatio-temporal correlations among eddy events, leading to a physically based representation of turbulence intermittency.

From  $\tau$ , the local rate of an eddy  $\lambda$  is calculated as

$$\lambda(x_0, l) = \frac{1}{l^2 \tau}. \quad (3.28)$$

Then, the probability of the eddy occurring  $p_e$  is computed as

$$p_e = \frac{\lambda \Delta t}{f(x_0)g(l)}, \quad (3.29)$$

where  $f(x_0)$  and  $g(l)$  are the PDFs for  $x_0$  and  $l$ , respectively given by

$$f(x_0) = \frac{c_e}{l^2} \exp\left(\frac{-2L_p}{l}\right), \quad g(l) = \frac{1}{L_{\max} - L_{\min}}. \quad (3.30)$$

The functional forms of  $f(x_0)$  and  $g(l)$  can influence the computational cost of the simulation but does not affect the results [48]. The calculated probability of the eddy  $p_e$  is compared to a random number generated on the interval  $[0, 1]$ . If the random number is less than  $p_e$ , then the eddy will be implemented.

The total rate of all eddies  $\Lambda$  is calculated as

$$\Lambda = \int \int \lambda(x_0, l) dx_0 dl. \quad (3.31)$$

Hence, the joint PDF of eddy parameters  $x_0$  and  $l$  is  $P(x_0, l) = \lambda(x_0, l)/\Lambda$ . Eddy occurrences are sampled from a Poisson distribution with mean rate  $\Lambda$ , with  $x_0$  and  $l$  parameters sampled from  $P(x_0, l)$ . To restrict the occurrence of unphysically large eddies, the maximum eddy size allowed is an input parameter that is problem specific.

## Part II

# INCOMPRESSIBLE ODT





*The contents of the Incompressible ODT part have been extracted from Jozefik et al. [42]. Adaptations have been performed to enhance discussions where appropriate or to avoid repetition of theory or background information.*

The study of laminar counterflow flames were originally motivated by attempts to model turbulent flames as a collection of strained laminar flamelets embedded within the flow [20]. One basic idea of the flamelet model is that strain rate imposed by the turbulent flow on the laminar flamelet stretches the flame changing the flame inner structure, the consumption of reactants and the heat release rate per unit area. The counterflow configuration is one of the simplest configurations allowing the effects of strain to be studied in a controlled manner while at the same time being suitable for studying burning regimes that covers the entire mixing spectrum from premixed, partially premixed, to non-premixed flames. A range of possible configurations is shown in Fig. 4.1. Laminar counterflow flames have been extensively studied (see reviews of Law and Sung [60] and Williams [120]) and is particularly useful for fundamental research because the governing equations can be simplified and cast as a function of the axial spatial coordinate only, enabling 1D solutions of the flame structure. Theoretical work has been performed using elementary chemistry [30, 99] as well as model [105] and reduced [100] chemistry.

Libby [62] pointed out that the experimental, computational and theoretical advantages attributed to the laminar counterflow flames apply as well to their turbulent counterparts. Although the turbulent counterflow configuration may seem removed from practical combustion problems, it has direct relevance to the study of turbulent shear flows and the effects of bulk strain rate can be studied. The reactant-to-product turbulent counterflow problem is particularly relevant to practical systems as it allows one to study effects of heat loss, burnt product stratification and flame dilution in a controlled environment. By operating in a turbulent Reynolds number regime of relevance to practical systems such as gas turbines and internal combustion engines, counterflow flames retain the interaction of turbulence and chemistry of these environments [18], but additionally offer several advantages including: (a) the achievement of high Reynolds numbers without pilot flames, which is particularly advantageous from a modeling standpoint; (b) compactness of the domain by comparison with jet flames, with advantages from both a diagnostic and computational viewpoint; and (c) reduction or elimination of soot formation due to high strain rates and low residence times. For these reasons, the system is ideally suited to be used for computational model validation.

In this thesis, numerical studies of a turbulent counterflow flame are conducted as a benchmark for validating stand-alone ODT. Moreover, a premixed

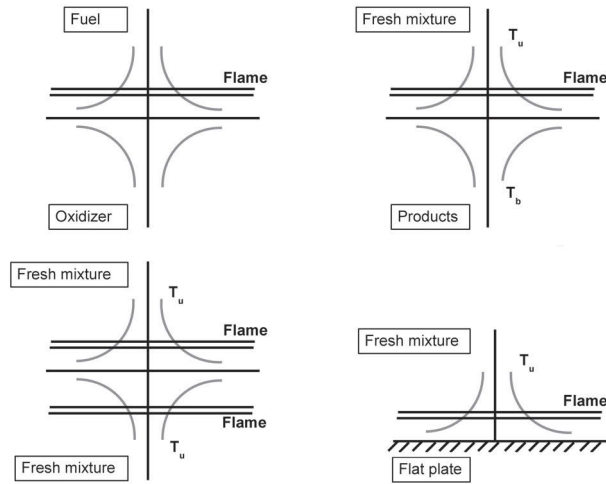


Figure 4.1: Strained flame configurations. Top left: strained diffusion flame. Top right: strained premixed flame formed by a counterflow of fresh mixture and hot products. Bottom left: strained premixed flame formed by a counterflow of fresh mixtures. Bottom right: strained premixed flame formed near a flat plate.

counterflow configuration is considered, providing the first detailed validation of ODT turbulence-chemistry interactions in turbulent premixed flames.

This part is organized as follows. Sec. 5.1 summarizes the mathematical formulations. Sec. 5.2 gives a short overview of ODT. For further depth on ODT, the reader is referred to Sec. 3.2. Sec. 5.3 introduces the ODT counterflow specific models. Sec. 6 describes the current counterflow configuration and boundary conditions. In the results, Sec. 7, model predictions for mean and RMS velocity and species profiles are compared to DNS data. Further, mixing rates are compared by looking at scalar dissipation rates and flame extinction/ignition characteristics by looking at the probability distribution of heat release rate conditioned on a chosen progress variable. To compare the range of results provided by DNS and ODT, scatter plots over temperature are shown. Statistics conditioned on temperature are compared for a more stringent test of model performance and a sensitivity study is carried out for the ODT input parameters. Finally, in Sec. 9 an outlook for possible future work is provided.

## 5.1 MATHEMATICAL FORMULATION

The set of variable density zero-Mach-number equations are solved in one spatial dimension in a Lagrangian framework on an adaptive grid. In all equations,  $x$  is the ODT line direction.

Following the formulation in [66], the continuity equation in integral form for a control volume  $V$  that encloses the mixture mass is first written. In Lagrangian formulation, the system boundary moves with the mass-average velocity so that in the direction of the ODT domain no mass crosses the control volume boundary via convective transport, only through diffusive transport. Since there is no mass source term, the Reynolds transport theorem is written for the continuity equation as

$$\frac{d}{dt} \int_V \rho dV = 0, \quad (5.1)$$

where  $\rho$  is the density. For uniform properties inside the control volume, and in 1D, the equation is integrated to give

$$\frac{d}{dt}(\rho dx) = 0, \quad \longrightarrow \quad \rho dx = \text{constant}, \quad (5.2)$$

where  $dx$  is a Lagrangian interval. This shows, that during a time advancement of the partial differential equations, the total mass in a given grid cell is constant. The balance equations for momentum, species mass fractions, and enthalpy are

$$\frac{d}{dt}(u_i) = \frac{1}{\rho} \frac{\partial}{\partial x} \left( \mu \frac{\partial u_i}{\partial x} \right) + \beta \delta_{i1} \quad (5.3)$$

$$\frac{d}{dt}(Y_s) = \frac{\dot{\omega}_s}{\rho} - \frac{1}{\rho} \frac{\partial j_s}{\partial x}, \quad (5.4)$$

$$\frac{d}{dt}(h) = -\frac{1}{\rho} \frac{\partial q}{\partial x}, \quad (5.5)$$

with  $s = 1, \dots, n_s$  and  $n_s$  is the number of different species in the gas mixture. Here,  $\mu$  is the dynamic viscosity of the mixture,  $u_i$  with  $i \in \{1, 2, 3\}$  are the three ODT velocity components,  $\beta$  is a pressure source term model discussed in Sec. 5.3.1,  $Y_s$  is the mass fraction of species  $s$ ,  $\dot{\omega}_s$  is the chemical source

term of species  $s$ ,  $h$  is the enthalpy of the mixture, and  $p$  the pressure. The species diffusive flux  $j_s$  is given by

$$j_s = -\rho D_s \left( \frac{\partial Y_s}{\partial x} + \frac{Y_s}{\bar{M}} \frac{\partial \bar{M}}{\partial x} \right), \quad (5.6)$$

where  $D_s$  is the diffusion coefficient of species  $s$  and  $\bar{M}$  is the mean molecular weight. The heat flux  $q$  is given by

$$q = -\lambda \frac{\partial T}{\partial x} + \sum_{s=1}^{n_s} h_s j_s, \quad (5.7)$$

where  $h_s$  is the enthalpy of species  $s$  including the heats of formation,  $\lambda$  is the thermal conductivity and  $T$  is the temperature. The equation of state of a mixture of ideal gases is given by

$$p = \rho T \frac{R}{\bar{M}}, \quad (5.8)$$

with  $R$  denoting the ideal gas constant.

Time advancement of Eqs. (5.3 - 5.5) is solved numerically using standard first-order finite-difference discretization and is advanced at a diffusive CFL constraint. Spatial discretization is second order on a uniform grid and formally first order on the currently used non-uniform grid. An adaptive mesh approach is used, such that the merging and splitting of grid cells is performed in a manner that conserves fluxes of transported quantities: mass, momentum, and energy. The grid is adapted based on a nominally uniform distribution of grid points along the arc length of the (centered and scaled) velocity, heat release rate, and species profiles [66]. A minimum grid cell size of  $8 \mu\text{m}$  is used, which is sufficiently small that no significant differences in results are observed when using a minimum grid cell size of  $4 \mu\text{m}$ . The ratio of Kolmogorov length to  $8 \mu\text{m}$  minimum cell size allowed is 2.35. The minimum cell size allowed is set prior to the simulation and controlled during time advancement. If the minimum cell size criteria is violated, then mesh adaptation is performed and cells are merged conserving mass, momentum, etc. The integration of the mean chemical source terms (used in the explicit time advancement) is performed with a high order implicit method using the most recent version of the CVODE code of the SUNDIALS package [40]. This eliminates chemical stiffness and allows advancement at a diffusive CFL. Thermodynamic and transport properties as well as reaction rates are calculated using the C++ interface of the CANTERA software package [36]. In this study the hydrogen combustion mechanism proposed in [61] that contains 21 reactions and 9 species is used.

## 5.2 TURBULENCE MODEL

In ODT, the turbulent motions that accelerate mixing are modeled through a series of stochastic rearrangement events. These events may be interpreted as

the model analog of individual turbulent eddies which are referred to as ‘eddy events’ or simply ‘eddies’. Each eddy event interrupts the time advancement of other processes and an instantaneous transformation is applied to the property profiles over some spatial interval  $(x_0, x_0 + l)$ . The eddy event is described in detail in Sec. 3.2.2.

### 5.3 COUNTERFLOW SUBMODELS

#### 5.3.1 Advection model

As noted in Sec. 3.2, stand-alone ODT represents flow advancement in the dominant direction of mean property variation and is applicable mainly to flows that have such a direction. In thin shear flows such as jets and mixing layers, this direction is transverse relative to the mean flow, and an ODT domain oriented in this direction can be validly formulated as a closed system provided that temporal or spatial (streamwise) advancement is implemented in accordance with the experimental or DNS configuration. In spatially developing cases, ODT can be viewed as representation of flow evolution along a Lagrangian line of sight that is advected downstream.

In a counterflow, mean property variation is primarily along the streamwise direction, so the ODT domain is the axial line. This line, viewed as a thin cylinder, is subject in a counterflow to inflow from the jet nozzles at the ends of the cylinder and corresponding net lateral outflow to conserve cylinder volume. Accordingly, an advection model needs to be introduced to transport incoming fluid from the nozzles towards the stagnation point and to expel mass from the ODT line as the fluid moves towards the stagnation point. The fluid expulsion required here by the counterflow configuration is a fundamental difference between the current and previous ODT formulations. The additional modeling that is needed introduces some further empiricism into ODT. The present study is in part intended to serve as an introduction and an initial validation of this additional modeling.

The cell faces are displaced with advection velocity  $u_1^A(x)$ , given by

$$u_1^A(x) = u_1(x) + u_1^D(x), \quad (5.9)$$

where  $u_1(x)$  is the ODT online velocity component time advanced in Eq. (5.3) and  $u_1^D(x)$  is the dilatation velocity introduced in Sec. 5.3.2 and given by Eq. (5.13). The advecting velocity is thus the sum of two contributions, one that is unrelated to density changes and one that is caused by density changes. The total ODT axial advection then consists of eddy events (maps) and  $u_1^A(x)$ .

To model the effect of the velocity decelerating towards the stagnation point, a pressure source term,  $\beta$ , in Eq. (5.3) is prescribed by

$$\beta(x) = u_1 \cdot \frac{\partial u_\beta}{\partial x}. \quad (5.10)$$

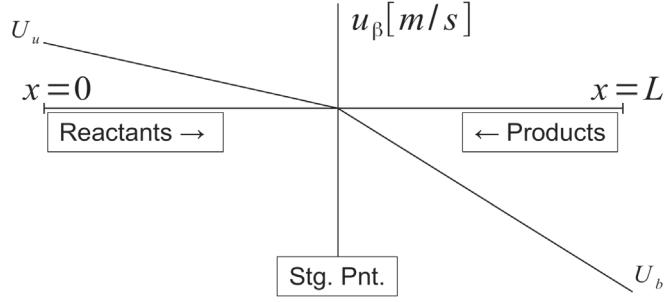


Figure 5.1: Shape function for pressure source term with prescribed stagnation point location.  $U_u$  and  $U_b$  are the mean inlet velocities of the reactants and products respectively.

The shape function for  $u_\beta$  is shown in Fig. 5.1, where the simplified model linearly decelerates the incoming velocity from the nozzles towards the prescribed stagnation point. The stagnation point location is an empirical input parameter.

### 5.3.2 Dilatation model

ODT operates on a 1D line between the two nozzles. There is expansion/contraction occurring due to temperature-induced density changes. The pressure remains constant and therefore a decision about how much dilatation to keep on the 1D line or inversely how much to expel must be made. Starting from the continuity equation in Lagrangian form, the preliminary dilatation velocity  $\hat{u}_i^D$  is first identified using

$$\frac{D\rho}{Dt} + \rho \frac{\partial \hat{u}_i^D}{\partial x_i} = 0 \quad (5.11)$$

in which the  $x$ ,  $y$  and  $z$  directions correspond to the respective indices  $i \in \{1, 2, 3\}$ . Solving for the preliminary dilatation velocity  $\hat{u}_1^D$  in  $x$

$$\hat{u}_1^D(x) = - \int_0^x \alpha \frac{1}{\rho} \frac{D\rho}{Dt} dx, \quad (5.12)$$

where  $\alpha=1/3$  is the fraction of the added volume that is kept on the line. For alpha, 1/3 is chosen based on the reasoning that in a turbulent field, on average 1/3 of the added volume is in the  $x$  direction. For the final dilatation velocity  $u_1^D$ , the boundary condition constraint dictated by the counterflow configuration,  $u_1^D(0) = u_1^D(L) = 0$  at the inlets, is imposed by linearly redistributing the total preliminary dilatation

$$u_1^D(x) = - \int_0^x \alpha \frac{1}{\rho} \frac{D\rho}{Dt} dx - \frac{x}{L} \cdot \hat{u}_1^D(L). \quad (5.13)$$

Fig. 5.2 shows schematically the preliminary and final dilatation velocity profiles over the domain for laminar flow.

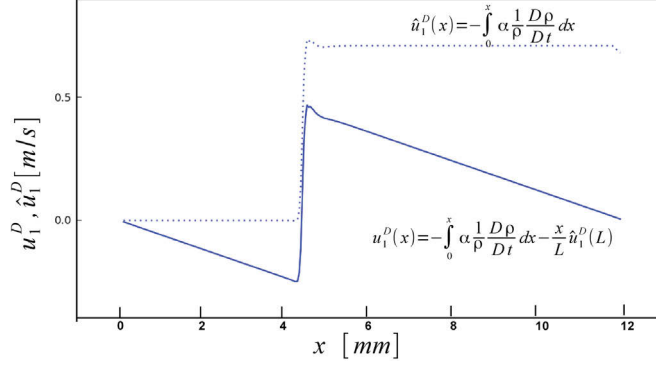


Figure 5.2: Preliminary and final dilatation velocity profiles for a notional laminar flow.

### 5.3.3 Darrieus-Landau instability model

Planar flames are intrinsically unstable due to acceleration of the variable-density fluid caused by thermal expansion across the burning front. This is the Darrieus-Landau (DL) instability, analogous to the Rayleigh-Taylor (RT) instability that develops when heavy fluid is above light fluid in a gravitational field (see Appendix B for a detailed description of the physics). This analogy allows an existing ODT representation of the RT instability [35] to be modified in order to incorporate the DL instability mechanism into ODT. Namely, a formal analog of gravitational potential energy is introduced. It is based on the equivalence of downward (negative) gravity and upward (positive) acceleration. In the current case, this implies that the constant acceleration of gravity is replaced by the varying time rate of change of the advecting velocity  $u_1^A(x)$ , defined as  $\alpha(x) = \partial u_1^A(x)/\partial t$ . Based on [35], it then follows that the associated potential energy change resulting from triplet mapping the accelerating variable-density flow is

$$E_{pe}^{DL} = \frac{8}{27} \int_{x_0}^{x_0+l} \alpha_{DL}(f(x)) \cdot K(x) \cdot (\rho(f(x)) - \bar{\rho}) dx, \quad (5.14)$$

where the factor  $8/27$  arises due to the variable density formulation and  $\bar{\rho}$  is a reference density defined as the average density over the interval  $[x_0, x_0 + l]$ . This potential energy change is nonzero only where the density varies, as it is the interaction of the dilatation-induced pressure gradient and the density gradient that is the cause of this instability mechanism.  $E_{pe}^{DL}$  is not a potential energy change in the same sense as in a buoyant flow, because it is not based on an external energy source. For this reason, it is only used to affect the probability of acceptance of an eddy, but it does not change the total kinetic energy during the energy redistribution step of the eddy event. It is however, a formal analog to the treatment of energy in the buoyant flow, and therefore a tunable coefficient is not required. Reflecting the analogy to gravitational potential energy,  $E_{pe}^{DL}$  is subtracted from the available kinetic energy when computing eddy likelihood as indicated in Eq. (3.27).

The DL instability is not specific to the counterflow configuration nor is it inherently a finite-Mach-number effect, so a representation of the instability should be incorporated into any ODT formulation involving unsteady dilatation within the ODT domain, irrespective of Mach number. The DL model was first introduced in [44] and shown to provide quantitatively good results for the simulation of ignition times in a turbulent homogeneous-charged compression-ignition (HCCI). It has also been used in [80] and shown to improve results for modeling flame propagation in fuel beds of wildland fires. In Appendix D, it is discussed further in the context of ODT modeling of flow acceleration effects.



## COUNTERFLOW CONFIGURATION

A reactant-to-product counterflow configuration is investigated, which consists of two axisymmetric, opposed nozzles of internal diameter  $D=12.7$  mm separated by a distance  $L_x=12.0$  mm as shown in Fig. 6.1. The flow arrangement consists of a turbulent stream of premixed reactants supplied through the left nozzle at a volumetric flow rate of  $Q_u=110$  LPM at an inlet temperature of  $T_u=294$  K, and a laminar stream of hot combustion products in equilibrium at  $T_b=1475$  K supplied through the right nozzle. The volumetric flow rate of the reactants fueling the stoichiometric flame, measured at 294 K, is  $Q_b=85$  LPM. The thermochemical state of the product stream is obtained by taking the products of a stoichiometric hydrogen and air mixture with adiabatic flame temperature 2388 K and cooling it under constant pressure to 1475 K. The reactant stream is shielded from the ambient air by an annular co-flow of nitrogen, supplied at 85 LPM. Combustion of a lean mixture of hydrogen and air (79 %  $N_2$  and 21 %  $O_2$  by volume) at an equivalence ratio of  $\phi_u=0.4$  and adiabatic flame temperature of 1723 K at 101.3 kPa flowing against a hot stream of combustion products generated by a stoichiometric flame with adiabatic flame temperature 2388 K is established at an elevated turbulent Reynolds number and bulk strain rate in a compact cylindrical volume and away from solid boundaries. At the simulated conditions, the freely propagating laminar flame speed and nominal thickness of a one-dimensional flame are  $S_u^L=0.22$  m/s and  $\delta_f = D_{th,u}/S_u^L=0.141$  mm, respectively, where  $D_{th,u}$  is the thermal diffusivity of the unburnt mixture. The laminar flame time is  $\tau_c=\delta_f/S_u^L=0.64$  ms.

The bulk velocities of the two streams are computed from the volumetric flow rate and the nozzle diameter. Under these conditions the mean bulk strain rate is  $\alpha=2 \cdot U_u/L_x=2400$  s<sup>-1</sup> and the residence time is  $\tau_R=0.5 \cdot L_x/U_u=0.4$  ms. The reactant side inlet turbulence is characterized by turbulence intensity,  $u'/U_u=0.35$ , and an integral length scale,  $l'/D=0.30$ , resulting in an eddy turn-over time,  $\tau'_t = l'/u'=0.752$  ms. The physical and numerical parameters of the simulations are summarized in Table 6.1.

## 6.1 ODT SET-UP

The ODT domain spans the 1D line between nozzle orifice centers,  $L_x=12$  mm. To produce the reactant side turbulent inlet conditions, velocity fluctuations are superimposed on the mean inlet velocity at the reactant's stream inlet. These fluctuations are obtained from a homogeneous isotropic turbulence field generated prior to the simulation, based on a prescribed Passot-Pouquet energy spectrum [83]. As empirical input, the stagnation point location used in

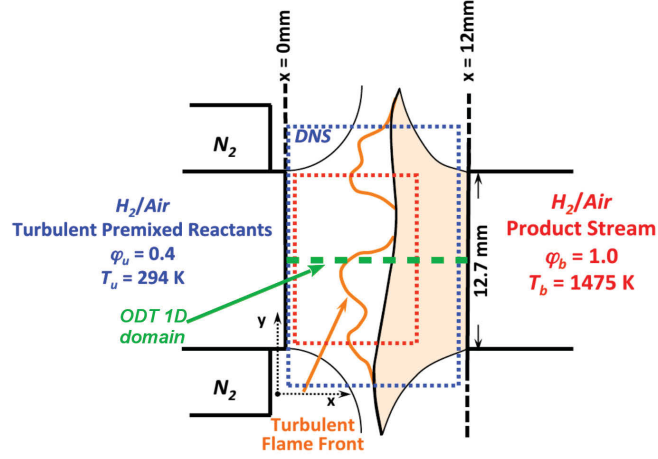


Figure 6.1: Schematic representation of the investigated counterflow burner. The ODT domain, denoted by the green dashed line, spans the 1D domain between nozzle orifice centers. The DNS data were obtained in a  $12 \times 17.5 \times 17.5 \text{ mm}^3$  rectangular volume denoted by the blue dotted box in the span-wise mid-plane. The DNS diagnostics window in which the analysis of the data is performed is confined to the  $8.4 \times 8 \times 8 \text{ mm}^3$  volume shown in red so that the DNS results are not biased by the  $\text{N}_2$  co-flow. The figure is adopted from [71].

Table 6.1: Numerical and physical parameters

Jet diameter ( $D$ )	12.7 mm
Mean inlet velocity of reactants ( $U_u$ )	14.47 m/s
Mean inlet velocity of products ( $U_b$ )	49.97 m/s
Temperature of reactants ( $T_u$ )	294 K
Temperature of products ( $T_b$ )	1 475 K
Turbulence intensity ( $u'/U_u$ )	0.35
Integral length scale ( $l'/D$ )	0.30
Bulk strain rate ( $\alpha = 2U_u/L_x$ )	$2\,400 \text{ s}^{-1}$
Jet Reynolds number ( $Re_{jet} = U_u D/\nu_u$ )	10 400
Turbulent Reynolds number ( $Re_t = u'l'/\nu$ )	1 100
Karlovitz number ( $Ka = (l'/\delta_f)^{-1/2}(u'/S_u^L)^{3/2}$ )	26
Damköhler number ( $Da = Re_t^{1/2}/Ka$ )	1.2
Kolmogorov length scale ( $\eta/D = Re^{-3/4}l'/D$ )	0.00157
DNS domain ( $L_x \times L_y \times L_z$ )	$0.95D \times 1.48D \times 1.48D$
DNS grid points ( $N_x \times N_y \times N_z$ )	$432 \times 640 \times 640$
ODT domain length ( $L_x$ )	12.0 mm

Eq. (5.10) was taken to be the mean DNS stagnation location, 4.8 mm. Additionally, ODT has three adjustable parameters that need to be specified:

- Viscous penalty parameter  $Z=0.1$ .
- Eddy frequency parameter  $C=3.5$ .
- Maximum eddy size allowed is 5 mm, which corresponds to  $1.3 \cdot l'$ .

These parameters were chosen by matching spatial and state-space statistics to DNS results. A parameter sensitivity study is conducted in Sec. 7.3.

## 6.2 DNS PHYSICAL AND NUMERICAL PARAMETERS

The DNS set-up is detailed in [71], here only the key points are re-stated. The three-dimensional physical extent of the computational domain is  $0.95D \times 1.48D \times 1.48D$  and the domain is discretized into  $432 \times 640 \times 640$  grid cells in the  $x$ ,  $y$  and  $z$  directions, respectively. An equidistant Cartesian mesh is used in all three directions where the resolution adequately resolves both the flame and turbulent flow field, resulting in a uniform spacing of  $D/dx=470$ . To produce the reactant side turbulent inlet conditions, velocity fluctuations are superimposed on the mean inlet velocity at the reactants stream inlet. These fluctuations are obtained from a spatially evolving turbulent field obtained from an auxiliary three-dimensional DNS of a non-reactive homogeneous isotropic field performed with the Sandia 3D Direct Numerical Solver S3D [122]. A homogeneous isotropic turbulence field is initially generated using the method described by [98], based on a prescribed Passot-Pouquet energy spectrum [83] that satisfies continuity and subsequently evolves until turbulence is established.



## RESULTS

In this section a macroscopic description of the overall flame burning behavior is provided from a statistical description of the turbulent flame and results from ODT and DNS are compared. The Favre mean of a variable,  $\tilde{\phi}$ , is defined as  $\tilde{\phi} = \overline{\rho\phi}/\bar{\rho}$  where the overbar denotes ensemble temporal averaging defined as:

$$\phi(x, y) = \frac{1}{N_t} \sum_{n=1}^{N_t} \phi(x, y, t_n). \quad (7.1)$$

$N_t$  is the number of samples in the statistically stationary period in the simulation over which ensemble averaging is performed.

The results section is outlined as follows: in Sec. 7.1 the 1D laminar strained flame results are presented. First, the evolution of the maximum temperature and maximum heat release rate are presented as a function of bulk strain rate. Then, for the bulk strain rate of the current counterflow configuration the 1D laminar strained flame results as a function of the nozzle separation distance are shown. In Sec. 7.2.1, spatial statistics of the turbulent flame are compared between ODT and DNS results. In Sec. 7.2.2, mixing rates are compared by looking at the scalar dissipation rate. In Sec. 7.2.3, flame extinction/ignition characteristics are discussed. Sec. 7.2.4 compares scatter plots of heat release rate and species conditioned on temperature to show the range of results obtained by ODT and DNS. Sec. 7.2.5 tests for superadiabaticity by showing the equilibrium temperature reached for mixture states taken from the DNS and ODT results. Sec. 7.2.6 looks at the effects of differential diffusion. For a more stringent comparison between ODT and DNS, Sec. 7.2.7 compares the mean and RMS profiles of the scatter plots. Finally, in Sec. 7.3 a sensitivity study to ODT input parameters is presented.

## 7.1 LAMINAR FLAME RESULTS

Prior to the application of ODT to the turbulent counterflow flame, the response of the flame to strain rate fluctuations was examined using laminar flame simulations. The laminar ODT simulations include the advection and the dilatation model, but not the ODT eddy events nor the Darrieus-Landau instability model. For these ODT simulations, the strain rate was progressively increased from  $200 \text{ s}^{-1}$  to  $10\,000 \text{ s}^{-1}$ , while the composition and temperature of the counterflowing streams and the nozzle separation distance were held constant and identical to the three-dimensional turbulent flame parameters investigated with DNS. The dependence of the maximum heat release rate and maximum temperature on bulk strain rate is shown in Fig. 7.1. It shows that

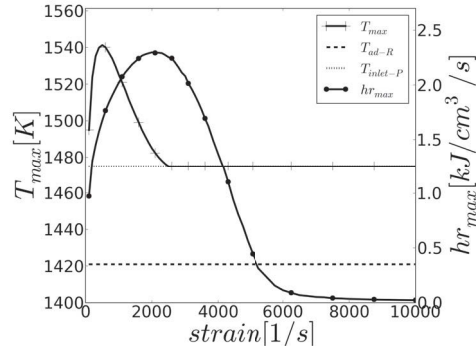


Figure 7.1: Steady state solutions of the 1D laminar strained flame as a function of bulk strain rate. ODT results for maximum heat release rate and maximum temperature are plotted. Additionally, the reactant side adiabatic flame temperature,  $T_{ad-R}$ , and the product side inlet temperature,  $T_{inlet-P}$ , are shown.

there is a non-monotonic dependence of heat release rate and temperature on strain rate. For low-to-moderate strain rate, up to approximately  $2400 \text{ s}^{-1}$ , the peak heat release rate increases with increasing strain rate as expected from effects of nonequidiffusivity [60]. At higher strain rate, the flame is pushed closer to the stagnation plane and the temperature and heat release rate decrease with increasing strain rate. The maximum temperature does not decrease below  $1475 \text{ K}$ , as this is the product side inlet temperature. The flame response to strain rate as shown in Fig. 7.1 is described by a stretched S-curve, as opposed to a folded S-curve when extinction is abrupt [28, 67]. The gradual extinction occurs due to the temperature of the product stream, which is higher than the adiabatic temperature of the lean premixed flame and thus provides back support that prevents the flame from extinguishing abruptly. The stretched S-curve lacks a turning point and results in an ambiguous definition of the extinction limit and the corresponding extinction strain rate. Therefore, in the present study, following [71], the flame is considered to be extinguished when the instantaneous heat release rate is lower than 0.5 percent of the maximum heat release rate of the strained laminar case which corresponds to  $0.01 \text{ kJ/cm}^3/\text{s}$ .

In Fig. 7.2, ODT results for the one-dimensional strained laminar flame ( $a=2400 \text{ s}^{-1}$ ) are compared to results from the OPPDIF solver of the CHEMKIN package [70]. This strain rate corresponds to the bulk strain rate of the current counterflow configuration. Results are centered about the stagnation point, with OPPDIF results offset by  $0.078D$  to obtain a clearer comparison. It can be seen that the normalized axial velocity profile  $u/U_u$  decreases from unity at the reactants nozzle to  $-3.45$  at the counterflowing product stream nozzle tip. Within the domain, the ODT velocity profile, and therefore local strain rate, underestimates the OPPDIF results. This shows that the linear approximation for the pressure source term in Eq. (5.10) does not accurately reflect the spatial variation of pressure in OPPDIF. However, near the stagnation point  $x/D=0$  the velocity profile shows good agreement with OPPDIF data. In this region the dilatation model has a large influence on the velocity field. The tem-

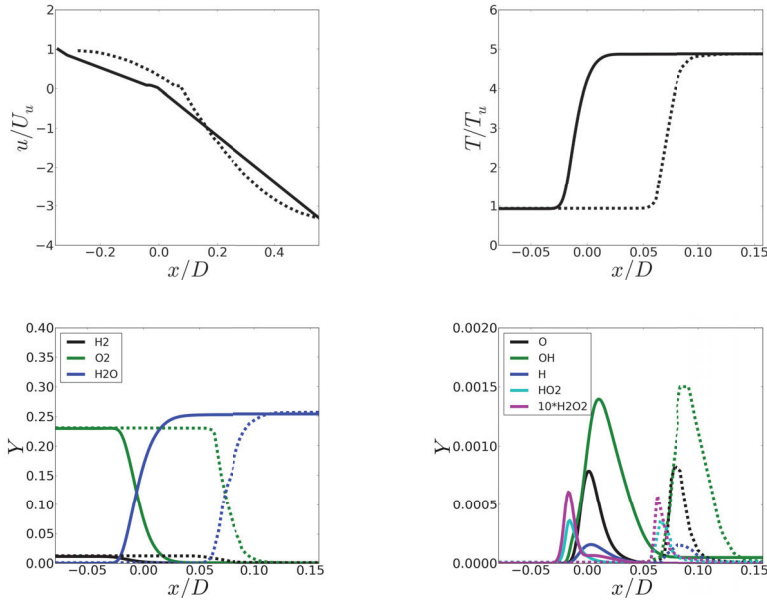


Figure 7.2: Laminar strained flame results. Top: Axial velocity (left) and temperature (right) as a function of the axial distance normalized by the jet diameter. The velocity  $u$  is normalized by the bulk velocity of the reactants  $U_u$  and the temperature by the reactant inflow temperature  $T_u$ . Bottom: Major (left) and minor (right) species mass fractions as a function of the axial distance. Reactant and product streams are on the left and right side of the plot, respectively. On the  $x$ -axis, zero is the stagnation point location. The solid lines represent the ODT results and the dashed lines the corresponding OPPDIF results. To obtain a clear visual comparison, OPPDIF results are offset by  $0.078D$  in all plots and temperature and species plots are zoomed in.

perature and major and minor species profiles are almost identical. Due to the previously mentioned lower strain rate encountered by ODT, a very slight discrepancy is observed, whereby the ODT profiles are more rounded. Here, the lower strain rate allows diffusion to broaden the ODT curves slightly more.

## 7.2 TURBULENT FLAME RESULTS

### 7.2.1 Spatial comparisons

Favre velocity and scalar means and variances are presented in this section. The Favre mean and RMS of the normalized axial velocity, temperature, and major ( $H_2O$ ,  $H_2$ ,  $O_2$ ) and minor ( $O$ ,  $OH$ ,  $H$ ,  $H_2O_2$ ,  $HO_2$ ) species as a function of the stagnation point location are presented in Fig. 7.3. It can be seen that the mean ODT and DNS velocity profiles are very similar to the laminar strained flame ODT and OPPDIF velocity profiles respectively. The ODT and DNS normalized RMS of the axial turbulent fluctuations is  $\widetilde{u_{rms}}/U_u=35\%$  at the exit of the reactant jet.

In the DNS, the normalized RMS of the axial turbulent fluctuations increases by a factor 1.85 towards the stagnation plane, attaining a maximum value at  $x/D=0.06$ , and vanishing in the product stream as expected. In ODT, the RMS first decreases and then recovers to approximately the same level at the stagnation plane. For ODT, the fluctuations decrease from the inlet because of the constant pressure source term applied that decreases the velocity amplitude from the inlet towards the stagnation point. Near the stagnation point, the generated turbulence then increases the fluctuations.

The Favre mean normalized temperature  $\tilde{T}/T_u$  increases monotonically between unity and five between the cold and hot boundaries and is approximately 2.5 at the stagnation plane. At this axial location, the normalized RMS approaches 97 % of its maximum value of 1.72 for the DNS while for ODT it approaches its maximum value of 1.57. The distribution of the mean temperature and its fluctuations reveal that the mean thickness of the mixing layer between the cold reactant and the hot product stream is 0.41D for the DNS, while it is 0.69D for ODT. The mixing layer is defined to start at the location where  $\tilde{T}_{RMS}$  reaches 1 % of  $T_u$  and ends where  $\tilde{T}_{RMS}$  drops again below this value. For ODT, the broadness of the thickness is directly related to the maximum allowed eddy size of 0.39D (5 mm), as the extent of the temperature fluctuation manifests itself 0.39D from the stagnation point into the product side. Therefore, if the maximum eddy size was set larger, intermittency would result in eddies that broaden the mixing layer even more (see Sec. 7.3). The significant levels of temperature fluctuations, i.e. up to 500 K for DNS and 460 K for ODT, correlate with the spatially and temporally intermittent flame attenuation events that occur near the stagnation plane. The heat release rate and radical production rates are sensitive to temperature fluctuations, amplified through the Arrhenius chemical effect.

Major species mean profiles vary monotonically between the two nozzles while minor species feature distributions centered around the stagnation plane. Contrary to the 1D laminar flame profiles at the same bulk strain rate, the mean minor-species spatial distributions exhibit maxima that are nearly collocated and the extent of the reaction zone is approximately 2.3 times wider than the corresponding laminar flame. This is expected as Karlovitz and the Damköhler number are  $Ka=26$  and  $Da=1.2$  respectively, which indicate that the current turbulent flame is in the thin reaction zone regime. The smallest eddies can enter the reactive-diffusive flame structure, however these small eddies are still larger than the reaction zone thickness and can therefore not penetrate into that layer. The second moments of all species are zero at the jet exits and increase with axial distance, attaining their maximum in the vicinity of the stagnation plane where the flame resides.

Comparing ODT temperature and species profiles with DNS, it is seen that although ODT is a reduced order model it is able to achieve a good quantitative comparison for both mean and RMS temperature and species results. RMS profiles for temperature and major species are slightly underpredicted. This can be explained by noting that the axial movement of the stagnation point is larger for the DNS than for ODT. In the DNS the mean stagnation



point is located 4.8 mm from the reactant side nozzle, and this was used as empirical input for ODT (see Sec. 6.1). The RMS of the stagnation point location is  $0.06D$  and  $0.04D$  in the DNS and ODT respectively. For the DNS, the larger stagnation plane motion increases RMS values but is not mixing. In ODT, the axial movement of the stagnation plane is seen to a lesser degree due to the prescribed constant pressure shape function for the advection velocity. Minor species mean profiles however, have peaks about two times that of the corresponding DNS peaks. This indicates that burning in ODT is more localized about the stagnation plane.

### 7.2.2 Scalar dissipation rate comparisons

The scalar dissipation rate can be physically interpreted as a mixing rate, or equivalently as a rate at which scalar fluctuations are destroyed [107]. Therefore, to look at mixing decoupled from burning, Favre averaged results of the nitrogen dissipation rate are presented next. The nitrogen concentration differs in the reactant and product inlet streams and therefore provides a simple conserved scalar that is representative of conserved scalar dissipation rates. In Fig. 7.4 the Favre averaged scalar dissipation rate as a function of axial distance and as a function of Bilger's mixture fraction [9] is plotted. Spatial results show that ODT is in reasonable agreement with the DNS although it underestimates peak mixing levels. The degree of accuracy of ODT seen in Fig. 7.4 is consistent with, and an important determining factor of, the accuracy of the statistics of various thermochemical quantities that are presented here. Additionally, this demonstrates that the ODT formulation captures relevant fluctuation properties of full 3D turbulence in 1D.

### 7.2.3 Flame attenuation

The nature of extinction that is observed in this flame is not abrupt extinction of flame regions, but rather gradual attenuation. A flame experiences attenuation when portions that are supposed to be burning vigorously experience a drop in heat release rate values. To provide a measure of this, a progress variable is first defined:  $p.v. = (Y_{H_2} - Y_{H_2,u}) / (Y_{H_2,u} - Y_{H_2,b})$ , where  $Y_{H_2,u}$  and  $Y_{H_2,b}$  are the reactant and product side inlet  $H_2$  mass fractions respectively. In Fig. 7.5 (left) heat release rate against  $p.v.$  for the 1D strained laminar flame computed with OPPDIF is plotted. From this curve it is seen that peak heat release rate for the laminar flame is reached in the vicinity of  $p.v.$  in range from 0.5 to 0.6. This  $p.v.$  range demarcates portions that should be burning well. In Fig. 7.5 (right) the probability density function (pdf) of heat release rate on the center line conditioned on being in this  $p.v.$  range is plotted. The heat release rate range for the laminar strained flame (dotted line) in this  $p.v.$  range is depicted from the left plot for comparison. The DNS result (dashed line) shows lower heat release rate values which denote significant attenuation. The ODT pdf (solid line) shows excellent agreement with the DNS data. This gives a quantitative demonstration that attenuation characteristics

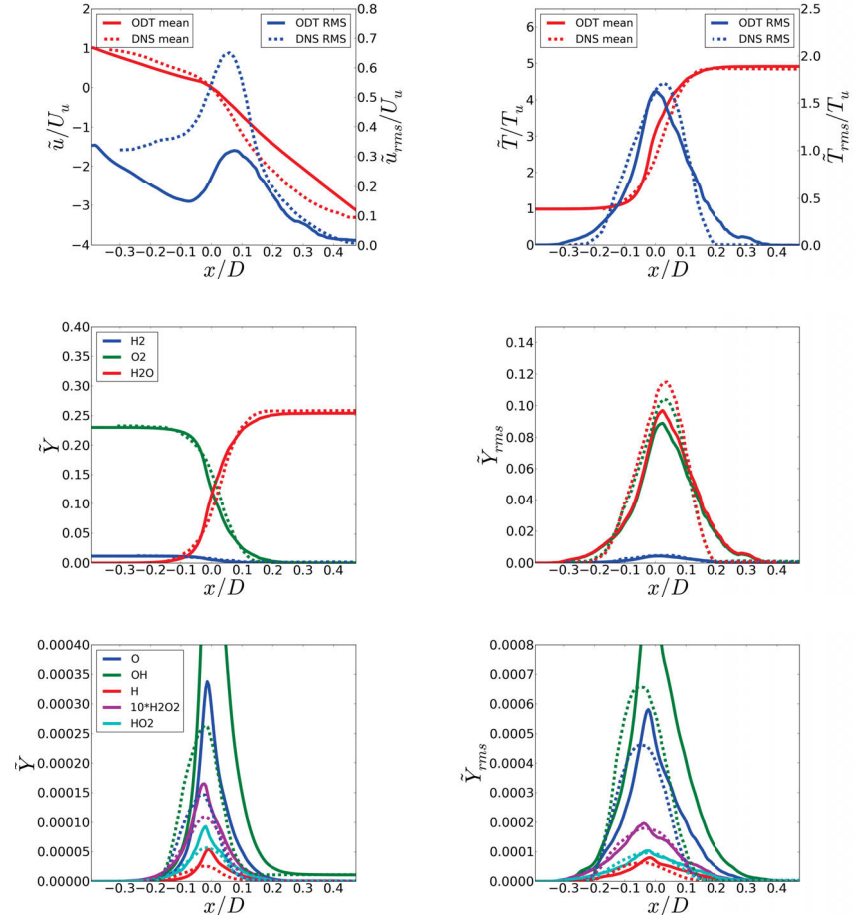


Figure 7.3: Top: Favre mean and RMS of the axial velocity and temperature as a function of the axial distance normalized by the jet diameter. The velocities are normalized by the bulk velocity of the reactants  $U_u$  and the temperature by the reactant inflow temperature  $T_u$ . Density weighted major (middle) and minor (bottom) mean (left column) and RMS (right column) species mass fractions as a function of the axial distance normalized by the jet diameter. Solid and dotted lines represent ODT and DNS results respectively. Results are offset on the  $x$  axis, such that  $x/D = 0$  is the stagnation point for both ODT and DNS.

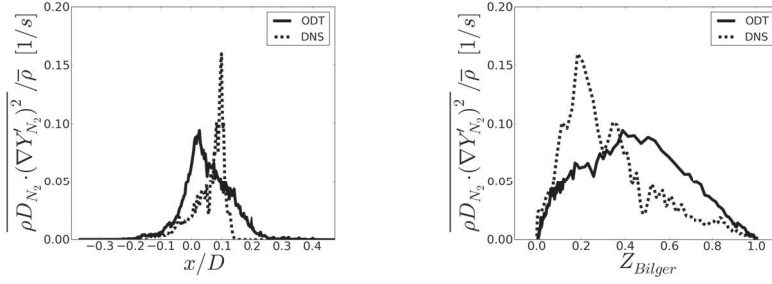


Figure 7.4: Favre averaged scalar dissipation rate as a function of the axial distance normalized by the jet diameter (left) and as a function of Bilger's mixture fraction (right). Solid and dotted lines represent ODT and DNS results respectively. Spatial results are offset on the  $x$  axis, such that  $x/D = 0$  is the stagnation point for both ODT and DNS.

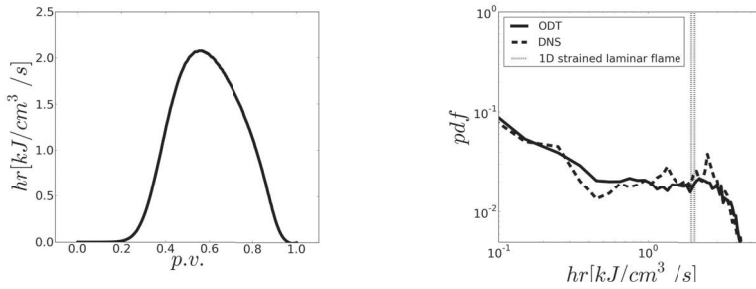


Figure 7.5: Left: Heat release rate on the center line plotted against progress variable ( $p.v.$ ) for the 1D strained laminar flame computed with OPPDIF. The progress variable is defined as  $p.v. = (Y_{H_2} - Y_{H_2,u}) / (Y_{H_2,u} - Y_{H_2,b})$ , where  $Y_{H_2,u}$  and  $Y_{H_2,b}$  are the reactant and product side inlet  $H_2$  mass fractions respectively. Right: Probability density function (pdf) of heat release on the center line conditioned on the  $p.v.$  in range 0.5-0.6. Solid line (ODT), dashed line (DNS), and the 2 dotted lines represent the heat release rate range for the 1D strained laminar flame in range  $p.v.$  between 0.5 and 0.6 (taken from the left plot).

in ODT are captured well. The DNS deviations from the ODT curve are mainly sharp peaks and troughs, possibly reflecting the greater statistical variability of the DNS relative to ODT rather than ODT modeling error. The heat release rate pdf curve conditioned on additional  $p.v.$  ranges (not shown) was also checked: 0.3-0.4, 0.4-0.5 and 0.6-0.7. These indicated some quantitative variations of heat release rate pdf shape from range to range, but at low heat release rate they all indicate the same rough power-law dependence seen for  $p.v.$  in the range 0.5-0.6, and also they all show good agreement between ODT and DNS.

#### 7.2.4 Scatter plot comparisons

Temperature-conditioned statistics are widely used to analyze the state-space structure of turbulent flames because they conveniently illustrate effects of

finite-rate kinetics that cause the thermochemical state to deviate from equilibrium. For ODT specifically, such statistics obtained from non-premixed configurations have proven useful and instructive [65, 91]. In addition to the novel features of the present ODT formulation (see Sec. 5.3), this study serves as the first detailed presentation of such statistics from ODT simulations of premixed combustion.

In Fig. 7.6 and Fig. 7.7 ODT and DNS scatter plots of heat release rate and major and minor species mass fractions conditioned over temperature are compared. Each value plotted represents a specific point in time and space. For the DNS, values from the center line were taken over 10 residence times 100 times per residence time, while for ODT, values over the entire domain were taken over 100 residence times 10 times per residence time. Therefore, the number of times the data was sampled at is the same for DNS and ODT, however ODT sampled for a longer run time but less frequently. The values for the corresponding strained ( $a=2400\text{ s}^{-1}$ ) laminar flame are shown for reference. The plots demonstrate that ODT is able to capture the full range of results seen by the DNS over the entire temperature range. It is observed that the calculation points for ODT are distributed in a band width that is in good agreement with DNS data at all temperatures. The most noticeable difference between ODT and DNS is in the heat release rate plot at temperatures below 1000 K. Here, a small number of points show higher heat release rates than indicated by DNS. A possible explanation is that this higher heat release rate level at low temperatures is an artifact of the instantaneous mappings, whereby unrealistic gradients are momentarily created that could affect the diffusion process. This shows that due to the stochastic nature of ODT, certain states can be obtained that are otherwise not obtained when the full Navier-Stokes equations are solved.

Scatter plots for major species  $\text{H}_2\text{O}$  and  $\text{O}_2$  compare well between DNS and ODT. The comparison for  $\text{H}_2$  shows that: 1) at temperatures below 1000 K, DNS has more points below the laminar line and 2) in general ODT has a wider band above the laminar line at all temperatures.

In general, in the DNS distinct structures at high temperatures that are not necessarily so prominent in the ODT results are seen. However, this is not a case of ODT not capturing these states, but rather that ODT captures additional states to those seen by the DNS that blur out the distinct shapes. Specifically looking at Fig. 7.6, and comparing the  $\text{O}_2$  plots, a distinct structure in the DNS at temperatures between 1500 - 1700 K is seen. In ODT, results in this temperature range are more broadly and smoothly spread than in the DNS. A possible explanation for this is that ODT simulated more diverse residence times than the DNS and therefore sees more states which blur out the sharp features in the DNS.

### 7.2.5 Superadiabaticity test

In Fig. 7.6, states with temperature up to approximately 1700 K are obtained. This is considerably higher than the product side inlet temperature of 1475 K

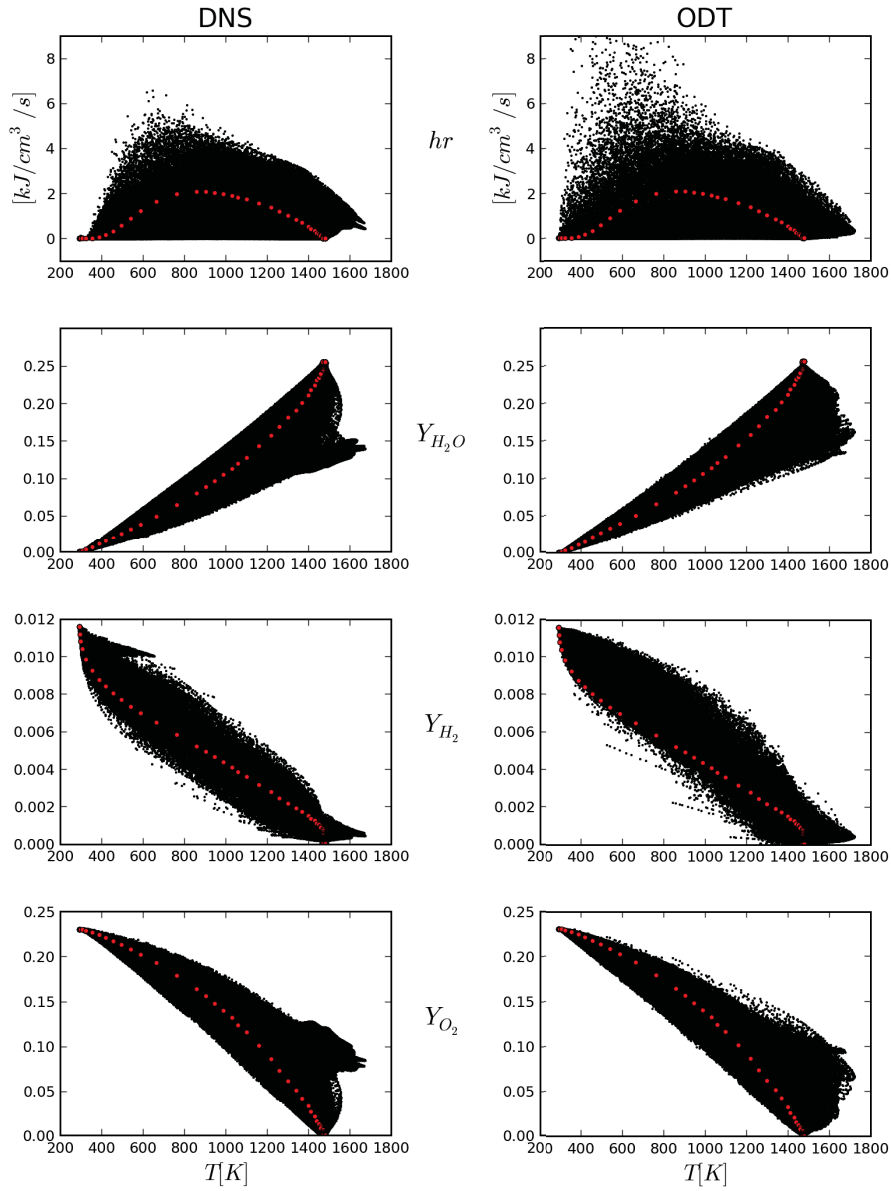


Figure 7.6: Scatter plots of heat release rate and major species mass fractions with temperature on the burner centerline. DNS (left), ODT (right). The red symbols represent the corresponding 1D strained laminar flame computed with OPPDIF.

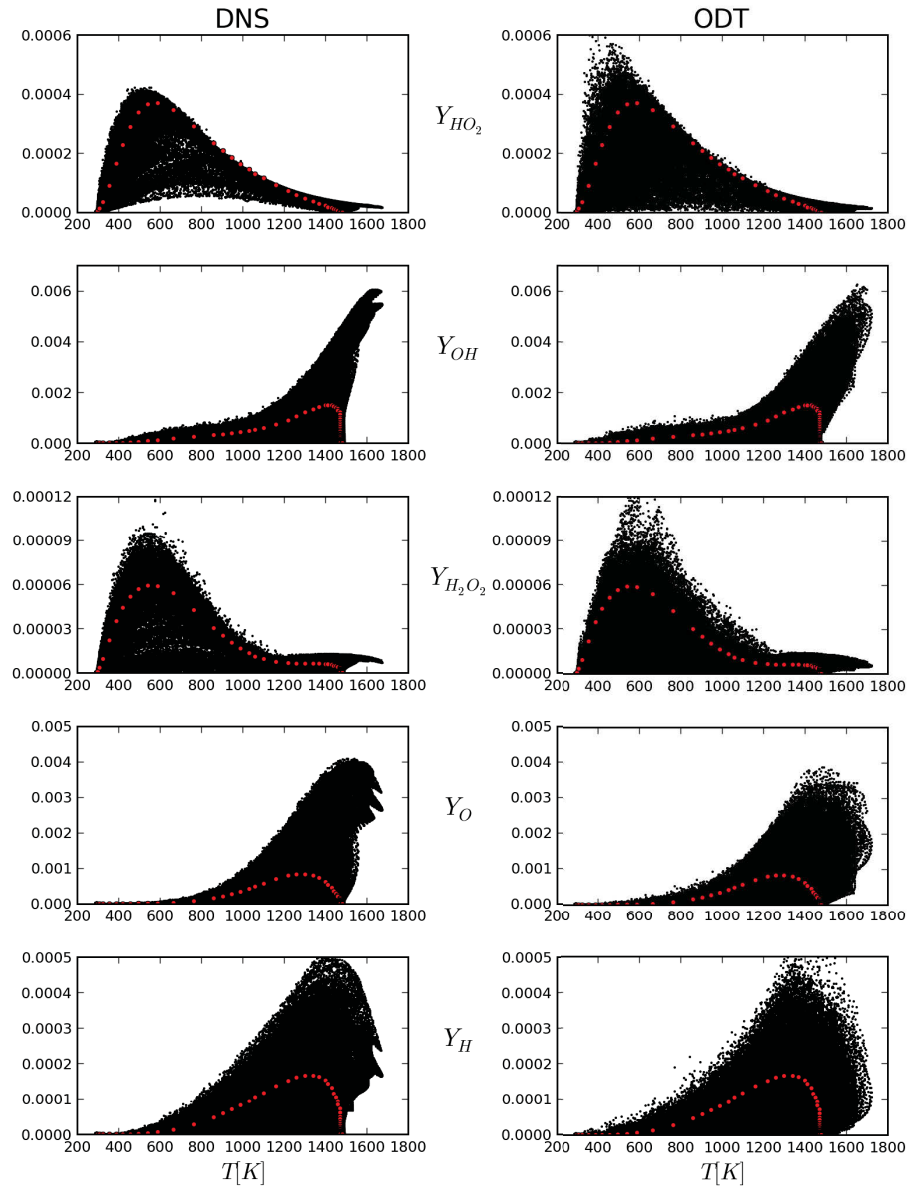


Figure 7.7: Scatter plots of minor species mass fractions with temperature on the burner centerline. DNS (left), ODT (right). The red symbols represent the corresponding 1D strained laminar flame computed with OPPDIF.

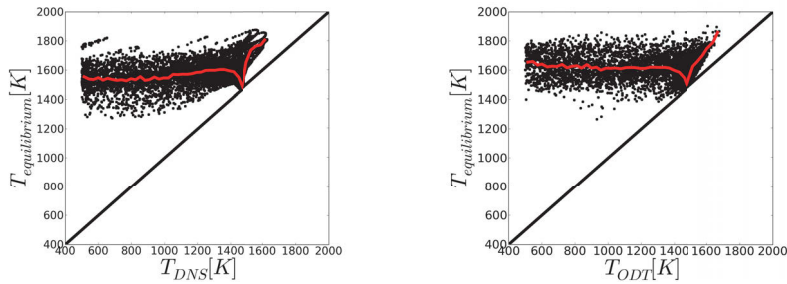


Figure 7.8: Equilibrium calculation for input states from DNS (left) and ODT (right) results. The red line represents the average equilibrium temperature for given input temperature.

and also above the reactant side adiabatic flame temperature of 1420 K. To test for superadiabaticity, temperature that exceeds the highest equilibrium temperature that is possible for any mixture of the two inlet states, each state above 500 K presented in Fig. 7.6 is taken as an input condition (pressure, temperature and species) and an equilibrium calculation is performed. The equilibrium temperature reached versus input temperature from DNS and ODT is shown in Fig. 7.8. Points on the diagonal line indicate no change in temperature (i.e. input mixture is at equilibrium). Points above the diagonal line indicate a temperature rise at equilibrium and points below indicate a temperature drop. No points are seen below the diagonal line for both DNS and ODT, indicating that superadiabaticity is not reached. The equilibrium temperature remains the same as the input temperature only for a group of points with initial temperature around 1475 K. These represent the product side inlet gas that is input at a state of equilibrium. All other points represent a mixture of the reactant and product side inlet states.

To facilitate the comparison between ODT and DNS results, the average equilibrium temperature reached for input temperature is additionally shown in red in Fig. 7.8. Comparing the ODT and DNS average equilibrium temperatures shows that for input temperatures below 1000 K, ODT reaches higher equilibrium temperatures. Differences in ODT and DNS species results below 1000 K have been highlighted in Sec. 7.2.4, here it is only noted that differences between ODT and DNS input states are amplified through the equilibrium calculation and lead to larger differences in the equilibrium states reached. Above 1000 K, the average equilibrium temperatures are similar.

### 7.2.6 Differential diffusion effects

Fig. 7.6 and 7.7 show that the turbulent flame reaches temperatures up to approximately 1700 K, whereas the laminar flame reaches a maximum peak temperature of 1540 K. A possible explanation for the turbulent flame reaching higher temperatures is that these temperatures are associated with differential diffusion (DD). Low molecular weight hydrogen (1.0 kg/kmol) species diffuse more rapidly than heavy oxygen (16.0 kg/kmol) and nitrogen (14.01 kg/kmol) species, in some instances increasing the  $H_2/O_2$  ratio creating a richer mixture.

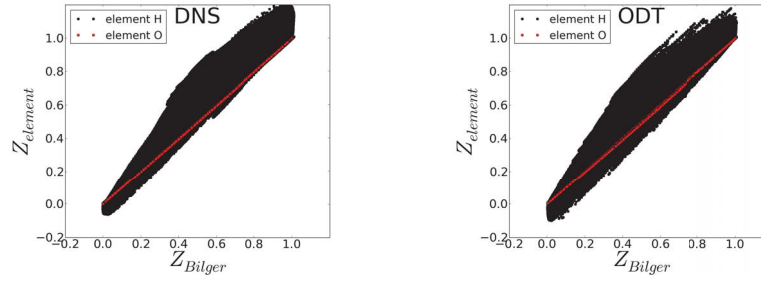


Figure 7.9: Scatter plot of element O (red) and element H (black) mixture fraction vs. Bilger's mixture fraction for DNS (left) and ODT (right).

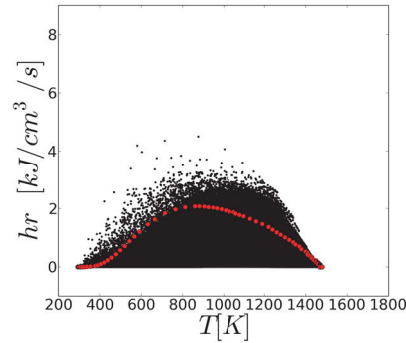


Figure 7.10: ODT scatter plot of heat release rate with temperature on the burner centerline with Lewis number of all species equal to 1. The red symbols represent the corresponding 1D strained laminar flame computed with OPPDIF.

To validate this claim, in Fig. 7.9 DNS and ODT results for element mixture fraction H and O versus Bilger's mixture fraction are first compared. It is seen that for both the DNS and ODT element H mixture fraction has values greater than and less than 1, while the Bilger's mixture fraction has values strictly between 0 and 1. This, and noting the difference between element H and element O mixture fraction, shows that DD effects are present. ODT results compare well to DNS data.

Having validated the ODT DD results, ODT is now re-run with the Lewis number of all species set to 1. Fig. 7.10 shows the scatter plot of heat release rate with temperature on the burner centerline and it is seen that temperatures above the laminar flame temperature are not obtained. This is an illustration that having validated ODT, ODT can be used to run parameter variations to look at questions of interest more quickly and easily than by running additional DNS cases.

### 7.2.7 State-space comparisons

For a more stringent comparison between ODT and DNS, mean and RMS plots conditioned on temperature for heat release rate and major and minor species are presented. A qualitative agreement is achieved in all of the cases, with



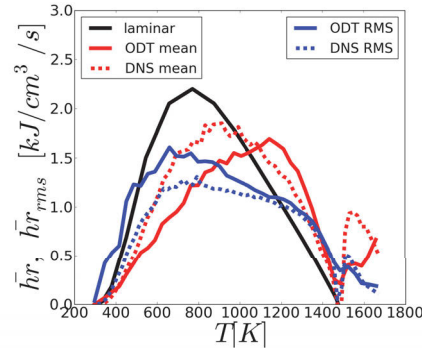


Figure 7.11: Temperature conditioned mean (red) and RMS (blue) of the heat release rate. Solid lines: ODT, dotted lines: DNS. The black line represents the corresponding 1D strained laminar flame computed with OPPDIF.

quantitative agreement for some of the mean and RMS profiles. In Fig. 7.11, heat release rate conditioned on temperature is compared. For reference, the strained laminar flame results are also shown. ODT mean results compare well to DNS for temperatures above 1000 K. For temperatures below 1000 K, ODT underestimates the heat release rate. A possible explanation for this is that in low temperature regions, the flame is weaker and more sensitive to strain fluctuations. ODT through its instantaneous maps can induce momentarily artificially high strains which disrupt the preheating process. RMS profiles show good qualitative comparison to DNS throughout the temperature range.

In Fig. 7.12, species conditioned on temperature are compared. In all cases, ODT gives good qualitative results for both mean and RMS profiles. From the plots it is seen that at low temperatures, below 1000 K, reactions involving the formation and consumption of  $\text{HO}_2$  and  $\text{H}_2\text{O}_2$  chemistry are important. Mean profiles here are again underestimated showing underignition at low temperatures.

### 7.3 PARAMETER SENSITIVITY STUDY

The DNS data is used to provide guidance on the selection of the ODT parameters listed in Sec. 6.1. Sensitivity analysis is performed in the context of Favre averaged spatial statistics and by collecting state-space statistics conditioned on temperature over 10 residence times from the DNS and ODT simulations. Statistical convergence has been ensured by verifying that the statistics from half the samples are indistinguishable from those from the full samples. The sensitivity of the ODT results to the eddy frequency parameter  $C$ , the maximum allowed eddy size  $L_{\text{max}}$ , and the stagnation point location is presented in Fig. 7.13. Favre averaged temperature fluctuations and heat release rate conditioned on temperature are shown because they characteristically represent spatial and state-space statistics. A sensitivity study for the viscous penalty parameter  $Z$  is not shown, as  $Z$  was chosen small enough such that results are insensitive to it.

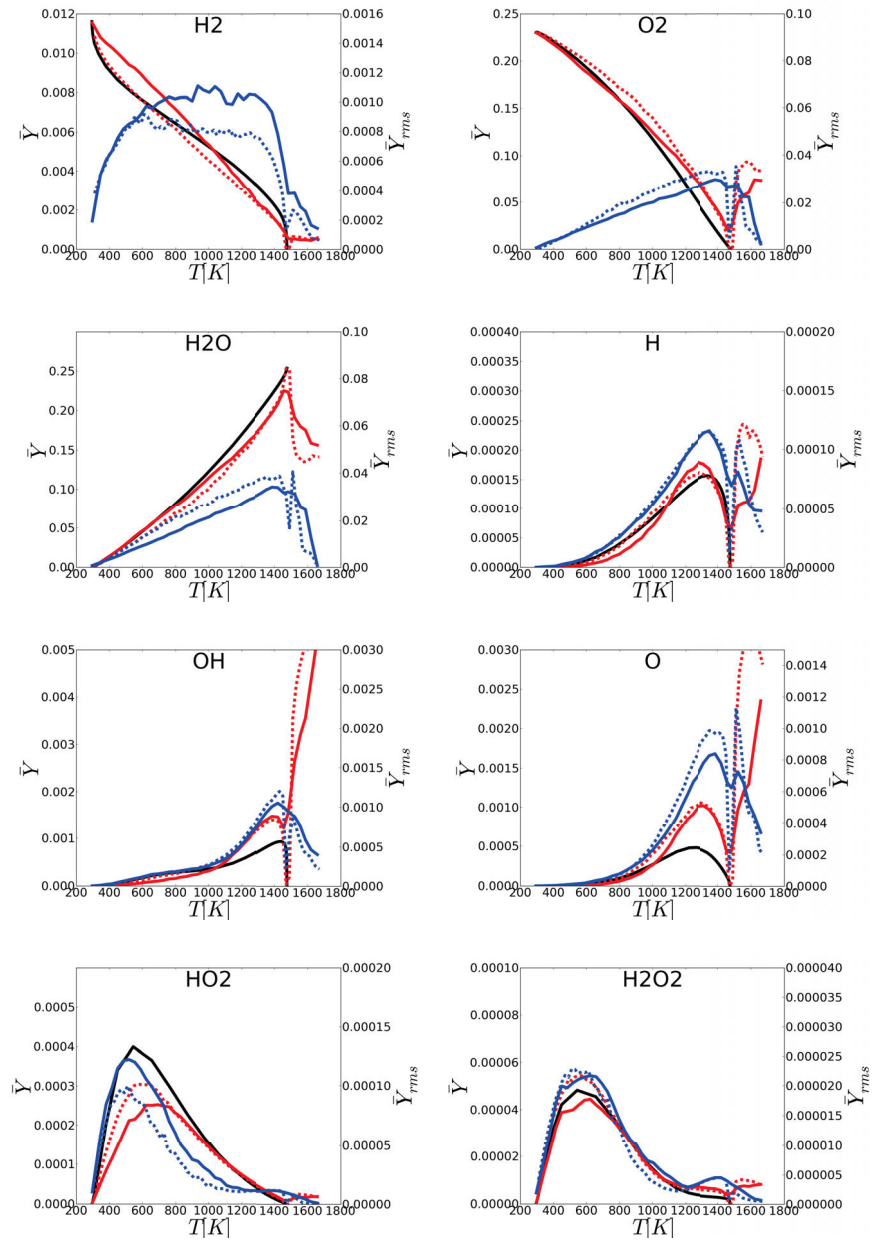


Figure 7.12: Temperature conditioned mean (red) and RMS (blue) of mass fractions for all major and minor species are shown. Solid lines: ODT, dotted lines: DNS. The black line represents the ODT results of the strained laminar flame with a strain rate of  $2\,400\text{ s}^{-1}$ .

The upper row in Fig. 7.13 shows results for  $C = 1, 3.5,$  and  $10,$  the middle row shows results for  $L_{max} = 3, 5,$  and  $7$  mm ( $L_{max}/D = 0.24, 0.39,$  and  $0.55$ ), and the bottom row shows results for setting the stagnation point location to  $\pm 1$  mm of the nominal case. These parameters are chosen to cover a relatively broad range of values and to show the sensitivity of results to changes in these values. First note, that for all values tested, results remain qualitatively similar indicating that simulation results are insensitive to moderate changes in parameter values. The temperature RMS plot shows that as  $C$  increases, the mixing layer broadens. A broadening of the mixing layer is similarly obtained by increasing the maximum size of eddies allowed from 3 to 7 mm. Although  $L_{max}$  increases by only a factor of 2.3 from 3 to 7 mm, it has a larger influence on the mixing width than increasing  $C$  from 1 to 10. The heat release rate statistics however show the reverse effect, whereby results vary only slightly with changes in  $L_{max}$ , but more prominently with changes in  $C$ . As  $C$  is increased, particularly at temperatures below 1200 K, the heat release rate decreases indicating higher levels of extinction. This is expected, as increasing  $C$  is representative of increasing the turbulence intensity at all length scales. If the turbulence intensity becomes too high, then within the residence time of the current counterflow configuration, a flame can not be sustained. Although, changes in  $L_{max}$  affect heat release rate results only slightly, it is seen that as  $L_{max}$  increases, the heat release rate rises. Larger eddies simultaneously mix in larger quantities of fresh gas and also increase the residence time of the gas by displacing burning fronts from the stagnation point towards the nozzles, giving the mixture more time to ignite. For the ODT counterflow simulations, the stagnation point location is an empirical input which is taken from the DNS. The sensitivity study shows that spatial and state-space statistics are not greatly affected by moderate changes in the stagnation point location.

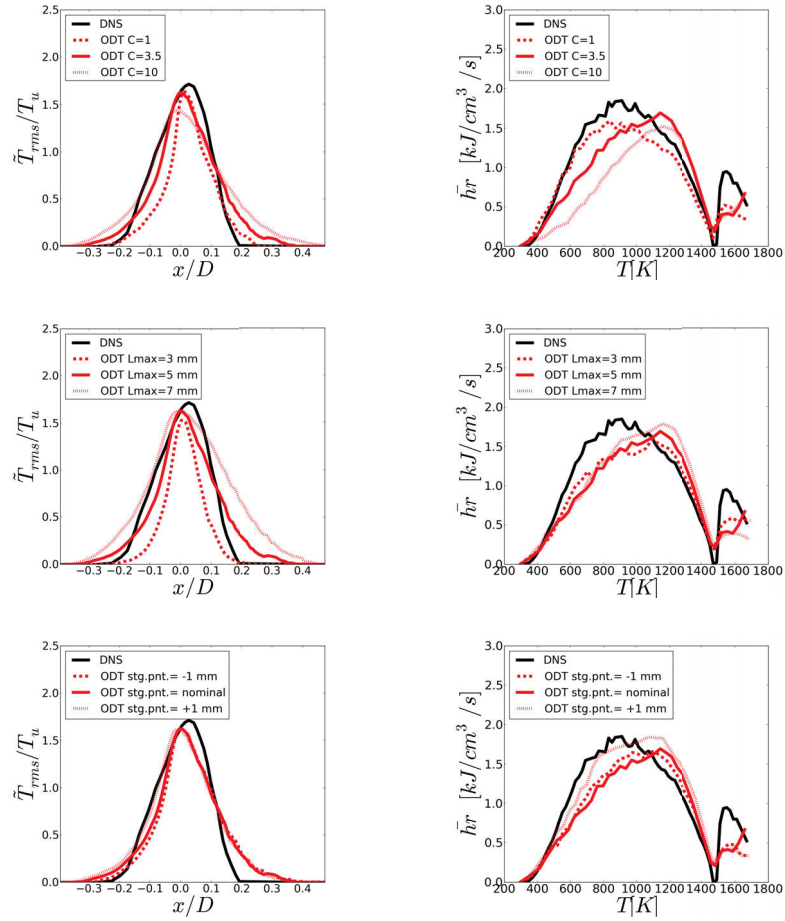


Figure 7.13: Sensitivity of the ODT results to the eddy frequency parameter  $C$  (top), maximum allowed eddy size  $L_{\max}$  (middle), and stagnation point location (bottom). The DNS data are also plotted for reference. Left: Favre RMS of temperature, normalized by the reactant inflow temperature  $T_u$  as a function of the axial distance normalized by the jet diameter. Right: mean heat release rate conditioned on temperature.

## CONCLUSIONS

---

In summary, the ODT methodology was applied to a turbulent reactant-to-product counterflow flame. Configuration specific models needed to address the 3D dilatation and advection phenomena on the 1D line were presented.

Comparison of results for the laminar strained flame obtained from ODT and OPPDIF, shows that the strain rate produced by ODT is slightly lower than that produced by OPPDIF. As a consequence, a very slight discrepancy is observed between ODT and OPPDIF profiles, whereby ODT profiles are more diffused.

Comparing ODT results with DNS data for spatial mean and fluctuating velocity, temperature, and major and minor species profiles, show that ODT results for temperature and species mean and RMS profiles are in good agreement with DNS. Comparison of the scalar dissipation rate shows that ODT estimates the mixing level seen in the DNS reasonably well. Flame extinction and ignition characteristics were compared by looking at the probability distribution of heat release rate conditioned on a progress variable. Comparisons show that the flame attenuation characteristics are captured accurately in ODT.

Scatter plots for heat release rate and major and minor species as a function of temperature were presented to illustrate model capabilities in capturing the full range of results observed by the DNS. Scatter plot results showed that temperatures above the hot product side inlet temperature and above the adiabatic flame temperature of the reactants are obtained. A test for superadiabaticity showed that superadiabatic conditions are however not reached. An additional study showed that differential diffusion effects are responsible for the higher temperatures reached in the turbulent flame.

State-space statistics of heat release rate and all species conditioned on temperature were shown for a more stringent comparison of ODT and DNS data. Good agreement with the DNS results is attained, although heat release rates for temperatures below 1 000 K are underpredicted.

A sensitivity study to ODT input parameters was carried out by varying the eddy frequency parameter  $C$ , the maximum eddy size allowed  $L_{max}$ , and the stagnation point location. For the range of parameters tested, results remained qualitatively consistent with moderate quantitative changes.

This work has demonstrated the application of ODT to the counterflow configuration. Results show that although ODT is a reduced order model, qualitative and quantitative agreement with DNS data are obtained.



## OUTLOOK

---

As introduced in Sec. 4, the counterflow configuration is one of the simplest configurations to study stratified turbulent flames. To provide an outlook for possible future research and to demonstrate the counterflow configuration's applicability to stratified flames in other canonical flow configurations, here an approach for using the ODT counterflow configuration to model the turbulent stratified premixed jet proposed by Sweeney et al. [108, 109] is outlined.

This section is organized as follows: in Sec. 9.1 the burner experimental setup is described, in Sec. 9.2 a modeling approach using the ODT counterflow configuration is proposed, and in Sec. 9.3 preliminary ODT state-space results are compared to experimental data for three different stratifications.

### 9.1 CAMBRIDGE STRATIFIED BURNER SETUP

In this section the Cambridge swirl burner (SwB) experimental setup presented in [108, 109] is described. A series of flames in a turbulent methane/air stratified flow were studied. The degree of stratification and swirl were varied to generate a matrix of experimental conditions. For the current comparisons with ODT, non-swirling cases are considered with varied degrees of stratification: SwB1 (premixed), SwB5 (moderately stratified), and SwB9 (highly stratified). The inner and outer annulus inlet equivalence ratios,  $\phi_i$  and  $\phi_o$  respectively, for the three different flames are given in Table 9.1, where  $S$  is included for completeness and is the swirl number calculated as the ratio of the inlet mean tangential velocity to axial velocity.

Fig. 9.1 depicts the burner setup. The burner features two annular channels through which fuel/oxidizer mixture can flow and a central bluff body to aid flame stabilization. The bulk velocity of the outer annulus  $U_o$  was set at more than twice the value of the velocity in the inner annulus  $U_i$  in order to generate substantial levels of shear between the two flows. Co-flow air was supplied around the outer annulus with a bulk velocity  $U_{co-flow}$  to prevent the entrainment of ambient air. The mean flame brush intersects the mixing layer at location  $z=50$  mm. Flow characterization measurements were taken at location C depicted in Fig. 9.1, as this was the closest measured data to the

Table 9.1: Operating conditions for Cambridge stratified burner.

Flame	$S$	$\phi_i$	$\phi_o$
SwB1	0	0.75	0.75
SwB5	0	1.0	0.5
SwB9	0	1.125	0.375

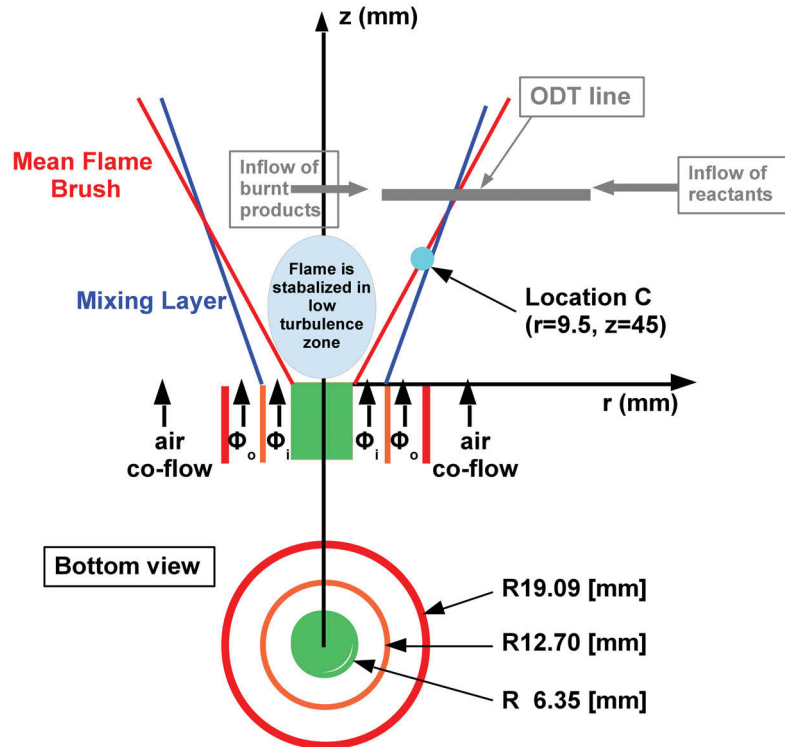


Figure 9.1: Cambridge burner setup [108]. At location C, experiment flow conditions are given in Table 9.2. At  $z=50$  mm the ODT line is shown in gray. At the left inlet of the ODT line a stream of hot burnt products are specified while at the right inlet of the ODT line a stream of cold reactants are specified.

location of the mean flame brush intersecting the mixing layer. Physical parameters of the burner and flow properties at location C are given in Table 9.2. For the calculation of the Damköhler and the Karlovitz number, a laminar flame at  $\phi=0.75$  was used for  $S_u^L$  and  $\delta_f$ . The values shown in Table 9.2 indicate that the flames lie in the thin reaction zone regime on the modified Borghi diagram, Fig. 2.2.

## 9.2 ODT MODELING APPROACH

As flow properties for the experimental setup are specified at  $z=45$  mm (Fig. 9.1 loc. C) and temperature conditioned results are provided on the radial line at  $z=50$  mm, the current goal is to match turbulence levels given at location C and to compare ODT state space results to experimental data on the radial line at  $z=50$  mm. The assumption is made that the turbulence intensity did not change significantly between flow measurements given at  $z=45$  mm and state space data given at  $z=50$  mm.

The ODT counterflow line is shown in Fig. 9.1, where at the left side inlet hot burnt products are supplied and at the right inlet cold premixed reactants. The hot products are needed to sustain and ignite the flame in case turbulence extinguishes it. By using the counterflow configuration, (1) a large scale strain and (2) a residence time for the flow is introduced. As the burning rate and



Table 9.2: Cambridge burner physical parameters

Bulk velocity co-flow ( $U_{\text{co-flow}}$ )	0.4 m/s
Bulk velocity outer annulus ( $U_o$ )	18.7 m/s
Bulk velocity inner annulus ( $U_i$ )	8.31 m/s
Inlet Temperature of reactants at $z=0$ mm ( $T_u$ )	294 K
At loc. C: mean velocity ( $\bar{u}$ )	12.62 m/s
At loc. C: RMS velocity ( $u'$ )	4.37 m/s
At loc. C: turbulent Reynolds number ( $Re_t$ )	463
At loc. C: integral length ( $l'$ )	1.72 mm
At loc. C: Kolmogorov length ( $\eta$ )	0.017 mm
At loc. C: Damköhler number ( $Da$ )	0.17
At loc. C: Karlovitz number ( $Ka$ )	1165

flame properties are controlled by strain, both of these effects need to be considered when choosing the inlet velocities and domain length. The boundary conditions that need to be specified on the product and reactant side are the inlet temperatures, mixture composition and velocities. Additionally, the ODT domain length also needs to be specified.

### 9.2.1 Inlet velocities and domain length

The chemical time scale  $\tau_c$  of a laminar methane/air flame at equivalence ratio  $\phi=0.75$  (the average equivalence ratio for each flame in Table 9.1) is  $\tau_c=2.28$  ms. Choosing the domain length to be  $L_x=12$  mm and setting the chemical time to be the desired residence time  $\tau_R$  of the counterflow, the reactant inlet velocity  $U_u$  is then found as  $U_u=0.5 \cdot L_x / \tau_R=2.6$  m/s. As the chemical time of a turbulent flame with back support is considerably shorter than that of the laminar flame,  $L_x$  was held fixed and  $U_u$  was iteratively increased until the desired turbulence level (measured by  $u'$  and  $l'$ ) was reached and reasonable comparisons to state space data was achieved. The product side inlet velocity  $U_b$  was set by requiring the stagnation point to be at the center of domain  $L_x/2$ . This requires that the momentum of the unburnt mixture balance that of the burnt products,  $\rho_u U_u^2 = \rho_b U_b^2$ . The ODT turbulence parameters, domain length and reactant inlet velocity are specified in Table 9.3.

### 9.2.2 Reactant and product inlet mixtures and temperatures

To provide the range of results seen in the experiment by the two inlet streams of different equivalence ratios, the reactant side of the ODT line can not have only one equivalence ratio. To illustrate this point, in Fig. 9.3 the scatter plot

Table 9.3: ODT parameters

Reactant inlet velocity ( $U_u$ )	10.0 m/s
Domain length ( $L_x$ )	12.0 mm
Inlet Temperature of reactants ( $T_u$ )	294 K
ODT eddy frequency parameter (C)	50
ODT eddy viscous penalty parameter (Z)	0.1
ODT maximum allowed eddy size ( $L_{max}$ )	6 mm
DL model time delay factor ( $\theta_{DL}$ )	0.1
Flow residence time ( $\tau_r = 0.5 \cdot L_x / U_u$ )	0.6 ms
Frequency of oscillation for $\phi_u$ ( $f_{ODT} = 1 / (2\tau_r)$ )	833.3 1/s

of mass fractions  $CH_4$  and  $O_2$  as a function of temperature is shown with the coloring of the points representing the equivalence ratio  $\phi$  given by

$$\phi = \frac{X_{CO_2} + 2X_{CH_4} + X_{CO} + 0.5(X_{H_2O} + X_{H_2})}{X_{CO_2} + X_{O_2} + 0.5(X_{CO} + X_{H_2O})}. \quad (9.1)$$

Additionally shown is the mean mass fraction over temperature in red. The results are for flame SwB9 (see Table 9.1) at location  $z=50$  mm. First looking at the experimental results for  $CH_4$  (Fig. 9.3 left, top) at temperatures close to  $T=300$  K. To be able to reproduce the high equivalence ratio results (indicated by orange) on the ODT line, requires that the cold reactant stream contain this rich mixture. Then, by mixing with burnt products, it might be possible to get dilution of the  $CH_4$  to get the lower mass fraction results which simultaneously give lower equivalence ratios (indicated by blue and cyan colors). However, looking at the same low temperature region for  $O_2$  (Fig. 9.3 left, bottom), it is clear that by specifying a rich equivalence inflow mixture, results of the  $O_2$  mass fraction are below the mean red curve and there is nothing in the reactant stream or the product stream to increase the  $O_2$  concentration to give the results above the mean red curve. Similar reasoning follows for other species as well, to indicate that if the ODT line has only one equivalence ratio on the reactant side, the result produced will only be a sub-set of the full range of results seen in the experiment.

The ODT reactant inlet equivalence ratio  $\phi_u$  is therefore a sine wave oscillating between the experiment flame  $\phi_i$  and  $\phi_o$  with frequency  $f_{ODT}$  and given by

$$\phi_u = \phi_o + \frac{\phi_i - \phi_o}{2} (\sin(f_{ODT} \cdot 2\pi t) + 1), \quad (9.2)$$

where  $t$  is the current time. This allows the ODT reactant stream to contain both fuel mixtures and turbulence to mix all states in between. The mixture and temperature of the burnt products then similarly changes with time and is specified as the products of complete combustion for the reactant equivalence ratio  $\phi_u$ .

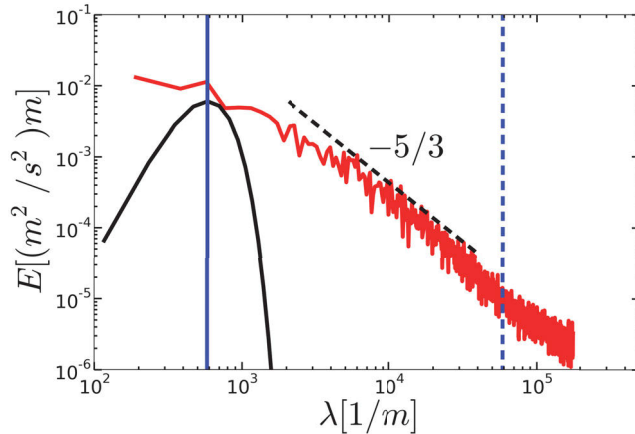


Figure 9.2: ODT energy spectrum (red) as a function of wave number. For reference, the Passot-Pouquet energy spectrum (black solid), the integral (blue solid) and Kolmogorov (blue dotted) length scales given in Table 9.2, as well as the  $-5/3^{\text{rds}}$  energy cascade (black dotted) are also plotted.

In this study the San Diego combustion mechanism proposed in [2] that contains 177 reactions and 38 species is used. A minimum grid cell size of  $10\ \mu\text{m}$  was used for the study.

### 9.3 RESULTS

In this section state-space results between ODT and experimental data are compared. To begin with, in Fig. 9.2 the energy spectrum produced on the ODT line at the location of maximum turbulence intensity is shown. Data was sampled at a rate  $6.0e^6\ \text{s}^{-1}$  for 4 ms and ensemble averaged over 10 realizations. In the figure, the integral length scale (blue solid) and the Kolmogorov length scale (blue dotted) are plotted for guidance, as well as the Passot-Pouquet energy spectrum indicating the magnitude of the energy contained in the integral length scale  $l'$  for given  $u'$  (see. Table 9.2). The figure shows that the ODT energy spectrum (red) accurately captures the desired turbulence level and a full spectrum reproducing to the  $-5/3^{\text{rds}}$  rule is produced.

Having confirmed that the desired turbulence level is reached, to show the range of results produced by ODT, in Fig. 9.3 and 9.4 a scatter plot of ODT state-space results is compared to experimental data for flame SwB9 taken from [108]. Following the procedure in [108], mean fits are generated by binning the species data in temperature space in steps of 20 K. From each temperature bin, 100 randomly selected points are then plotted with coloring of the markers representing the mixture equivalence ratio given by Eq. (9.2). The comparisons show that ODT is able to capture the range of results shown by the experimental data, although differences in details are observed. First, the maximum temperature in ODT is 2228 K which corresponds to the adiabatic flame temperature of a stoichiometric methane/air mixture. In the experimental data, the maximum temperature in the plots is approximately 2130 K. A possible explanation for the difference, is that in ODT burnt products at the

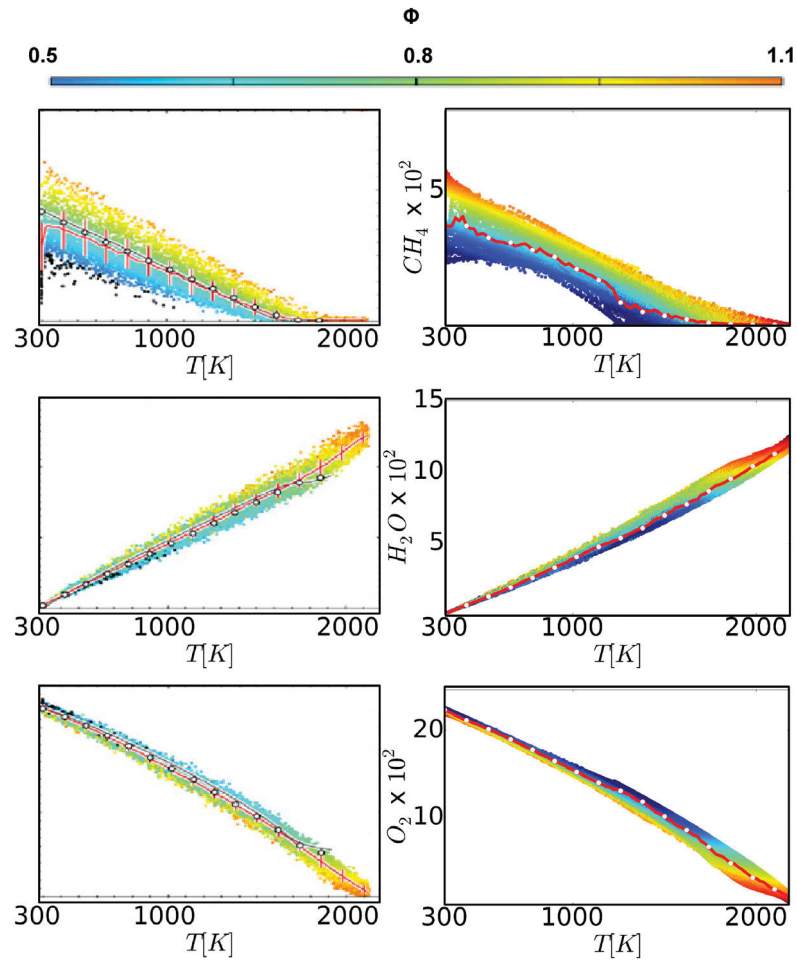


Figure 9.3: Scatter plot of mass fraction  $\text{CH}_4$  (top),  $\text{H}_2\text{O}$  (middle), and  $\text{O}_2$  (bottom) as a function of temperature for flame SwB9. ODT results (right). Experimental results (left) are taken from [108] at location  $z=50$  mm. Coloring of markers represent the equivalence ratio  $\phi$  given by the legend at the top. Mean mass fraction over temperature is plotted in red.

adiabatic flame temperature for the range of equivalence ratios of the flame are being specified as a boundary condition. This insures that within the domain all states are present, whereas for the experiment, through dilution of species and temperature, it is possible that these maximums are not seen. A second difference between ODT and experimental results is that the experiment exhibits higher  $\text{CO}$  and  $\text{H}_2$  maximums and lower  $\text{CO}_2$  values in Fig. 9.4. This might indicate that in the experiment there is a greater degree of incomplete burning as in ODT. One possible remedy might be to reduce the residence time of the flow in ODT.

In Fig. 9.5 mean mass fractions as a function of temperature for ODT and experimental data are compared for flame SwB1, SwB5 and SwB9. The general features and difference between the three different flames exhibited by the experimental data are reproduced by ODT. In these figures, the previously commented discrepancy between ODT and experimental data for  $\text{CO}$ ,  $\text{H}_2$  and  $\text{CO}_2$

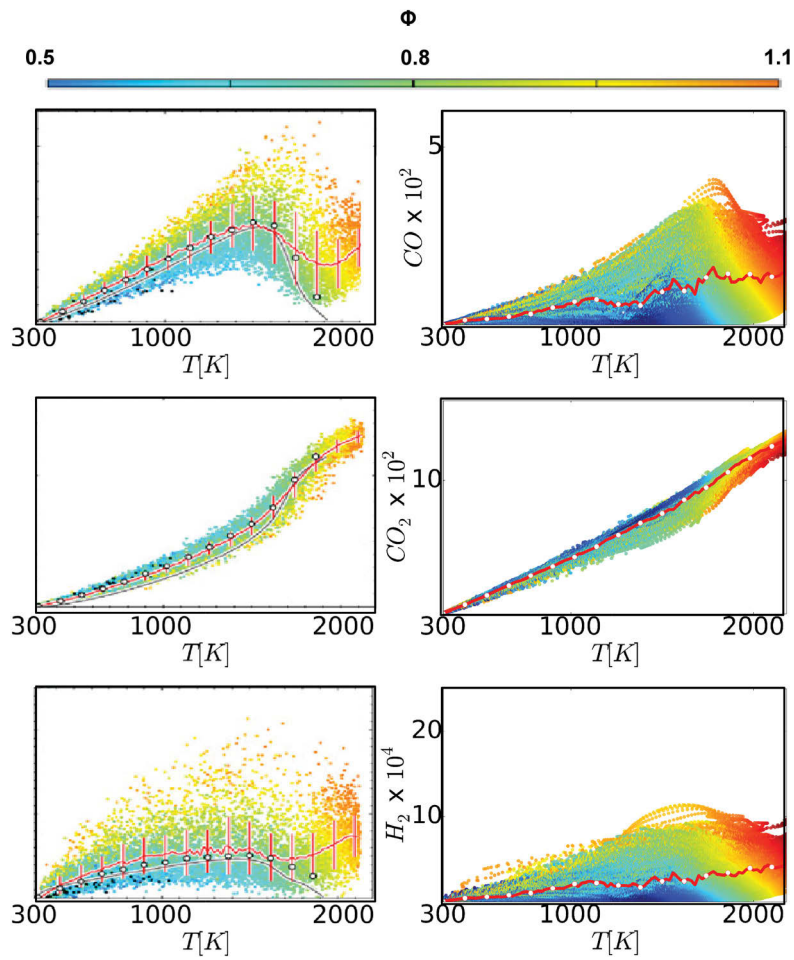


Figure 9.4: Scatter plot of mass fraction CO (top), CO<sub>2</sub> (middle), and H<sub>2</sub> (bottom) as a function of temperature for flame SwB9. ODT results (right). Experimental results (left) are taken from [108] at location  $z=50$  mm. Coloring of markers represent the equivalence ratio  $\phi$  given by the legend at the top. Mean mass fraction over temperature is plotted in red.

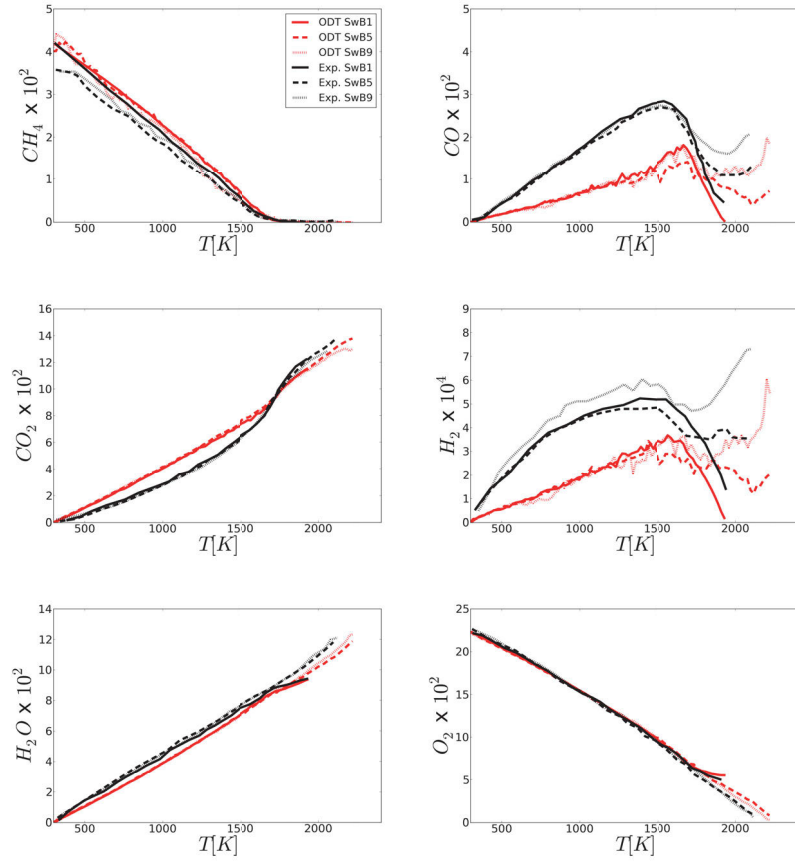


Figure 9.5: Mean mass fraction over temperature is plotted for ODT (red) and experimental data (black) taken from [108]. Flame SwB1 (solid), SwB5 (dashed) and SwB9 (dotted).

become more evident. Additionally, it is interesting to note that at  $T=300$  K, for flame SwB5 and SwB9 the experimental data for  $\text{CH}_4$  shows mass fraction that is lower than that for flame SwB1. ODT did not reproduce this tendency and it is not clear what reduces the mean  $\text{CH}_4$  concentration of flame SwB5 and SwB9 compared to SwB1 at the inflow temperature in the experiments.

#### 9.4 CONCLUSIONS

The modeling approach described is a first attempt to capture the gross features of the SwB non-swirling flames. Results have shown that ODT reproduces the general features, although adjustments in inlet mixture, flow residence time, frequency of sinusoidal oscillation between inlet equivalence ratios, and other ODT parameters are needed to be able to better reproduce the details of the experimental results.

## Part III

# COMPRESSIBLE ODT





*The contents of the Compressible ODT part have been extracted from Jozefik et al. [43]. Adaptations have been performed to enhance discussions where appropriate or to avoid repetition of theory or background information.*

Beginning with the Big Bang, the history of the Universe has been determined largely by explosions. The effects of explosions on humankind, both beneficial and detrimental, have been investigated from the beginning of science, resulting today in a degree of knowledge of their properties—their physics, chemistry and dynamics [82]. This knowledge is being used to help avoid unwanted explosions or to design explosions for specific purposes.

There are two different types of 1D steady reaction waves propagating through a reactive material: (1) detonations exhibit large pressure increases and small volume decreases, while (2) deflagrations have large volume increases and small pressure decreases. Detonations are found to be supersonic and deflagrations to be subsonic. Explosions are however dynamical processes that transition between the two and are defined as a scenario in which energy is injected into a system faster than it can be smoothly equilibrated [82].

Mechanisms for deflagration to detonation transition (DDT) remain a topic of open research. It has been however observed that DDT is reluctant to occur in open and obstacle-free systems, but in the presence of walls or in closed vessels the conditions for transition are favorable [63]. It has been further observed that a flame can experience a transition to detonation only through an unsteady process [63].

In a confined vessel with gaseous combustibles, a turbulent flame emits pressure waves that propagate compressing the fuel and raising its temperature resulting in a strong decrease in the fuel's reaction time. The temperature increase can be great enough to generate local explosions that develop into new deflagration waves. Eventually, large enough pressure waves develop to trigger a detonation that then propagates through the rest of the combustible mixture. This mechanism of DDT is described by Zel'dovich et al. [125] and termed the Zel'dovich gradient mechanism. Hot spots can give rise to detonations by the ignition of a detonation in a gradient of reactivity. The idea being is that a spontaneous reaction wave can propagate through a reactive material if there is a spatial gradient in chemical induction time  $\tau_c$ . The wave appears when the material spontaneously ignites at the location of the minimum  $\tau_c$ . The resulting wave propagates in the direction of the gradient with the velocity  $D_{sp} = |\nabla\tau_c|^{-1}$ .

Shock tube experiments of a combustible gases fuel have been widely used for the study of DDT. The passage of a shock over a flame distorts the flame, making it turbulent and increasing the energy-release rate of the system. Mark-

stein [74] showed that the first and major effect of the interaction of a curved flame and a shock is a large funnel of unburned material that extends into the burned region. The funnel forms as a result of the Richtmyer-Meshkov (RM) instability [79, 97], which develops as a shock impulsively accelerates a perturbed contact discontinuity.

The goal here is to extend the adaptive ODT methodology introduced by Lignell et al. [66] and used in the counterflow configuration in part II of this thesis to handle compressibility effects and their interactions with turbulence and chemistry and to study shock-turbulence interaction (STI) and DDT. The STI, which is related to the RM instability, plays a fundamental role in the context of many physical settings, both natural and man-made. To list a few, it finds applications in natural phenomena like supernova collapse [106], pressure wave interaction with flame fronts [74], and supersonic and hypersonic combustion [73, 116]. In the interaction of shock waves with flames it plays an important role in the DDT [51, 52, 53], and in inertial confinement fusion [68].

This part is organized as follows. Section 11 gives an overview of the modeling approach. Section 12.1 discusses the strategy of incorporating instabilities caused by acceleration of a variable density flow into ODT. Section 12.1.1 presents the model representation of the Darrieus-Landau instability caused by unsteady dilatational flow and section 12.1.2 introduces the ODT representation of shock-turbulence interaction. Section 13 presents results for (1) Sod's shock tube problem with comparison to a Riemann solver, (2) non-reacting shock-tube results with comparison to experimental and LES data, and (3) reacting shock-tube results with comparison to 2D simulation data. The details of the numerical implementation and the shock-turbulence interaction model are provided in Appendix E and F respectively.

### 11.1 OVERVIEW

In this section a general overview of the modeling approach is given. To the author's knowledge, the current state of the art for modeling compressible turbulence in 1D is by Ni et al. [81]. In their formulation, the flow is entirely confined to a 1D line and turbulent fluctuations are generated by stochastic forcing. The intention is to improve on this formulation by introducing a physically based turbulence model, namely ODT, that is also capable of mixing scalars which is ideal for combustion. Therefore, the formulation has a hydrodynamic model that is based on the truncated 1D Navier-Stokes equations and a turbulence model that emulates 3D turbulence.

The physics of the turbulence model are described in detail in Sec. 3.2.2 and have been validated generally in many ways. A submodel of ODT, intended to represent unsteady dilatation, termed the Darrieus-Landau (DL) instability, is described in Sec. 5.3.3 and has been validated in a turbulent counterflow configuration Sec. 7 and a turbulent wall flame fire [80]. For flows involving shocks, in Sec. 12.1.2 a model for representing shock-turbulence interaction (STI) is introduced, which is based on the validated concept of the DL instability model. To validate the STI model, in Sec. 13.2 ODT results with experimental data are compared for a non-reactive shock tube with reshock. As this is a non-reactive case, dilatational effects are minimal in comparison to the instability generated by a shock traveling over a density interface and therefore is an ideal test case for the STI model.

The formulation for the hydrodynamic model and its implementation is described in Appendix E. It is an extension of the code described in Sec. 5.1 to include finite Mach number effects. In Sec. 13.1 the hydrodynamic model is compared to a 1D gas dynamics solver for Sod's shock tube problem. This and the laminar simulations carried out for the non-reactive and reactive shock tubes in Sec. 13.2 and 13.3 respectively are verifications of the 1D hydrodynamic solver, as in these cases the turbulence model is turned off.

In general, the ODT methodology views the 1D line as a closed system. In the example of the counterflow configuration Sec. 6, the 1D line is taken to be the center line connecting two nozzles facing each other. For such a configuration, mass conservation dictates a mean off-line flow. In Sec. 5.3.1 the necessary additional modeling needed to take into account off-line flow was developed. For the applications discussed here, although expansion and compression can occur in off-line directions, they are statistically 1D flows and off-line effects are neglected to maintain simplicity in the formulation. Results shown in Sec. 13 validate the hypothesis that a treatment of off-line effects is not needed.

## 11.2 GOVERNING EQUATIONS

The time advancement of the truncated 1D equations are interrupted to implement eddy events EE as discussed in Sec. 3.2. Further explanation of the formulation and numerical solution of the governing equations is provided in Appendix E. The truncated differential equations for continuity, momentum, species and enthalpy are written as:

$$\frac{\partial \rho}{\partial t} + \frac{\partial (\rho u_1)}{\partial x} + EE(\rho) = 0, \quad (11.1)$$

$$\frac{\partial u_i}{\partial t} + u_1 \frac{\partial u_i}{\partial x} + EE(u_i) = \frac{1}{\rho} \left( -\frac{\partial p}{\partial x} \delta_{i1} + \frac{\partial \sigma_{i1}}{\partial x} \right), \quad (11.2)$$

$$\frac{\partial Y_s}{\partial t} + u_1 \frac{\partial Y_s}{\partial x} + EE(Y_s) = \frac{1}{\rho} \left( -\frac{\partial j_s}{\partial x} + \dot{\omega}_s \right), \quad (11.3)$$

$$\frac{\partial h}{\partial t} + u_1 \frac{\partial h}{\partial x} + EE(h) = \frac{1}{\rho} \left( \frac{\partial p}{\partial t} + u_1 \frac{\partial p}{\partial x} - \frac{\partial q}{\partial x} + \sigma_{i1} \frac{\partial u_i}{\partial x} \right), \quad (11.4)$$

with  $s = 1, \dots, n_s$  and  $n_s$  is the number of different species in the gas mixture. Subscripts  $i \in \{1, 2, 3\}$  denote the  $\{x, y, z\}$  spatial directions where  $x$  is the spatial direction along the ODT line and summation over repeated indices  $i$  is implied.  $u_i$  denotes the three ODT velocity components,  $\rho$  is the density,  $Y_s$  is the mass fraction of species  $s$ ,  $\dot{\omega}_s$  is the chemical source term of species  $s$ ,  $h$  is the enthalpy of the mixture, and  $p$  is the pressure. The species diffusive flux  $j_s$  is given by

$$j_s = -\rho D_s \left( \frac{\partial Y_s}{\partial x} + \frac{Y_s}{\bar{M}} \frac{\partial \bar{M}}{\partial x} \right), \quad (11.5)$$

where  $D_s$  is the diffusion coefficient of species  $s$  and  $\bar{M}$  is the mean molecular weight. The heat flux  $q$  is given by

$$q = -\lambda \frac{\partial T}{\partial x} + \sum_{s=1}^{n_s} h_s j_s, \quad (11.6)$$

where  $h_s$  is the enthalpy of species  $s$  including the heats of formation,  $\lambda$  is the thermal conductivity and  $T$  is the temperature.  $\sigma_{ij}$  is the deviatoric stress tensor given by

$$\sigma_{ij} = 2\mu e_{ij} - \frac{2}{3}\mu \frac{\partial u_k}{\partial x_k} \delta_{ij}, \quad (11.7)$$

where  $\mu$  is the dynamic viscosity of the mixture,  $e_{ij} = \frac{1}{2} \left( \frac{\partial u_i}{\partial x_j} + \frac{\partial u_j}{\partial x_i} \right)$  is the strain rate tensor and  $\delta_{ij}$  is the Kronecker-Delta function. Summation over repeated indices  $k$  is implied. ODT has one spatial direction but all three velocity components are time advanced. The deviatoric stress tensor therefore has the following three components:

$$\sigma_{11} = \frac{4}{3}\mu \frac{\partial u_1}{\partial x}, \quad \sigma_{21} = \mu \frac{\partial u_2}{\partial x}, \quad \sigma_{31} = \mu \frac{\partial u_3}{\partial x}. \quad (11.8)$$

All other components of the deviatoric stress are eliminated as part of the 1D modeling approach. The equation of state of a mixture of ideal gases is given by

$$p = \rho T \frac{R}{M}, \quad (11.9)$$

with  $R$  denoting the universal gas constant.

Owing to the 1D truncation, advection in these equations acts only in the  $x$  direction, yet all three velocity components are time advanced. This and other differences between the treatment of  $u_1$  and the other velocity components are explained in Sec. 12.1.2.

### 11.3 CHEMICAL SOURCE TERMS

For the reactive case, comparisons to the 2D fully resolved simulation results from [Khokhlov et al. \[51, 53\]](#) are made. The simulations use a one-step Arrhenius expression for the chemical source term that was developed for modeling a stoichiometric acetylene-air mixture. The simplified chemistry model gives the correct 1D flame and detonation properties over the range of temperatures and pressures typical of experiments. To minimize sources that could potentially cause differences between ODT and the 2D simulation results, this one-step mechanism and the associated material properties are adopted. The source term is therefore described by the first-order Arrhenius kinetics as

$$\frac{dY}{dt} \equiv \dot{\omega} = -A\rho Y \exp\left(-\frac{Q}{T}\right), \quad (11.10)$$

where  $A = 1 \times 10^9 \text{ m}^3/\text{kg/s}$  is the preexponential factor,  $Q = 29.3T_0$  is the activation energy, and  $T_0 = 293 \text{ K}$  is the initial temperature. The enthalpy of formation used for this chemical model is  $h_f = 35.0RT_0/M$ . The temperature dependence for the kinematic viscosity, species diffusion, and heat conduction are

$$\nu = \nu_0 \frac{T^n}{\rho}, \quad D = D_0 \frac{T^n}{\rho}, \quad \frac{K}{\rho c_p} = \kappa_0 \frac{T^n}{\rho}, \quad (11.11)$$

where  $\nu_0 = D_0 = \kappa_0 = 1.3 \times 10^{-6} \text{ kg/m s K}^n$  are the transport constants,  $c_p = \gamma R/M(\gamma - 1)$ ,  $\gamma = 1.25$ ,  $M = 29$  is the molecular weight, and  $n = 0.7$ .

A more extensive description of the physical and chemical model is given in [52].

#### 11.4 MESH ADAPTION

An adaptive mesh approach is used, such that the merging and splitting of grid cells is performed in a manner that conserves transported quantities: mass, momentum, and energy. The grid is adapted based on a nominally uniform distribution of grid points along the arc length of the (centered and scaled) velocity, heat release rate, and species profiles [66]. For the non-reactive and reactive simulations a minimum grid cell size of  $50\ \mu\text{m}$  and  $5\ \mu\text{m}$  are used respectively, which are sufficiently small that no significant differences in results are observed when halving the minimum grid cell size. The minimum cell size allowed is set prior to the simulation and controlled during time advancement. If the minimum cell size criterion is violated, then mesh adaption is performed and cells are merged conserving mass, momentum, etc. The occurrences of merging operation dissipates kinetic energy and scalar fluctuations to some extent. For this reason, mesh adaption is formulated to be applied only when/where it is needed so that merging are not frequent enough to degrade computed results significantly. A more detailed discussion of the adaption procedure is provided in [66].

In ODT, the turbulent motions that accelerate mixing are modeled through a series of stochastic rearrangement events. These events may be interpreted as the model analog of individual turbulent eddies which are referred to as ‘eddy events’ or simply ‘eddy’. Each eddy event interrupts the time advancement of other processes and an instantaneous transformation is applied to the property profiles over some spatial interval  $(x_0, x_0 + l)$ . The eddy event is described in detail in Sec. 3.2.2.

### 12.1 REFERENCE-FRAME ACCELERATION IN ODT

The strategy of incorporating instabilities into ODT resulting from flow acceleration effects is discussed in detail in Appendix D. Here, the underlying concept is recapitulated to provide a framework for introducing a model for shock-eddy interaction.

Consider a fluid parcel that is accelerated by some mechanism. Viewed in the accelerating reference frame, the fluid is subject to a d’Alembert force that is formally the negative of the gravitation force in the context of the Rayleigh-Taylor (RT) instability [54]. Accordingly, the response of the fluid parcel to acceleration can be analyzed by supposing instead that it is subject to the corresponding gravitational field. If there is density variation within the fluid parcel in the direction aligned with gravity, then density increase in the direction opposite to the orientation of the gravity vector implies gravitational instability. In this context, ODT provides a dynamical pathway to represent the instability. The likelihood of a prospective eddy event is based on ‘available energy’. Upon identifying the accelerating mechanism of a variable density flow, an ‘available energy’ term can be calculated and used to increase or decrease the likelihood of generating turbulence (accepting eddies). For the case of the RT instability, the accelerating mechanism is the constant gravity. For the Darrieus-Landau (DL) instability, the accelerating mechanism is the time varying thermal expansion across a burning front. For the Richtmyer-Meshkov (RM) instability, the acceleration of the fluid is caused by the passing of a shock. In the ODT context, the reactive RT turbulence generated by overlying heavy/cold reactants and underlying light/hot products was studied in [35]. The DL model was first introduced in [44] and used for the simulation of ignition times in a turbulent homogeneous-charged compression-ignition. In [80] it was used to improve the modeling of a turbulent wall fire and in Sec. 7 it was used in modeling a turbulent counterflow flame. In what follows, the DL model is briefly described and the shock-turbulence-interaction (STI) model is introduced.

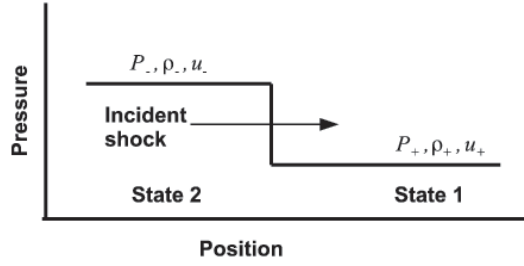


Figure 12.1: Incident shock propagating to the right. State 1 and 2 are chosen to be downstream and upstream of the propagating shock respectively. Due to the notional discontinuity across the shock, states 1 and 2 can be taken to be arbitrarily close to each other.

### 12.1.1 Darrieus-Landau-instability model

Planar flames are intrinsically unstable due to acceleration of the variable-density fluid caused by thermal expansion across the burning front. This is the DL instability and has been introduced in Sec. 5.3.3.

Here, a new feature is added to the DL model to reflect the physical initiation of turbulence by the DL instability while hindering potential runaway characteristics of the DL model that do not conform to the true physical behavior [15]. To this effect, a delay time between an accepted DL energy dominated eddy and potentially accepting another DL energy dominated eddy over the accepted eddy interval is introduced. The delay time is defined by the eddy time scale  $\tau$  times an adjustable coefficient  $\theta_{DL}$ . That is, consider an accepted eddy at time and location  $t_1$  and  $x_1$  respectively with time and length scale  $\tau_1$  and  $l_1$  respectively for which  $E_{pe}^{DL}$  was the dominant source of energy. Then, the next  $E_{pe}^{DL}$  dominated eddy overlapping the line segment  $[x_1, x_1 + l_1]$  can be accepted only for current time  $t$  greater than  $t_1 + \tau_1 \cdot \theta_{DL}$ .

### 12.1.2 Shock-turbulence-interaction model

The STI model is now introduced from a conceptual point of view. A formal derivation of the model is provided in Appendix F. Consider a homogeneous mixture of gas (state 1) in which a shock at Mach-number  $Ma$  moves to the right. As the shock propagates it raises the pressure and density upstream of the shock (state 2) and induces a uniform subsonic flow. This is schematically depicted in Fig. 12.1. The thickness of the shock is of the order of the mean free path, so that properties vary almost discontinuously across a shock wave and states 1 and 2 can be taken to be arbitrarily close to each other.

The RM instability arises when a shock passes over a perturbed interface separating two different fluids. The basic mechanism for the amplification of perturbations at the interface is baroclinic vorticity generation resulting from the misalignment of the pressure gradient of the shock and the local density gradient across the interface. As the interface between the two fluids becomes more distorted, secondary instabilities, such as the Kelvin-Helmholtz shearing instability, also become important, causing the roll up (mushrooming) of the



spike and the appearance of smaller scales. Eventually a turbulent mixing zone (TMZ) develops between the two fluids [11]. In the case of heavy fluid accelerating into light (H/L), spikes appear, and for the case of light fluid accelerating into heavy (L/H), bubbles appear at the interfaces [79] (see Appendix B for a more detailed description of the physics).

On a 1D line, the individual steps that lead to a TMZ cannot be captured. Therefore, the model employed is also not termed an RM model. The passing of a shock over a variable density flow is instead viewed as an energy source that acts for a period of time. The STI contribution to the ODT rate expression is modeled by modifying the expression for the DL contribution, Eq. (5.14), and is written as

$$E_{pe}^{STI} = C_s \left| \alpha_{STI} \int_{x_0}^{x_0+l} K(x) \cdot (\rho(f(x)) - \bar{\rho}) dx \right|, \quad (12.1)$$

where  $\alpha_{STI}$  is an acceleration term that is defined as

$$\alpha_{STI} \equiv \frac{Ma \cdot c \cdot \Delta u}{l}. \quad (12.2)$$

The speed of sound  $c = \sqrt{\gamma_+ P_+ / \rho_+}$  and the shock Mach number are calculated in the gas downstream of the shock, and  $\Delta u = u_- - u_+$  is the change in gas velocity across the shock. Additionally, because there is no quantitative basis for treating the shock as an energy source, a tunable coefficient,  $C_s$  is introduced in Eq. (12.1). For cases with reshock, the re-shock creates a second much more energetic RM instability than the initial shock [39]. To reflect this behavior, the reshock is assigned a different constant,  $C_{rs}$ . Contrary to the DL model that acts to enhance turbulence in regions of L/H and mitigate turbulence for H/L interfaces (hence the analogy to RT instability), the STI model is formulated to enhance turbulence for both H/L and L/H interfaces as indicated by the absolute value brackets in Eq. (12.1). Conceptually, the acceleration term can be seen as some measure of the shock strength over a particular eddy interval and the integral term can be seen as a measure of the density stratification of the flow over an eddy analogous to the Atwood number,  $At = (\rho_- - \rho_+) / (\rho_- + \rho_+)$ . As in Eq. (5.14), the formulation of the integral is based on the physical consideration that shocks directly generate turbulence only when they encounter density variations. The time duration  $t_e$  over which a shock is deemed to be a source of available energy for a particular eddy is defined by multiplying the eddy time scale  $\tau$  by an adjustable coefficient  $\theta_{STI}$  to obtain  $t_e = \tau \cdot \theta_{STI}$ . Hence, a shock that passed the sampled eddy location within the time range  $[t - t_e, t]$ , where  $t$  is the current time at which an eddy is sampled, is deemed to interact with the eddy. Although the aforementioned describes eddy interaction with a single shock or reshock event, the same concept applies if multiple shocks and reshocks are present within the assumed time window.

An additional departure from the implementation of the DL model is that, contrary to the DL model, the STI model is seen as an external energy source

and therefore does not only affect the probability of acceptance of an eddy, but also changes the total kinetic energy during the energy redistribution step of the eddy event. However, in compressible flow,  $u_1$  is advecting, which implies compressions and expansions due to nonzero  $\partial u_1 / \partial x$ . Then if the  $u_1$  component were included in the kernel mechanism, there would be a direct kinematical effect of the STI model as well as the indirect kinematical effect of its contribution to the available energy. For the sake of a minimal representation of the STI, the choice is made to exclude the direct effect. So during an eddy, the  $u_1$  component is subject only to triplet-mapping. In this formulation the available energy is then based solely on the  $u_2$  and  $u_3$  components.

STI is implemented based on shocks previously but not presently within the range of a candidate eddy (justified in Appendix F). Therefore, incorporation of this interaction into the eddy implementation as described in the previous paragraph, including triplet-map implementation, causes no artifacts. Incorporation of shock-eddy interactions then simply involves inclusion of Eq. (12.1) in the rate expression in the same manner that Eq. (5.14) is included. In particular, both can be included for a given eddy with no inconsistency because they represent two distinct, additive reference-frame effects.

### 12.1.3 ODT adjustable parameters

ODT has four adjustable parameters, maximum and minimum eddy size allowed, eddy frequency parameter  $C$  and viscous penalty parameter  $Z$ , that need to be specified. The maximum and minimum eddy size allowed are set large and small enough respectively such that simulation results are not constrained by these two parameters. Additionally to the ODT parameters, one DL model constant and three STI model constants need to be specified. The choices for ODT parameters  $C$  and  $Z$  and the DL and STI model parameters are shown in table 12.1. These parameters were chosen by matching ODT results for turbulent kinetic energy to LES results and turbulent mixing width growth rates to experiments. Corresponding ODT results are shown in Sec. 13.2.

Table 12.1: ODT adjustable parameters.

ODT viscous penalty parameter	$Z = 100$
ODT eddy frequency parameter	$C = 2$
DL model time delay factor	$\theta_{DL} = 1$
STI model shock energy scaling factor	$C_s = 2 \times 10^{-4}$
STI model reshock energy scaling factor	$C_{rs} = 5 \times 10^{-2}$
STI model elapsed time factor	$\theta_{STI} = 1$

## RESULTS

The results section is outlined as follows: in Sec. 13.1 the compressible solver is validated by making comparisons to a Riemann solver for Sod's shock tube problem. In Sec. 13.2 the STI model is validated for a series of non-reactive shock tube experiments, and finally in Sec. 13.3 ODT model predictions are compared to 2D simulation results for a reactive shock tube at different Mach numbers.

## 13.1 SOD'S SHOCK TUBE PROBLEM

A useful problem to test a compressible flow code is the shock tube, in which a long straight cylinder is divided into two compartments by a central diaphragm. In these simulations the turbulence model is turned off and the intention is to verify the hydrodynamic solver. At time  $t=0$  a diaphragm at the location  $x=0.5$  m separates the two constant states. On the left side of the diaphragm the initial conditions are  $p=100$  kPa and  $\rho=1.230$  kg/m<sup>3</sup>. On the right side of the diaphragm two cases are calculated. For case 1,  $p=10$  kPa and  $\rho=0.1230$  kg/m<sup>3</sup> and for case 2,  $p=1$  kPa and  $\rho=0.01230$  kg/m<sup>3</sup>. The initial temperature in the domain is  $T=300$  K. The gas is an ideal gas with  $\gamma=1.4$  and molecular weight  $M=28.0115$  kg/kmol.

The calculation begins by removing the diaphragm with the gases at rest. The pressure difference in the two gases drives a shock into the less dense gas, while a rarefaction moves into the denser gas. Across the contact discontinuity the pressure and velocity are continuous, but the density has a jump for all time. In Fig. 13.1 the pressure, density and velocity profiles are compared with the solution from a Riemann solver at time  $t=0.4$  ms for both case 1 and 2. The comparison shows that the methodology is stable and that shock speed is captured accurately. The shock wave and the contact discontinuity are computed with no smearing. Case 2 demonstrates that even for a large pressure discontinuity, a factor of 100 between the initial pressure on the left and right side of the diaphragm, the expansion wave and the shock are captured without smearing, overshoots or numerical oscillations.

In order to demonstrate the ability of the scheme to compute complicated wave interactions accurately, the shock tube problem is carried a step further. Reflecting walls are assumed at  $x=0$  and  $x=1$  m. The computation is continued to see how the reflection of the shock from the wall and its collisions with the contact discontinuity are calculated. In Fig. 13.2 the solution at  $t=2.6$  ms is shown after the first reflections of the shock wave from the wall and collision with the contact discontinuity.

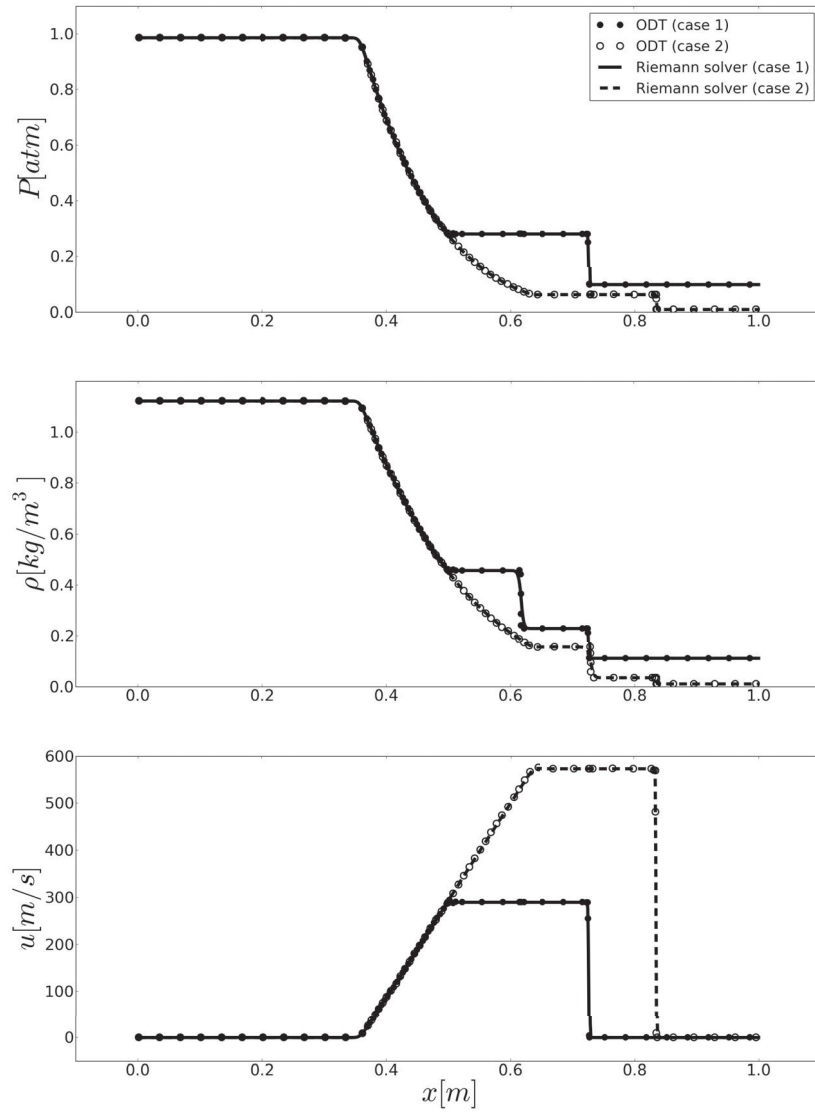


Figure 13.1: Comparison of the hydrodynamic solver (Appendix E) to a Riemann solver for Sod's shock tube problem at 0.4 ms. Results for pressure (top), density (middle), and velocity (bottom) for an initial pressure jump across the central diaphragm of a factor 10 (case 1) and 100 (case 2) are shown.

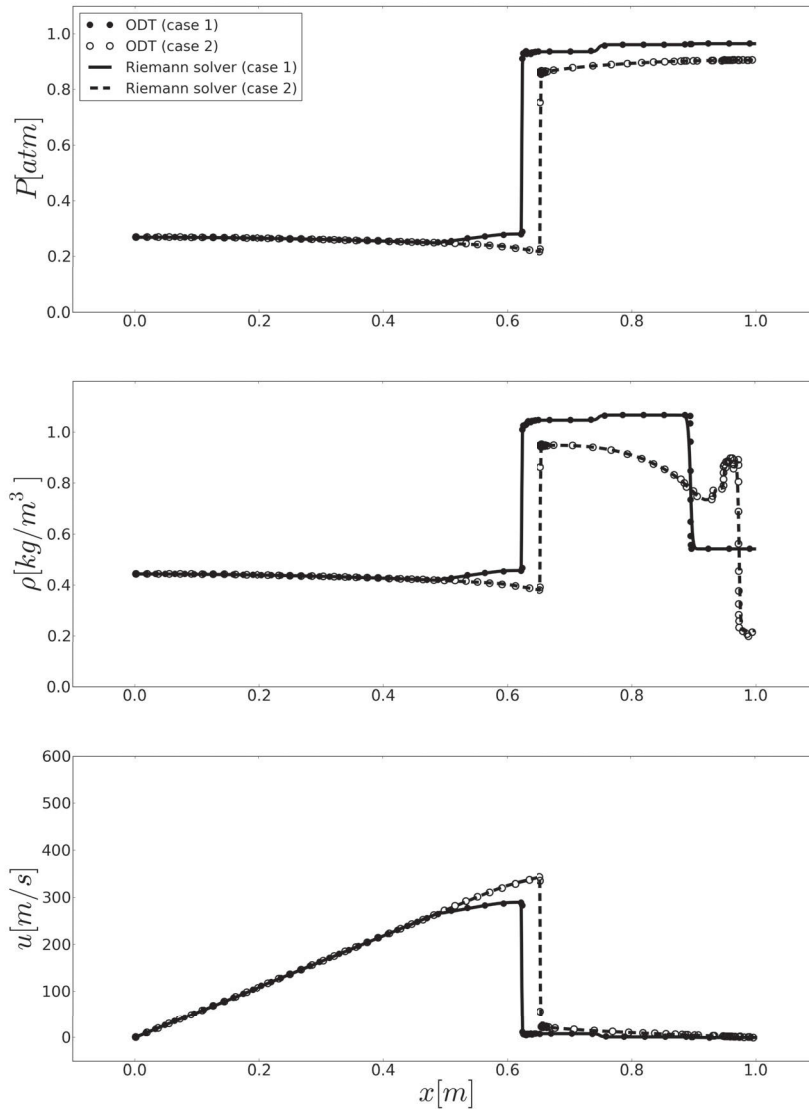


Figure 13.2: Comparison of the hydrodynamic solver (Appendix E) to a Riemann solver for Sod's shock tube problem at 2.6 ms. Results for pressure (top), density (middle), and velocity (bottom) for an initial pressure jump across the central diaphragm of a factor 10 (case 1) and 100 (case 2) are shown.

## 13.2 NON-REACTIVE RM INSTABILITY WITH RESHOCK

Next, a non-reactive example of the RM instability with reshock is presented. The experiments of Vetter and Sturtevant (VS) [113] involved a planar incident shock with  $Ma$  ranging from 1.18 to 1.98 striking a density interface formed by a thin membrane separating two gases, air and sulfur hexafluoride ( $SF_6$ ). The passage of the transmitted shock induced a turbulent mixing zone (TMZ) between the air and  $SF_6$  which was instantaneously accelerated to reported velocities of 56 m/s to 287 m/s, depending on the case. The length of the shock tube from the interface to the end wall was set prior to each experiment to ensure that the reshocked TMZ would develop in the observation field. Pictures were collected as the TMZ passed the observation field, and data were again recorded after the transmitted shock reflected off the closed end of the shock tube and reshocked the TMZ. The instantaneous width of the TMZ was measured and two TMZ growth rates were calculated, one following the initial shock and the second following the reshock. The results for TMZ width versus time serve as the primary comparison between the experiments and the ODT simulations. To obtain a more detailed understanding of the ODT STI model capabilities and limits, LES results from Hill et al. [39] for the  $Ma=1.50$  case are presented for the TMZ and the turbulent kinetic energy (TKE) as a function of time. In the experiments, measurements were taken from photographs of the TMZ, but the way in which these measurements of the width were made was not reported. For this reason, the definition of the TMZ width  $\delta$  used in the LES is adopted and written for 1D as

$$\delta(t) = 4 \int_0^L (1 - Y_{SF_6}) \cdot Y_{SF_6} dx. \quad (13.1)$$

Because ODT is a stochastic simulation, results have been ensemble averaged over 300 realizations. It is additionally noted that the VS experiments use a shock tube with a large cross-sectional area compared to other experiments to reduce the influence of boundary layer effects [113] and therefore make for an ideal comparison case for ODT.

A schematic of the initial flow configuration, including the incident shock, the interface between the two test gases, and boundary conditions is shown in Fig. 13.3. The simulated shock Mach numbers and the corresponding initial test conditions are shown in table 13.1. The four Mach numbers were chosen to provide a wide range of comparisons and because high-speed motion pictures are available for these four cases, opposed to less accurate single spark-schlieren photographs for other VS  $Ma$  cases.

First, results for the  $Ma=1.50$  case are presented. The laminar wave diagram for the configuration is shown in Fig. 13.4. The transmitted shock hits the far wall at approximately 2.5 ms and reshocks the density interface at approximately 3.5 ms. This sets up an expansion wave that hits the wall at 4.5 ms, and then the interface is hit with this expansion wave around 5.5 ms. The comparison between ODT and VS results serve as a validation of our 1D hydrodynamic model for planar-symmetric 3D laminar cases.

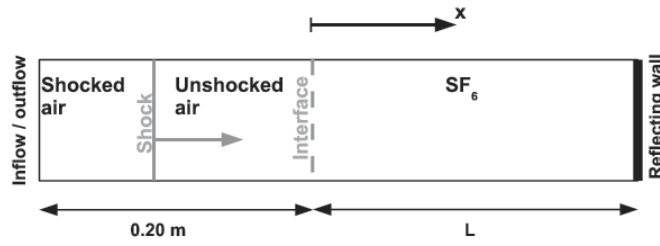


Figure 13.3: Geometry of the ODT 1D simulation domain.

Table 13.1: Simulated Mach numbers and their corresponding test conditions.

Shock Mach number (Ma)	1.24	1.43	1.50	1.98	[-]
Length, interface to end wall (L)	1.10	0.62	0.62	0.49	[m]
Initial pressure	40	31	23	8	[kPa]
Initial temperature	286	286	286	286	[K]

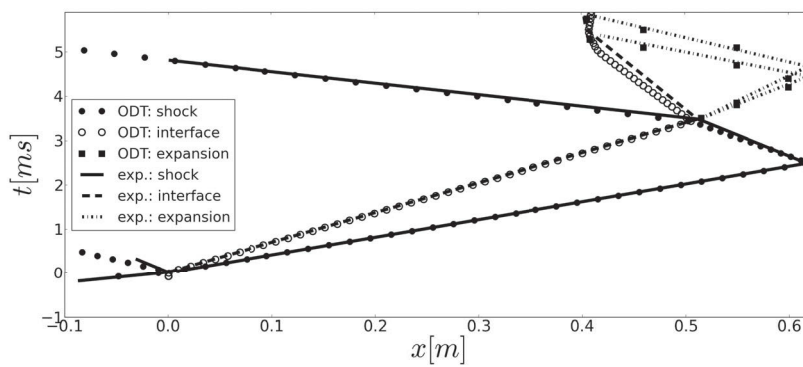


Figure 13.4: Wave diagram for the interaction of a Ma=1.50 shock wave with a plane discontinuous interface between air and SF<sub>6</sub>.

Computed TMZ width as a function of time for ODT, VS and LES are shown in Fig. 13.5 (left). First, comments on the LES results are given to provide a basis for later comparing ODT to LES. In comparing the LES to VS experimental data, it is seen that LES overestimates the initial growth. In the LES, the initial perturbations were much larger than those inferred for the experiments, therefore no actual agreement in the mixing-zone width was anticipated in the early stages of the simulation [39]. The agreement for the TMZ growth width rates  $d\delta/dt$ , post shock and post reshock are quite reasonable. The arrival of the reshock is indicated by the sharp compression of the TMZ. The evolution of the mixing width after reshock can then be divided into distinct parts: (1) the initial growth from the reshock which starts to decay around 4.5 ms, (2) further growth stimulated by the reflected expansion event and peaking at 6 ms, followed finally by (3) turbulent saturation and a subsequent very slow period of growth [39]. These stages in the life of the post-reshock TMZ can be seen clearly in the LES TKE of the flow, Fig. 13.5 (right). The initial shock produces little TKE, visible as a small bump close to the time origin. The reshock arrives at 3.5 ms, followed by a steep decay in energy and then an increase as the expansion wave arrives. This peaks at 6 ms and is followed by rapid energy decay.

For ODT, in Fig. 13.5 (left), the growth of the TMZ after the passage of the initial shock is in good agreement with the experimental data. For the LES, the arrival of the reshock is indicated by the compression of the TMZ. For ODT, this compression is less prominent than for the LES because the LES TMZ prior to the arrival of the reshock was much wider. The evolution of the TMZ post reshock is characterized by an almost continuous growth without reaching saturation within the simulated time. These processes can similarly be seen in the ODT TKE plot, Fig. 13.5 (right). The initial shock deposits very little energy. At 3.5 ms the reshock arrives and energy starts to grow. The growth continues with a slightly decreasing slope till approximately 9.0 ms, at which point energy begins to decay.

In comparing ODT to LES, in the LES there are two distinct energy sources that increase the post reshock TMZ width, the arrival of the reshock and the arrival of the expansion wave. The expansion wave arrives just as the energy from the shock begins to decay, therefore the TMZ growth is almost continuous throughout. In ODT, only the energy created by the passage of a shock over an interface is modeled while the effects of the expansion wave are not. In Fig. 13.5 (right), it is seen that the energy starts to increase after the arrival of the reshock, grows for a period of time, and then begins to decay. It's important to note that the time span over which the STI deposits energy is not a hard set time span, but depends on the turnover time of each individual eddy (see Appendix F). The TKE comparison between ODT and LES is used from a qualitative point of view to show that the energy levels produced by ODT are in approximate agreement with that of LES.

Having presented detailed ODT, LES and VS comparisons for the  $Ma=1.50$  case, in Fig. 13.6 ODT and experimental computed widths of the TMZ are shown next for all  $Ma$  cases,  $Ma = 1.24, 1.43, 1.50, \text{ and } 1.98$ . The agreement



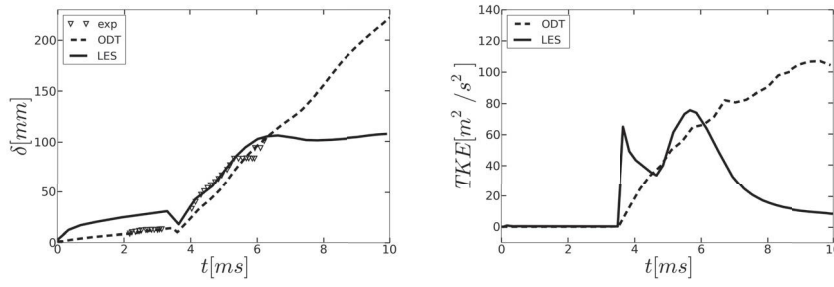


Figure 13.5: Evolution of the TMZ width  $\delta$  (left) and spatially averaged TKE (right) as a function of time for the  $Ma=1.50$  case. ODT (dotted), LES (solid), and on the left VS experimental data (triangle). On the right, the LES results show the total TKE, resolved plus subgrid. LES and experimental data are taken from [39] and [113] respectively.

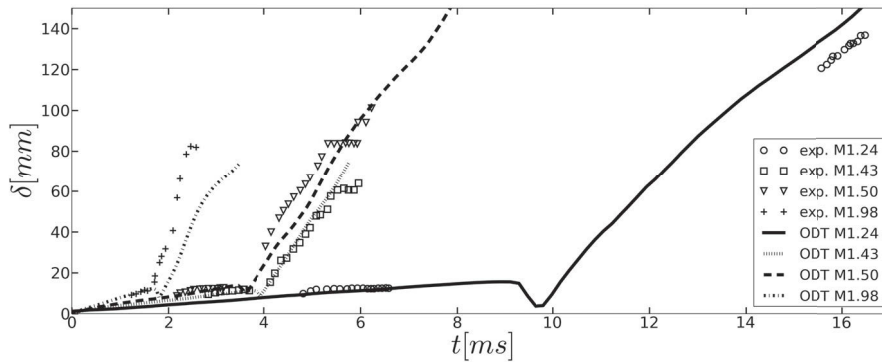


Figure 13.6: Evolution of the TMZ width  $\delta$  as a function of time for the  $Ma=1.24, 1.43, 1.50$  and  $1.98$  cases. Experimental data are taken from [113].

in growth rates for all four simulations post shock and post reshock with the experimental data is good, as shown in table 13.2. The arrival of the reshock is shown by the compression of the TMZ in the ODT results. In these regions there are no experimental points, therefore the VS results don't show this. ODT simulations were carried out for approximately the time interval for which experimental data is available.

Summarizing the non-reactive results, because the detailed physics of the reshock and expansion wave are not modeled, the ODT extension to shock-turbulence interaction is viewed as a rough attempt to capture the gross features of these cases. Therefore the main role of the comparisons to non-reactive cases has been to enable the setting of parameters so that the settings for the reactive cases are not arbitrary. Approximately capturing the post shock and post reshock TKE levels for the  $Ma=1.50$  case and TMZ growth rates for all  $Ma$  cases with one set of parameters serves this purpose. The non-reactive results serve as validation of the STI model, as in these cases dilatation induced instability (represented by the DL model) is minimal compared to shock induced instability represented by the STI model. More precisely, obtaining correct tim-

ing for the arrival of the reshock is a result of the hydrodynamic model, while obtaining correct mixing width growth rates is a result of the STI model.

### 13.3 REACTIVE RM INSTABILITY WITH RESHOCK

Having validated the compressible solver and having shown the capabilities of the STI model for non-reactive cases, model capabilities for the reactive shock tube with reshock numerical experiments by [Khokhlov et al. \[51, 53\]](#) are shown next. The 2D fully resolved simulations (2D-sim) involve a planar incident shock with Mach number 1.50 and 1.63 traveling through a stoichiometric air and acetylene ( $C_2H_2$ ) mixture, striking a pre-ignited laminar flame, reflecting from the endwall and restriking the now turbulent flame. The 2D-sim computational setup is a shock tube of 32 cm by 1 cm, with reflecting boundary conditions on the right, a zero gradient outflow boundary on the left, and symmetry conditions on the upper and lower boundaries. A schematic of the corresponding ODT 1D configuration with initial flow conditions is shown in [Fig. 13.7](#). As in the 2D-sim, a driven shock is initially placed 2 cm from the left boundary. The velocity of the gas is set to zero everywhere ahead of the shock and the initial temperature and pressure are  $T_0=293$  K and  $P_0 = 1.33 \times 10^4$  Pa respectively. Between the left boundary and the shock, there is a uniform flow with the post shock conditions determined from the Rankine-Hugoniot criteria for a shock with a given Mach number (see [Appendix C.2](#)). The left boundary condition provides a constant inflow of gas through this boundary until rarefaction and sound waves from the shock-flame interaction taking place inside the domain reach the boundary. Then the inflow is modified by outgoing waves. The center of the flame is initially 13 cm from the endwall and has an initial radius of 1.5 cm. The initial flame is set up as a discontinuity separating the unburnt gas from a region of adiabatic flame conditions. After molecular diffusion and heat conduction spread the discontinuity, chemical reactions begin and a self-consistent flame develops.

#### 13.3.1 Reactive RM instability: $Ma=1.50$ case

The laminar space-time density evolution of ODT for the  $Ma=1.50$  case is plotted in [Fig. 13.8](#). The incident shock passes through the flame causing a rarefaction and reflected shock that move upstream, and a transmitted shock that eventually reflects from the endwall. This reflected shock interacts again with

Table 13.2: Post shock and post reshock TMZ growth rates for ODT and VS.

Shock Mach number (Ma)	1.24	1.43	1.50	1.98	[-]
VS $(d\delta/dt)_{\text{post shock}}$	2.1	3.0	4.2	7.5	[m/s]
ODT $(d\delta/dt)_{\text{post shock}}$	2.0	2.5	4.3	7.0	[m/s]
VS $(d\delta/dt)_{\text{post reshock}}$	17.0	31.5	37.2	74.4	[m/s]
ODT $(d\delta/dt)_{\text{post reshock}}$	22	34	37	64	[m/s]

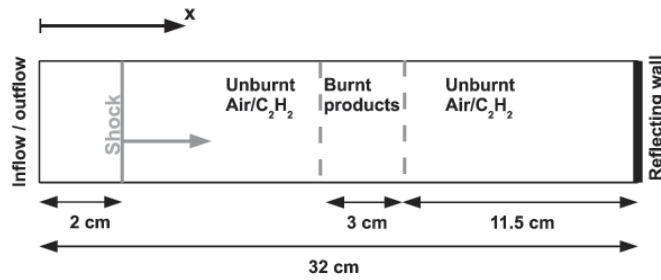


Figure 13.7: Geometry of the ODT 1D simulation domain.

the flame producing transmitted and reflected shocks. This situation continues to repeat, generating a series of shocks. Superimposed on the density plot are the 1D simulation (1D-sim) results from [53] for the evolution of the shock and the outlying edges of the flame. The comparison shows that the incident shock and flame dynamics are captured correctly. In Fig. 13.9, the corresponding total heat release rate ( $hr$ ) as a function of time is compared between ODT and the 1D-sim. This is a comparison of two gas dynamics solvers and serves as further verification of the 1D hydrodynamic solver. At time  $t=0$  there is a jump in the  $hr$  as the initially discontinuous flame smooths out. The  $hr$  begins to increase at 0.35 ms due to the interaction of the incident shock with the flame. Then it increases again at 0.7 ms as the reflected shock from the end-wall interacts with the flame. Minor oscillations in the  $hr$  plot continue as the flame interacts with subsequent reflected shocks that are now much weaker. The comparison of ODT to the 1D-sim shows that the ODT solver accurately captures the dynamics of pressure induced  $hr$  rise.

Because ODT is a stochastic simulation, turbulent results for a given flow configuration vary from realization to realization depending on the assignment of the initial random number seed. Therefore ensemble statistics are generally the best basis for comparison to results obtained by other methods (other models, DNS, or experiments). However, the comparison data that is available for the cases of present interest consists of individual flow realizations rather than ensemble data. Therefore, the comparisons that follow are based on simulated ODT realizations for each case that are run for several different random number seeds and the realization that shows best agreement with the corresponding case of [53] are presented. To illustrate sensitivities, additional results are shown for the first case considered below that indicate the run-to-run variability of the ODT results. There is unpublished anecdotal evidence of analogous sensitivity of 2D-sim results (E. Oran, personal communication).

ODT results for the turbulent space-time density evolution for the  $Ma=1.50$  case is plotted in Fig. 13.10. Comparison of the turbulent results in Fig. 13.10 to the laminar results in Fig. 13.8 shows that the flame post shock and post reshock grows much more slowly in the laminar case because there are no flame instabilities to increase the surface area and that in the turbulent case DDT occurs while in the laminar case it does not (see Appendix C.4 for details

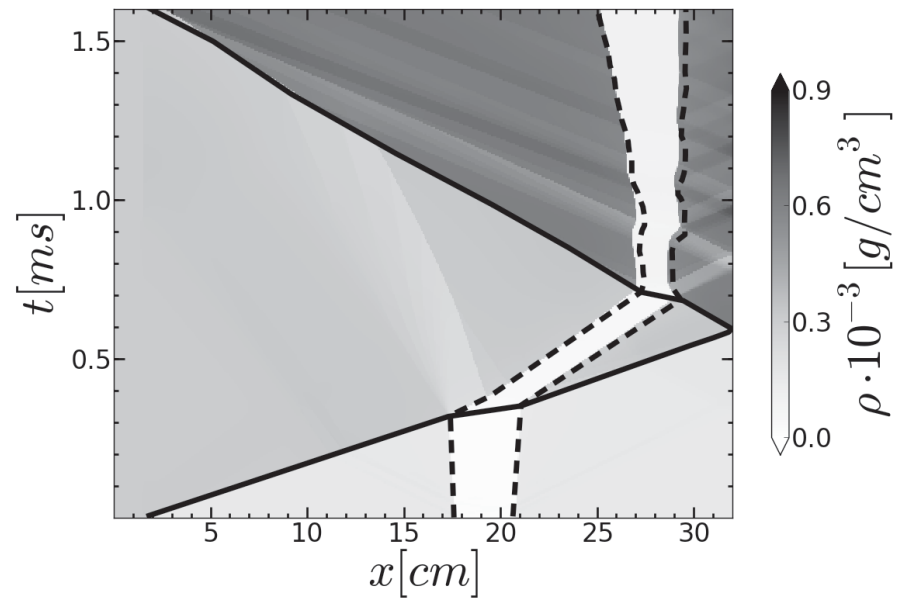


Figure 13.8: 1D simulation space-time plot of the shock (solid) and the outlying edges of the flame (dashed) from [53] are superimposed on the ODT space-time density evolution plot for the laminar  $\text{Ma}=1.50$  case.

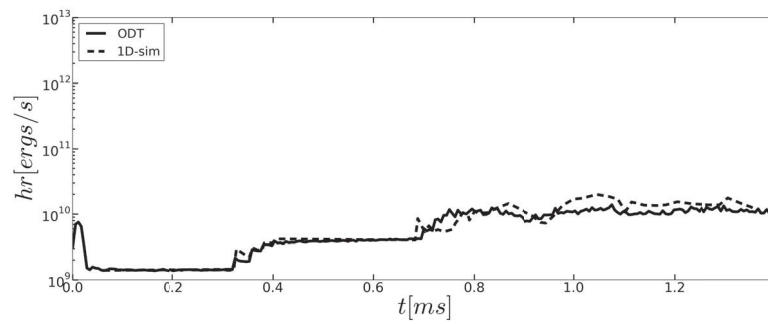


Figure 13.9: Total heat release rate ( $hr$ ) as a function of time for the laminar  $\text{Ma}=1.50$  case. ODT (solid) is compared to 1D simulation (1D-sim) (dashed) results from [53]. The results are multiplied by the channel cross section area.

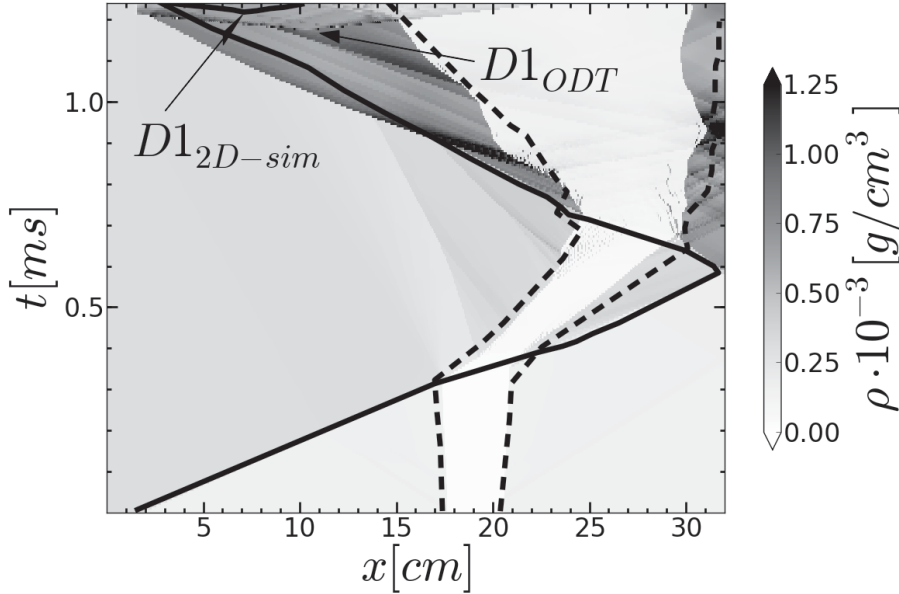


Figure 13.10: 2D-sim space-time plot of the shock (solid) and the outlying edges of the flame (dashed) from [53] are superimposed on the ODT space-time density evolution plot for the  $Ma=1.50$  case.  $D1_{ODT}$  and  $D1_{2D-sim}$  point to the origin of the DDT event in the ODT and the 2D-sim respectively.

of detonation theory). The turbulent ODT results further show streaks of unburnt fuel (e.g. at  $x=29$  cm and  $t=0.7$  ms) that are being mixed into the flame. Comparison of the ODT results to the superimposed 2D-sim space-time evolution of the shock and outlying edges of the flame in Fig. 13.10 shows that post shock and post reshock, ODT estimates the spreading of the flame reasonably well with slight underestimation of the flame width on the right edge of the flame. The turbulent flame brush width (designated as the shocked, heated, unreacted material to the left of the left edge of the flame) is in good agreement with results from the 2D-sim. DDT occurs in ODT in the turbulent flame brush at approximately  $x=10$  cm and  $t=1.2$  ms. This is recognized by the spreading of a spontaneous wave simultaneously to the left and to the right of the DDT point and burning up all unburnt material. This qualitatively reproduces results of the 2D-sim. In the 2D-sim, DDT occurred similarly in the turbulent flame brush at approximately  $x=7$  cm and  $t=1.25$  ms.

In Fig. 13.11, the corresponding  $hr$  as a function of time is compared between ODT and the 2D-sim. A reasonable agreement between ODT and the 2D-sim is obtained for the  $hr$  trend and amplitude. The  $hr$  rises as the initial shock (0.35 ms) and the reshock (0.7 ms) interact with flame. This is followed by a period of smaller heat release oscillations until DDT is reached in ODT just before 1.2 ms and in the 2D-sim at 1.25 ms indicated by the large jump in  $hr$ . In comparing the ODT turbulent results in Fig. 13.11 to the ODT laminar results in Fig. 13.9, the difference is due to the ODT turbulence models acting on top of the 1D hydrodynamic model. To the extent that the 2D-sim accu-

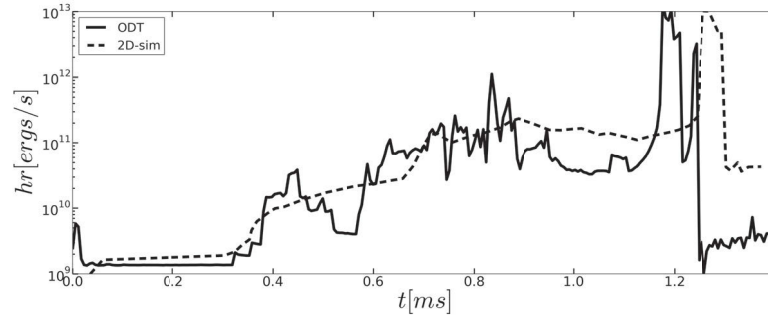


Figure 13.11: Total heat release rate ( $hr$ ) as a function of time for the  $Ma=1.50$  case. ODT (solid) is compared to 2D-sim (dashed) results from [53]. The ODT results are multiplied by the channel cross section area and the 2D-sim results are multiplied by the channel depth.

rately represents the 3D configuration, the Fig. 13.11 comparison thus serves as a validation of the ODT turbulence models.

In Fig. 13.12, ODT and 2D-sim pressure as a function of time at three different locations (12.8, 19.2 and 25.6 cm) are plotted. At  $x=12.8$  cm the pressure initially rises as the initial shock passes through at 0.24 ms and later slightly decreases (0.7 to 1.05 ms) due to the rarefaction. Then jumps are seen again in ODT at  $t=0.95$  ms and in the 2D-sim at  $t=1.05$  ms as the reflected shock from the wall passes through. The earlier pressure rise in ODT reflects the earlier arrival of the reshock, as also seen in Fig. 13.10. In ODT, this pressure rise is followed by a larger dip in the pressure than in the 2D-sim. At approximately 1.1 ms, another pressure wave passes the location and just before 1.2 ms DDT is indicated by the large increase in pressure. In the 2D-sim, this is qualitatively validated. After the passing of the reshock at 1.05 ms pressure oscillations ensue and DDT is recognized by the sudden large jump in the pressure (1.25 ms). Pressure at locations  $x=19.2$  and 25.6 cm shows similar behavior. The passing of the initial shock and the reshock are indicated by sudden rises in the pressure and the arrival of the DDT by the large jump in the pressure.

The turbulent results shown in Figs. 13.10 - 13.12 have been selected based on agreement with the 2D-sim results. In what follows the sensitivity of the ODT results is evaluated by varying the initial random number seed. In Figs. 13.13 - 13.15 the ODT space-time density evolution for the  $Ma=1.50$  case are shown with the 2D-sim results superimposed for reference. In all three variations it is seen that the flame spreading post shock and post reshock are in reasonable agreement with the 2D-sim results and yet a variation in the location and timing of the DDT event is seen. In Fig 13.13 (var. 1) two DDT events are observed in ODT. The first occurs at the right wall at approximately  $t=0.95$  ms. As this wave begins to travel to the left, it burns up the pocket of fuel remaining near the wall. Once it passed through the flame and reaches the unburnt heated shocked material it triggers a second DDT event at  $x=17$  cm and  $t=1.05$  ms. In Fig. 13.14 (var. 2) two DDT events are similarly observed. In this variation however the first DDT occurs at the left edge of the flame at

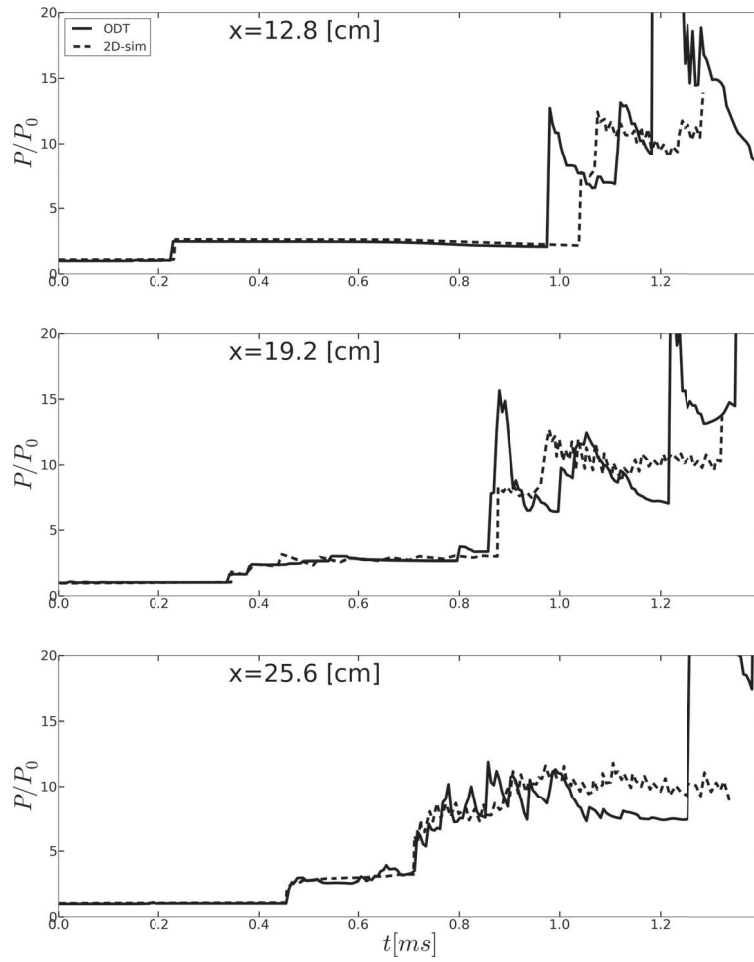


Figure 13.12: Pressure normalized by the initial pressure ( $P_0$ ) is plotted as a function of time evaluated at location  $x=12.8$  cm (top), 19.2 cm (middle) and 25.6 cm (bottom). ODT (solid), 2D-sim (dashed) results from [53].

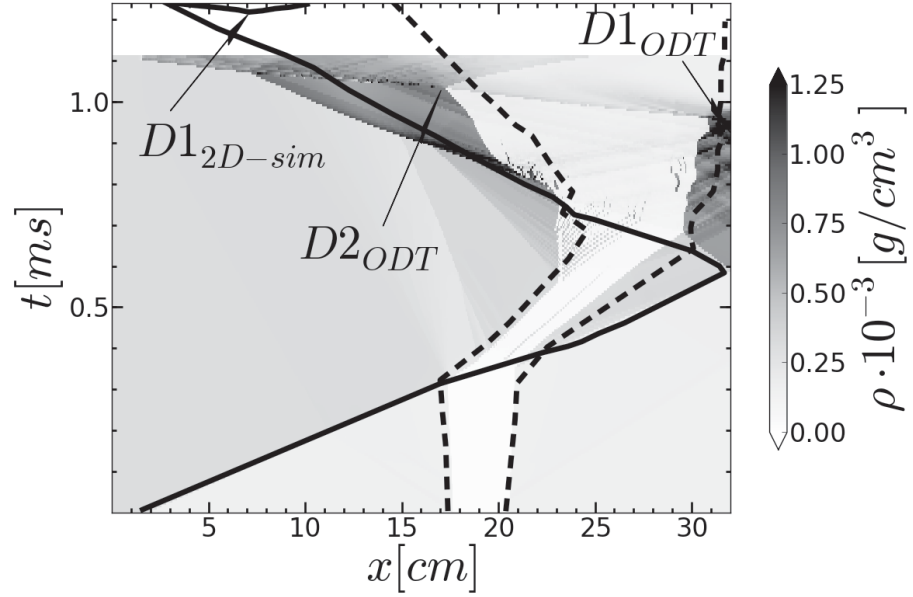


Figure 13.13: Variation 1 for the  $Ma=1.50$  case. 2D-sim space-time plot of the shock (solid) and the outlying edges of the flame (dashed) from [53] are superimposed on the ODT space-time density evolution plot for the  $Ma=1.50$  case.  $D1_{2D-sim}$  points to the origin of the DDT event in the 2D-sim.  $D1_{ODT}$  and  $D2_{ODT}$  point to the origin of the DDT events in ODT.

approximately  $x=21$  cm and  $t=0.97$  ms and travels simultaneously to the left and to the right. Once this wave reaches the unburnt pocket of gas at the right wall, it triggers the second DDT event. At this point all fuel is burnt up. Finally in Fig. 13.15 (var. 3) no DDT event is observed. The flame width continues to grow but a DDT event is not triggered.

These three variations serve as examples of the sensitivity of DDT events and represent additional physically plausible scenarios. Although the mixing levels in the three ODT simulations are approximately similar, as indicated by the spreading of the flame, large variations in the occurrence of DDT events are seen.

### 13.3.2 Reactive RM instability: $Ma=1.63$ case

Next, results for a higher Mach number case are presented. The turbulent space-time density evolution results of ODT for the  $Ma=1.63$  case are plotted in Fig. 13.16. Superimposed on the plot is the approximate space-time evolution of the shock and the outlying edges of the flame of the 2D-sim taken from [51]. Qualitative agreement is seen between ODT and the 2D-sim results, although post shock and post reshock flame spreading is underestimated in ODT. In ODT two separate, almost simultaneous, DDT events are seen. The first DDT event ( $D1_{ODT}$ ) occurs at the endwall at 0.85 ms. This consumes the small pocket of unburnt material at the endwall and then travels to the left



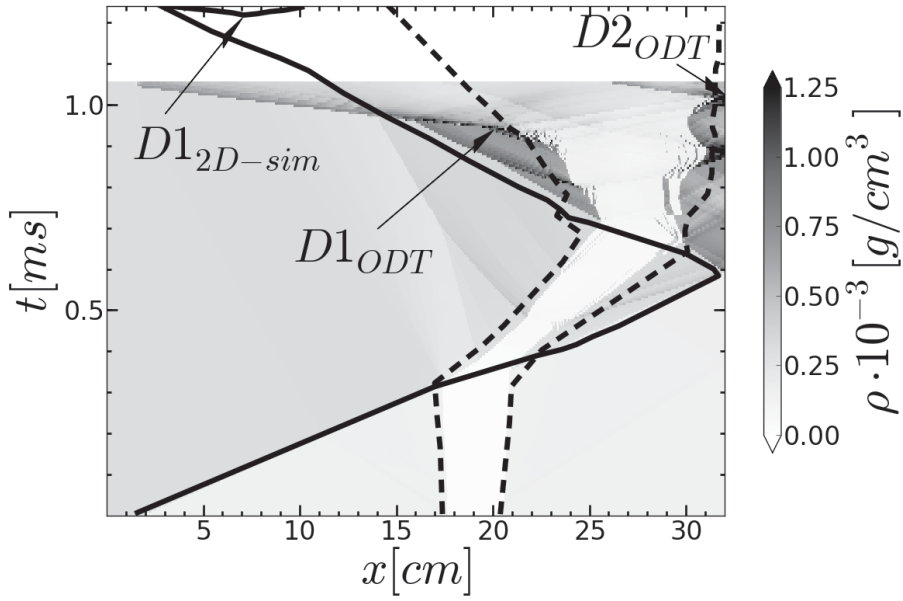


Figure 13.14: Variation 2 for the Ma=1.50 case. 2D-sim space-time plot of the shock (solid) and the outlying edges of the flame (dashed) from [53] are superimposed on the ODT space-time density evolution plot for the Ma=1.50 case.  $D1_{2D-sim}$  points to the origin of the DDT event in the 2D-sim.  $D1_{ODT}$  and  $D2_{ODT}$  point to the origin of the DDT events in ODT.

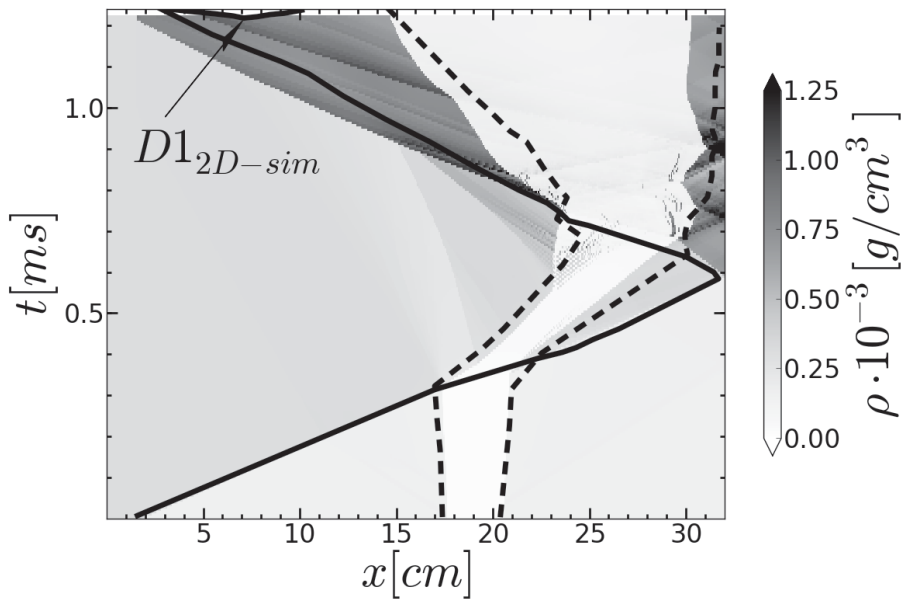


Figure 13.15: Variation 3 for the Ma=1.50 case. 2D-sim space-time plot of the shock (solid) and the outlying edges of the flame (dashed) from [53] are superimposed on the ODT space-time density evolution plot for the Ma=1.50 case.  $D1_{2D-sim}$  points to the origin of the DDT event in the 2D-sim.

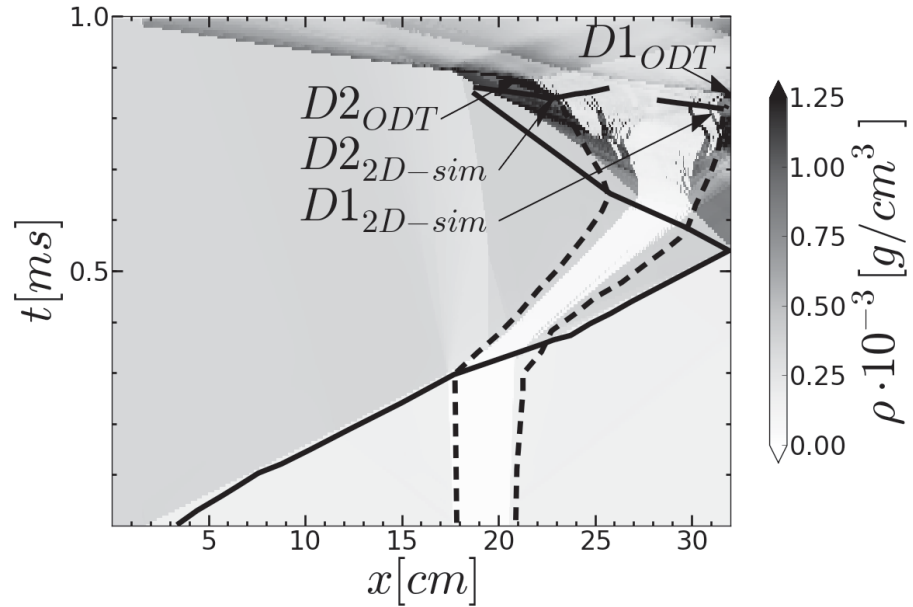


Figure 13.16: 2D-sim approximate space-time plot of the shock (solid) and the outlying edges of the flame (dashed) from [51] are superimposed on the ODT space-time density evolution plot for the  $Ma=1.63$  case. D1 and D2 point to the first and second DDT event respectively in ODT and the 2D-sim.

through the flame as a shock. The second DDT event ( $D2_{ODT}$ ) occurs prior to the arrival of the first DDT event at  $x=22$  cm and  $t=0.88$  ms inside the flame brush just at the left edge of the flame and propagates both to the right and to the left. These DDT events are in qualitative agreement with results of the 2D-sim. In the 2D-sim, the first DDT event ( $D1_{2D-sim}$ ) occurs similarly at the endwall 0.03 ms earlier at 0.82 ms and the second ( $D2_{2D-sim}$ ) occurs between 0.82 and 0.84 ms inside the flame brush prior to the arrival of the first DDT event [51].

The corresponding total heat release rate for ODT and the 2D-sim as a function of time is plotted in Fig. 13.17. The agreement between results is quite reasonable, although post shock hr is underestimated. This is in accordance with the slower post shock spreading of the ODT flame in Fig. 13.16. Comparing hr results between the  $Ma=1.50$  and the  $Ma=1.63$  case shows that post shock hr results are approximately similar. However, post reshock hr rise for the  $Ma=1.63$  case is steeper and DDT is observed approximately 0.15 ms sooner.

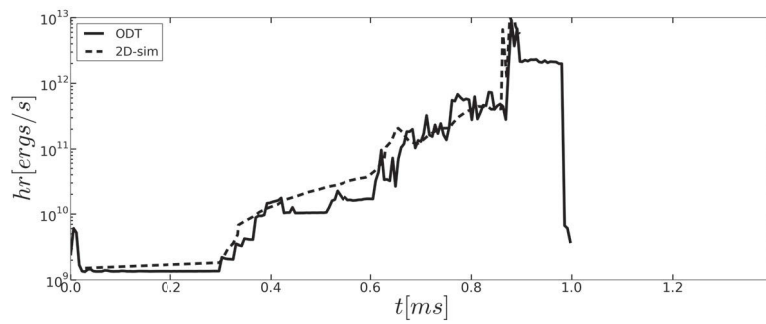


Figure 13.17: Total heat release rate ( $h_r$ ) as a function of time for the  $Ma=1.63$  case. ODT (solid) is compared to 2D-sim (dashed) results from [51]. The ODT results are multiplied by the channel cross section area and the 2D-sim results are multiplied by the channel depth.



## CONCLUSIONS

---

In this study, an adaptive grid Lagrangian incompressible code has been extended to include finite Mach number effects and a novel method has been presented for modeling shock-turbulence interaction for the study of DDT.

The compressible solver was validated against results from a Riemann solver for the Sod shock tube problem. Two cases were compared, one with an initial pressure difference of a factor 10 across the discontinuity and the second with an initial pressure difference of a factor 100. Results showed that for both cases the shock speed, shape, and complicated wave interactions with the reflecting walls and the contact discontinuity are captured accurately.

Simulation results for a non-reactive shock tube with comparison to experimental and LES results were presented for benchmarking and validation of the shock-turbulence-interaction model. Turbulent mixing width growth for four different Mach numbers were compared to experimental data. Comparisons showed good agreement for post shock and post reshock mixing width growth as a function of time for all Mach numbers. TKE as a function of time was compared to LES results for one Mach number. ODT TKE magnitude is in reasonable agreement with LES results, however the comparison showed that (1) ODT does not reproduce the saturation point and (2) it additionally highlighted modeling simplifications in ODT. The main goal has been to develop a reduced order model for studying shock-induced turbulence, its interaction with chemistry and the initiation of DDT. For this reason, the purposes of the comparisons to non-reactive results have been to choose tunable parameters in ODT so that settings for the reactive case are not arbitrary and to better understand the capabilities and limits of the shock-turbulence-interaction model in ODT. Matching TKE levels in order of magnitude for one Mach number and turbulent mixing zone width growth for all simulated Mach numbers with one set of parameters gives confidence in using these parameters for the reactive cases. A choice has been made to sacrifice case specific accuracy for generality and model limitations as exemplified by point (1) and (2) are considered acceptable. Additionally, as the main interest here is in studying DDT, which occurs prior to reaching the saturation point, inaccurate prediction of the timing of this and the ensuing decay of turbulence is not problematic for current purposes.

ODT results for a reactive shock tube for two Mach number cases were compared to 2D-sim results. Results for both Mach numbers showed that ODT is able to model the turbulence induced by the passing of a shock and its effects on chemistry by correctly capturing pressure and heat release rate rise as function of time. Flame growth is also in reasonable agreement with 2D-sim results. For the lower Mach number case, the 2D-sim predicts a single DDT event in the shocked heated unburnt region of the flame brush. ODT results matching this prediction were shown for comparison. However, as ODT

is a stochastic simulation it does not provide unique predictions. To demonstrate the sensitivity of the DDT event and to show physically plausible DDT events other than that predicted by the 2D-sim, additional ODT results were shown that were obtained by varying the initial random number seed. Results showed similar flame growth rates but the timing and location of the DDT events now differed.

This work has served as a proof of concept and demonstrated the potential of the developed methodology. It offers the prospect of cost-effective investigation of compressible combustion regimes that are not accessible by other methods. It may prove useful for studies of the dependence of details of DDT on the (presently) largely unknown chemical mechanisms under DDT conditions. Additionally, the strong sensitivity of DDT to the particular flow structure within each flow realization has been highlighted, and the model comparisons raise the fundamental question of why ODT and the 2D-sim agree as well as they do despite complexity of the phenomena and the distinct simplifications inherent in the two methods.

OUTLOOK

---

In addition to possible future work listed at the end of Sec. 14, the impact of driver-shock Mach number and Atwood number can also be studied in a parametric manner. The ideas proposed, exploit the cost-effective attribute of the tool developed.

The methodology itself has potential for further development. The shock capturing capability of the compressible formulation was tested for a maximum driver-shock Mach number of 1.98. To insure accurate flux calculations at higher Mach numbers, a Riemann solver could potentially be implemented. It is also unclear if changes in the initial level of perturbation of the flame or interface are reflected accurately in the intensity of the turbulence developed. Further testing is needed to better understand the limits and capabilities of the method developed.





Part IV

APPENDIX



## THERMODYNAMICS RELATIONS

## A.1 1ST LAW OF THERMODYNAMICS

The first law of thermodynamics states that energy can be neither created nor destroyed and it gives a quantitative expression to the principle of energy conservation. Formally, on a per unit mass basis it is written as

$$\Delta e = q - w \quad (\text{A.1})$$

where  $\Delta e$  is the total energy change of the system,  $q$  is the heat flow into the system, and  $w$  is the work done by the system. Contrary to usage in everyday language (e.g. heat flows, we heat), in thermodynamics heat is a mode of transfer of energy by virtue of a temperature difference. Hence, heat is the name of a process and not a form of energy. Work is defined as motion against an opposing force. The type of work that a gas can perform is pressure work which expands the volume,  $w = p dv = p d(\frac{1}{\rho})$  where  $v$  is the specific volume. Finally, the energy can be viewed as the capacity of a system to do work.

The total energy change can be split into particular forms as

$$\Delta e = \Delta e_k + \Delta e_p + \Delta \theta. \quad (\text{A.2})$$

Where  $e_k$  is the kinetic energy,  $e_p$  is the potential energy, and  $\theta$  is the internal energy. Neglecting changes in kinetic and potential energy and rewriting Eq. (A.1) in differential form gives

$$d\theta = \delta q - \delta w. \quad (\text{A.3})$$

This has been done to highlight an important difference between the quantities  $q$  and  $w$  and the property  $\theta$ . The property  $\theta$  depends only on the state of the system and thus  $d\theta$  represents an infinitesimal change in  $\theta$ . Integration gives the difference between two states:  $\int_1^2 d\theta = \theta_2 - \theta_1 = \Delta\theta$ . On the other hand,  $q$  and  $w$  are not properties, but path dependent processes. Thus  $\delta$  is used to denote an infinitesimal quantity and when integrated gives a finite quantity:  $\int_1^2 \delta q = q$  and  $\int_1^2 \delta w = w$ .

## A.2 IDEAL GAS RELATIONS

The ideal gas law is in fact the culmination of three different laws:

- Robert Boyle (1627-1691) showed that for a fixed amount of gas at constant temperature (isotropic), the pressure and volume are inversely proportional to one another,

$$pV = \text{const.} \quad (\text{A.4})$$

- Jacques Charles (1746-1823) showed that if the pressure is kept constant (isobaric), the volume is proportional to the temperature,

$$\frac{V}{T} = \text{const.} \quad (\text{A.5})$$

- J.L. Gay-Lussac (1778-1850) showed that if the volume is kept constant (isochoric), the pressure is proportional to the temperature,

$$\frac{p}{T} = \text{const.} \quad (\text{A.6})$$

Combining these laws and reformulating in terms of density, the ideal gas law becomes

$$p = \rho \frac{R}{\bar{M}} T = \rho \bar{R} T, \quad (\text{A.7})$$

where  $\bar{R}$  is the specific gas constant and defined as  $R/\bar{M}$ . The ideal gas relation holds under the following conditions:

- The size of the molecules is negligible in comparison to the distance between them.
- The molecules experience forces only during collisions (i.e. no intermolecular attraction).
- The gas molecules move randomly, frequently colliding with one another creating uniform pressure.
- All collisions are completely elastic.
- The kinetic energy of all gas molecules is directly proportional to the absolute temperature of the gas.

Real gases follow ideal gas behavior if their density is low enough that the gas molecules don't interact much with each other. A more detailed equation of state is for example the van der Waals equation, which describes both gases and liquids and takes into account molecules with non-zero volumes and subject to a pairwise inter-molecules attractive force.

## A.3 ENTHALPY

The enthalpy  $h$  is directly related to the internal energy  $\theta$  and is defined as

$$h \equiv \theta + \frac{p}{\rho} = \theta + \bar{R}T. \quad (\text{A.8})$$

It is infact only a clever book keeping tool used for taking into account the internal energy and energy used by the gas to do work on its surroundings [7].

## A.4 SPECIFIC HEAT

Heat capacity is a measure of the amount of heat needed to bring about a given rise in temperature. Water for example has a higher heat capacity than air. In thermodynamics, a distinction between two heat capacities is made depending on how the heating occurred. If the heating occurs under constant volume (i.e. no work is done in expanding the sample), the slope of a graph of the value of the internal energy plotted against temperature is called the heat capacity of the system at constant volume  $c_v$  and is defined as

$$c_v = \left( \frac{\partial \theta}{\partial T} \right)_v = \frac{d\theta}{dT} \quad \longrightarrow \quad d\theta = c_v dT. \quad (\text{A.9})$$

If however it is under conditions of constant pressure with the sample free to expand, then the energy supplied as heat going into expanding the sample needs to be accounted for. In this case, the slope of a graph of the value of enthalpy plotted against temperature is called the heat capacity of the system at constant pressure  $c_p$  and is defined as

$$c_p = \left( \frac{\partial h}{\partial T} \right)_p = \frac{dh}{dT} \quad \longrightarrow \quad dh = c_p dT. \quad (\text{A.10})$$

It then follows that under constant pressure more heat is needed to bring about the same temperature change as for heating under constant volume and hence  $c_p > c_v$ . The heat capacity ratio  $\gamma$  is defined as  $\gamma = c_p/c_v$ , which for an ideal gas is close to constant with respect to temperature. Under this assumption, a change in enthalpy is directly proportional to a change in internal energy as

$$\frac{dh}{d\theta} = \frac{c_p dT}{c_v dT} = \frac{c_p}{c_v} = \gamma \quad (\text{A.11})$$

A final useful relationship between  $c_p$  and  $c_v$  is arrived at by differentiating Eq. (A.8),

$$dh = d\theta + \bar{R}dT \quad \longrightarrow \quad \frac{dh}{dT} - \frac{d\theta}{dT} = \bar{R} \quad \longrightarrow \quad c_p - c_v = \bar{R}. \quad (\text{A.12})$$

## A.5 2ND LAW OF THERMODYNAMICS

Entropy is a state property just as internal energy, and is viewed a measure of disorder. If matter and energy are distributed in a disordered way, as in a gas, then the entropy is high. If matter and energy are stored in an ordered manner, as in a crystal, then the entropy is low. For a reversible or quasisteady process, the change in entropy  $s$  is the ratio of energy transferred as heat to or from a system to the temperature at which it is transferred from. On a per unit mass basis, this is written as

$$ds = \frac{\delta q}{T}. \quad (\text{A.13})$$

The word reversibly is important because the transfer of heat can be imagined as carried out with only an infinitesimal difference in temperature between the system and its surroundings [7]. In the everyday language a reversible process is one that can be done in reverse (e.g.rolling a wheel, compression of gas can be reversed by pulling out the piston), but in thermodynamics a reversible process is one that is reversed by an infinitesimal modification of the conditions in the surroundings [3]. To highlight the meaning of infinitesimal, take the following two examples:

- If a block of iron at 20 °C is immersed in a water bath at 40 °C, energy will flow as heat from the bath into the block, and an infinitesimal change in the temperature of the water will have no effect on the direction of flow.
- Consider a piston in equilibrium where the external pressure matches the internal pressure. Raising the external pressure infinitesimally and then lowering it infinitesimally reverses the process.

Considering these examples, one realizes that real processes are rarely ever reversible processes and therefore the usefulness of Eq. (A.13) is unclear. However, the usefulness of Eq. (A.13) comes from the fact that it can also be applied to irreversible processes with the realization that in such a case Eq. (A.13) only represents the minimum entropy change in the process under consideration [126].

The second law of thermodynamics formally states that the entropy change of any system and its surroundings is positive and approaches zero for any process which approaches reversibility [3]. That is

$$ds \geq 0. \quad (\text{A.14})$$

To obtain an expression for entropy change in terms of more familiar quantities, plugging Eq. (A.3) into Eq. (A.13) gives

$$ds = \frac{dh}{T} - \frac{1}{\rho T} dp. \quad (\text{A.15})$$

Now plugging in Eq. (A.7) and Eq. (A.10) for  $dh$  and  $\rho T$  gives

$$ds = c_p \frac{dT}{T} - \bar{R} \frac{dp}{p}, \quad (\text{A.16})$$

and upon integrating gives

$$s_2 - s_1 = c_p \ln \left( \frac{T_2}{T_1} \right) - \bar{R} \frac{p_2}{p_1}. \quad (\text{A.17})$$





When two fluids of different densities are in contact with each other and the interface is accelerated by some mechanism, a variety of fluid motions can ensue depending on the form and direction of the acceleration.

### B.1 RAYLEIGH-TAYLOR AND RICHTMYER-MESHKOV INSTABILITY

The basic mechanism for growth of initial small-scale perturbations in the RT and RM instabilities is the baroclinic generation of vorticity at the interface due to the misalignment of pressure and density gradients. The evolution of the vorticity field  $\vec{\omega} = \nabla \times \vec{u}$  is given by

$$\frac{D\vec{\omega}}{Dt} = \frac{1}{\rho^2} \nabla \rho \times \nabla p + \vec{u} (\nabla \cdot \vec{\omega}) - \vec{\omega} (\nabla \cdot \vec{u}) + \nabla \times \left( \frac{\nabla \cdot \tau}{\rho} \right). \quad (\text{B.1})$$

The first term on the RHS is the baroclinic production of vorticity, the second term is called vortex stretching and appears only in 3D flows, the third term is the vortex compression which is a result of compressibility effects, and the last term is due to viscous dissipation.

The initial configurations for the RT and RM instabilities are shown in Fig. B.1. In both cases the initial perturbation is represented by a half cosine wave of amplitude  $a_0$ , wave number  $\lambda$ , and interface thickness  $w$ . The density above (to the left) and below (to the right) of the interface for the RT (RM) configuration is given by  $\rho_-$  and  $\rho_+$  respectively. The accelerating mechanism for the RT instability is gravity  $g$ , while for the RM instability it is the shock with driver Mach number  $Ma_-$ .

The baroclinic generation of vorticity as given in Eq. (B.1) is shown schematically in Fig. B.2 for a shock traveling from left to right for the case of light fluid accelerating into heavy (L/H) and for the case of heavy accelerating into

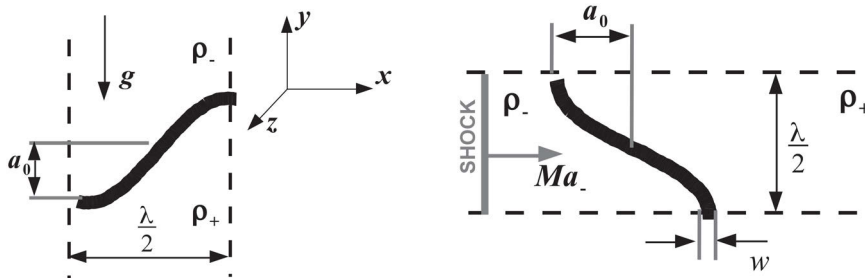


Figure B.1: Initial configuration of the RT (left) and RM (right) instability. The coordinate system shows  $x$  pointing to the right,  $y$  to the top and  $z$  out of the page.

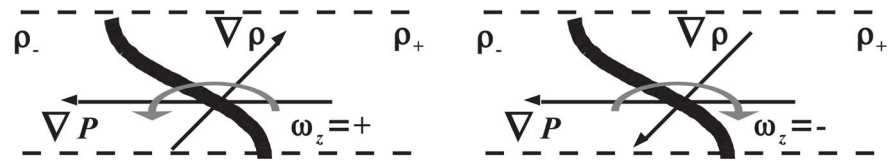


Figure B.2: Direction of baroclinic vorticity generation for L/H (left) and H/L (right) interface for the RM instability.

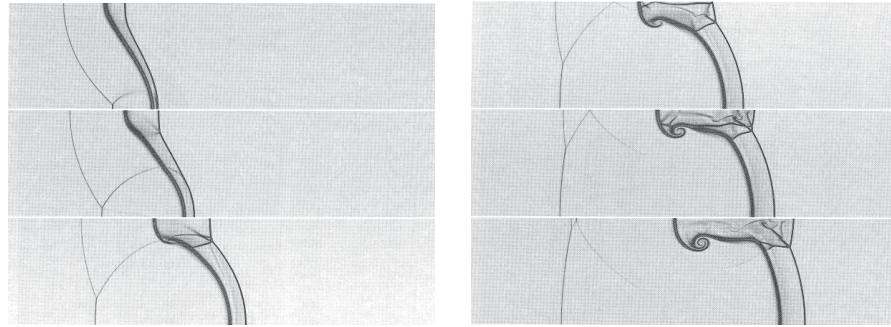


Figure B.3: Schlieren images of the initial (left) and developing (right) stages of the RM instability for a L/H interface. The figure is adopted from [78].

light (H/L). Shown in the figure is the direction of the pressure gradient across the incident shock  $\nabla p$ , the direction of the density gradient  $\nabla \rho$ , and the resulting direction of the generated vorticity  $\omega_z$  about the  $z$  axis. This has been done to highlight the difference between the direction of the resulting vorticity for an L/H and H/L interface. Schlieren images are shown in Fig. B.3 depicting the initial stages of the RM instability after the passing of a shock over an L/H interface. The images show the interface beginning to roll up due to the vorticity on it and starting to exhibit a mushroom-like structure. To the left of the interface, the shock reflected from the interface is seen as a thin line. The initial stages of a shock passing over a H/L interface are shown in Fig. B.4. When a shock moves from a region of higher density to a region of lower density, a rarefaction is reflected from the interface and moves to the left as opposed to a reflected shock for the L/H case. Additionally, the interface layer changes phase. This is a result of the transmitted shock having greater velocity in the light fluid than the incident shock traveling in the heavy fluid. This then causes the initial through of the interface to move ahead of the crest and reverses phase. The phase reversal of the interface has deposited negative vorticity in the layer, in contrast to the positive vorticity created by the L/H interface. As time progresses, the interface will begin to roll up similarly as in the L/H case.

After the initial rolling up of the spikes, secondary instabilities such as the shearing Kelvin-Helmholtz instability develops. The instability forms at a transition zone between two streams of different velocities, where shear causes initial perturbations to grow in time and lead to overturning of the interface. The development of the instability is shown in Fig. B.5, a detailed quantitative derivation can be found in [8]. As time progresses, a wide range of scales are obtained and a turbulent mixing zone between the two fluids develops.

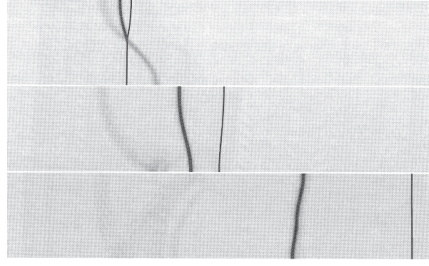


Figure B.4: Schlieren images of the initial stages of the RM instability for a H/L interface. The figure is adopted from [78].

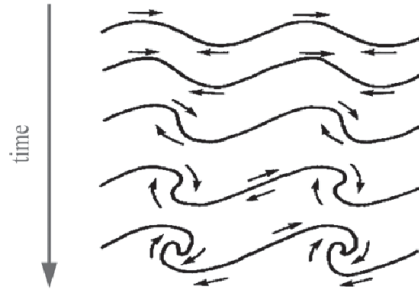


Figure B.5: Kelvin-Helmholtz instability developing from a single mode perturbation. The figure is adopted from [18].

Having described the basic mechanisms leading to growth of the initial perturbation, quantitative descriptions of the perturbation growth rates for the RT and RM instabilities are given next. Rayleigh [94] and Taylor [110] provided an analysis for the time evolution of the perturbation amplitude  $a(t)$  for two incompressible fluids separated by a sinusoidal interface ( $\rho_- > \rho_+$ ) under the constant acceleration of gravity  $g$  (see Fig. B.1). For the analysis, surface tension and viscosity were neglected and it was assumed that  $a_0 \ll \lambda$  and that the interface width  $w$  is infinitesimally small. Under these conditions, the equation obtained for the acceleration of the amplitude width  $\ddot{a}(t)$  is

$$\ddot{a}(t) = k \cdot g \cdot a(t) \cdot At, \quad (\text{B.2})$$

where  $k = 2\pi/\lambda$  is the wave length,  $At = (\rho_+ - \rho_-)/(\rho_+ + \rho_-)$  is the Atwood number, and  $a(t)$  is the perturbation amplitude over time  $t$ . Upon integrating Eq. (B.2), an expression for the perturbation growth rate  $\dot{a}(t)$  is obtained as

$$\dot{a}(t) = n \cdot a_0 \cdot e^{n \cdot t}, \quad n = -\sqrt{-g \cdot k \cdot At}. \quad (\text{B.3})$$

The analysis shows that the interface grows exponentially with time and that the equation holds for negative Atwood numbers. The development of the RT instability is shown schematically in Fig. B.6.

To describe the sinusoidal interface growth after the passing of a shock, Richtmyer [97] modified Taylor's analysis by using an impulsive force in the

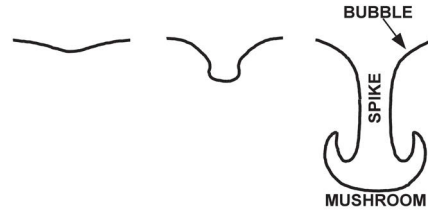


Figure B.6: Development of the the RT instability.

equation of motion instead of a constant force provided by gravity. Following from this, in Eq. (B.2)  $g$  is modified as  $g = \Delta v \cdot \delta(t = 0)$  where  $\Delta v$  is the change in velocity of the interface due to the passing of the shock and  $\delta(t = 0)$  is the Dirac delta function for which  $t = 0$  is the time of passing of the shock. Upon integrating the modified equation, the interface growth rate  $\dot{a}_R$  obtained by Richtmyer is written as

$$\dot{a}_R = k \cdot \alpha_0 \cdot \Delta v \cdot At. \quad (\text{B.4})$$

The result differs from that of RT in two aspects. First, Richtmyer's equation gives a linear growth rate with time opposed to the exponential growth given by RT. Second, Richtmyer's equation holds for both H/L and L/H interfaces. In cases of H/L interfaces,  $At < 0$ , the interface growth rate  $\dot{a}_R$  is negative which indicates the phase reversal as previously discussed and shown in Fig. B.4. Richtmyer stated that the interface continues to grow according to Eq. (B.4) until the linear theory no longer holds, that is until  $\alpha_0 \ll \lambda$  is no longer valid. Additionally, as the Atwood number  $At$  changes instantaneously due to the passing of the shock, the ambiguity arose as to whether the  $At$  should be taken from pre or post-shock conditions. Comparing results to numerical simulations of that time showed that using post-shock conditions for  $At$  provided better comparisons. Nine years later Meshkov [79] experimentally measured growth rates and verified that the growth rate is linear, but obtained growth rates below that predicted by Richtmyer. One possible explanation for the discrepancy is that Richtmyer assumed an interface of zero thickness in his analysis, however Brouillette and Sturtevant [12] showed that as the interface thickness increases, the growth rate drastically decreases.

## B.2 DARRIEUS-LANDAU INSTABILITY

Gas expansion due to heat release over a wrinkled flame leads to a distortion of streamlines creating flow divergence and velocity gradients that increase the wrinkling of the flame [16]. This form of instability mechanism was first recognized by Darrieus [21] in 1938 and independently by Landau [59] in 1944. The instability has since been termed the Darrieus-Landau instability. A detailed derivation and analysis of the instability is provided in [118], here only the fundamental aspects of the instability are presented. As shown in Fig. B.7, a streamline entering a flame convex towards the reactants is deflected downwards after passing through the flame. The velocity can be decomposed

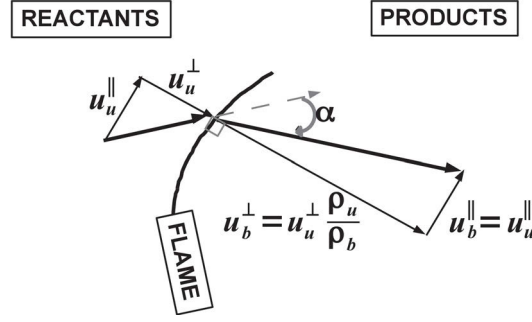


Figure B.7: Deflection of streamlines through a curved flame front.

into parts parallel  $u^{\parallel}$  and normal  $u^{\perp}$  to the flame. Assuming that the flame is infinitesimally thin, momentum conservation of the parallel component leads to  $u_u^{\parallel} = u_b^{\parallel}$  and mass conservation in the normal direction gives  $\rho_u u_u^{\perp} = \rho_b u_b^{\perp}$ . This shows, that the angle of deflection  $\alpha$  increases with increasing chemical heat release rate. That is, as the temperature of the burnt products rises,  $\rho_b$  decreases, and  $u_b^{\perp}$  increases increasing the deflection angle  $\alpha$ . For flames concave towards the reactants, a similar deflection is obtained but in the opposite direction.

A sinusoidal flame front is shown in Fig. B.8 where reactants approach the flame from the left with velocity  $u_{-\infty}$  equal to the laminar flame velocity  $S_u^L$ . Due to expansion over the flame, products far to the right of the flame have a velocity  $u_{+\infty} = u_{-\infty} \frac{\rho_u}{\rho_b}$ . As shown in Fig. B.7, expansion across the flame deflects streamlines. Due to the requirement that a stream tube with cross-section area  $A_0$  must be the same far upstream and far downstream of flame, since perturbations vanish there, the deflection of the streamline on the product side also cause a deflection on the reactant side near the flame. Otherwise  $A_0$  downstream would be less than  $A_0$  upstream. For a flame convex (concave) towards the reactants, the deflection causes streamlines to widen (narrow) which causes a decrease (increase) in velocity due to continuity as  $u_1 = \frac{A_0}{A_1} u_{-\infty}$ . This results in  $u_1 < S_u^L$  ( $u_1 > S_u^L$ ) such that the convex (concave) region begins to propagate upstream (downstream) resulting in an amplification of the initial perturbation. Figure B.9 shows typical images taken from high speed film of a flame during the development of the DL instability starting from an initial sinusoidal perturbation at  $t = 0$ .

The initial perturbation analysis of the DL instability gave the predicted growth rate  $\dot{\alpha}_L$  as

$$\dot{\alpha}_L = k \cdot S_u^L \cdot f(E), \quad (\text{B.5})$$

where  $E = \frac{\rho_u}{\rho_b}$  is the gas expansion ratio, and  $f(E)$  is a positive function of order unity vanishing for  $\rho_u = \rho_b$ . Eq. (B.5) predicts a continuous growth rate, however studies have shown that the influence of diffusion and gravity have a stabilizing effect on the instability and therefore development of the DL instability is not indefinite [15, 23].

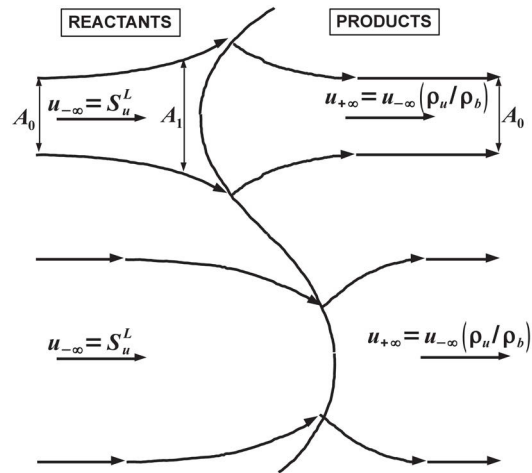


Figure B.8: Schematic illustration of the DL instability mechanism.

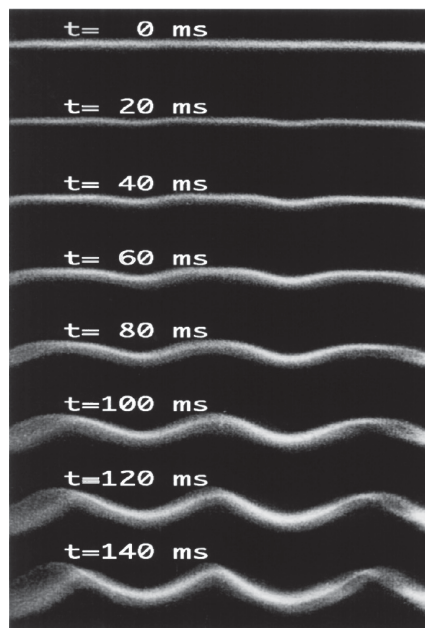


Figure B.9: Images taken from high speed film show the development of the DL instability starting from an initial perturbation. The images are adopted from [16].

As described up to this point and shown in Fig. B.9, for laminar flames the instability is of a purely diverging, non oscillatory character [118]. However, for turbulent flows, the effect of modifying the streamlines and the flame structure are coupled through a feedback mechanism which increases the complexity of the problem [17]. The coupling of turbulence and DL instability is therefore still an open research topic [111].





## NORMAL SHOCK THEORY

## C.1 SHOCK EQUATIONS

A shock wave is similar to a sound wave except that a shock wave has finite strength and the high gradients of velocity and temperature result in entropy production, due to which the isentropic relations cannot be used across the shock [58].

To derive the relationships between the properties on the two sides of the shock, consider a control volume as shown in Fig. C.1. State 1 and 2 can be taken arbitrarily close to each other because of the discontinuous nature of the shock. The velocities relative to the shock front moving at velocity  $u_s$  are

$$u'_1 = u_1 - u_s, \quad u'_2 = u_2 - u_s. \quad (\text{C.1})$$

The equations for continuity,  $x$ -momentum and energy written in terms of the shock coordinate system are:

$$\dot{m} = \rho_1 u'_1 = \rho_2 u'_2, \quad (\text{C.2})$$

$$p_1 + \dot{m}u'_1 = p_2 + \dot{m}u'_2, \quad (\text{C.3})$$

$$h_1 + \frac{(u'_1)^2}{2} = h_2 + \frac{(u'_2)^2}{2}. \quad (\text{C.4})$$

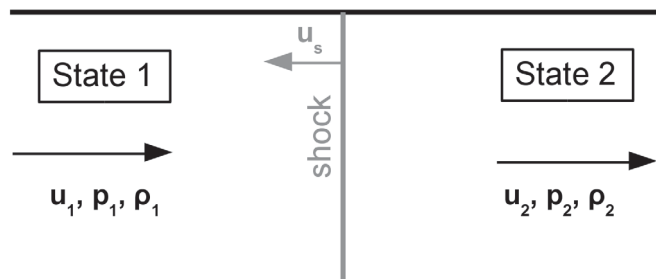


Figure C.1: Flow model of a normal shock propagating to the left at velocity  $u_s$ . State 1 is the state of the fluid moving into the shock and state 2 is the post shocked state.  $u$ ,  $p$ , and  $\rho$  represent the velocity, pressure and density respectively of state 1 and 2.

There are three equations and four unknowns ( $h_2, u_2, p_2, \rho_2$ ). To close the system the ideal gas relation is used for the equation of state

$$h = c_p T = \frac{\gamma R}{\gamma - 1} \frac{p}{\rho R} = \frac{\gamma p}{(\gamma - 1)\rho}. \quad (\text{C.5})$$

Plugging this into Eq. (C.4), gives

$$\frac{\gamma p_1}{(\gamma - 1)\rho_1} + \frac{(u_1')^2}{2} = \frac{\gamma p_2}{(\gamma - 1)\rho_2} + \frac{(u_2')^2}{2}. \quad (\text{C.6})$$

Up to this point, it hasn't been mentioned when a normal shock can occur. Note that there are two solutions to the equations, because Eq. (C.3) is quadratic when Eq. (C.2) is substituted in for  $\dot{m}$ . These two possible solutions refer to the direction of the flow. Physics dictates that there is only one possible solution and the second law of thermodynamics gives guidance on selecting the direction. Mathematically, the second law states that for an adiabatic shock, the entropy  $s$  must increase,

$$s_2 - s_1 > 0. \quad (\text{C.7})$$

Note, that the greater-equal sign was not used, as the process is irreversible, and therefore no equality can exist. For an ideal gas Eq. (C.7) can be reformulated as

$$\ln \frac{T_2}{T_1} - (\gamma - 1) \frac{p_2}{p_1} > 0. \quad (\text{C.8})$$

This shows that  $s$  can be expressed in terms of other properties, giving 4 unknowns ( $u_2, p_2, T_2, \rho_2$ ) and 5 equations (continuity, momentum, energy, state equation, and the second law of thermodynamics). These equations can be viewed as two different subset of equations. We can choose the first set to be the energy, continuity, and state equation and the second set to be the momentum, continuity, and state equation. In both sets the second law is included. The solution of both these sets produce a range of possible solutions. The first case, known as Fanno flow, assumes no heat transfer and variable momentum transfer. If one solves the second set, known as Rayleigh flow, the degree of freedom is energy (i.e., the amount of energy added to the shock) and the flow is similar to a frictionless flow with the addition of heat.

Since the shock has no heat transfer (a special case of Rayleigh flow) and there isn't any momentum transfer (a special case of Fanno flow), the intersection of these two curves is the actual solution [77]. This is schematically depicted in Fig. C.2. Additionally shown is the  $M = 1$  crossing for the Fanno and Rayleigh lines. It is seen that the second law dictates that the gas flows from a supersonic flow to a subsonic flow, that is from state 1 to state 2.

These results and the relations discussed in Sec. C.2 show that a physically possible shock is always a compression shock; pressure, density and temperature increase, while the absolute value of the relative velocity decreases [114].

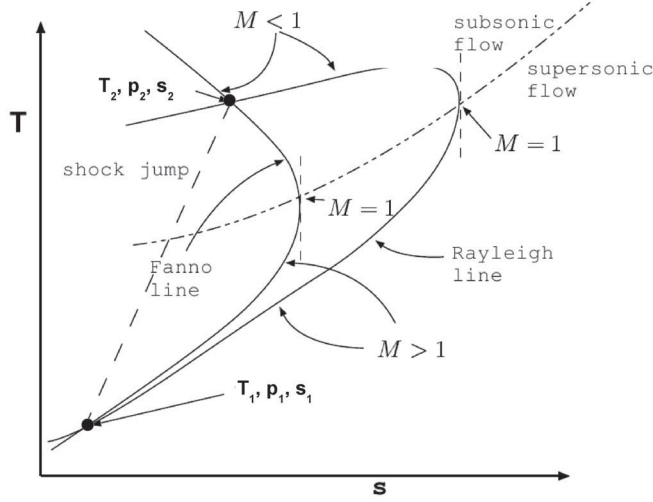


Figure C.2: Fanno and Rayleigh lines plotted against entropy  $s$  and temperature  $T$  on the  $x$  and  $y$  axis respectively. The figure is adopted from [77].

## C.2 RANKINE-HUGONIOT RELATIONS

Take the continuity, momentum, energy and state equation, Eqs. (C.2-C.5), to derive relations between states 1 and 2 for the four unknown variables ( $u'_2$ ,  $p_2$ ,  $T_2$ ,  $\rho_2$ ).

Elimination of  $\rho_2$  and  $u'_2$  from these gives

$$\frac{p_2}{p_1} = 1 + \frac{2\gamma}{\gamma + 1} \left[ \frac{\rho_1 (u'_1)^2}{\gamma p_1} - 1 \right]. \quad (\text{C.9})$$

This can be expressed in terms of the upstream relative velocity Mach number  $M'_1$  by noting that  $M'_1 = \frac{u'_1}{\sqrt{\gamma p_1 / \rho_1}} = \frac{u'_1}{\sqrt{\gamma R T_1}}$

$$\frac{p_2}{p_1} = 1 + \frac{2\gamma}{\gamma + 1} [(M'_1)^2 - 1]. \quad (\text{C.10})$$

Using the momentum equation and the relation  $\rho u^2 = \rho c^2 M^2 = \gamma p M^2$ , a relation between  $M'_1$  and  $M'_2$  can be written as

$$p_1 + \gamma p_1 (M'_1)^2 = p_2 + \gamma p_2 (M'_2)^2. \quad (\text{C.11})$$

Combining Eqs. (C.10) and (C.11) gives

$$(M'_2)^2 = \frac{(\gamma - 1)(M'_1)^2 + 2}{2\gamma(M'_1)^2 + 1 - \gamma}. \quad (\text{C.12})$$

Relations for density, relative velocity, and temperature ratios can be similarly obtained. They are

$$\frac{\rho_2}{\rho_1} = \frac{u'_1}{u'_2} = \frac{(\gamma + 1)(M'_1)^2}{(\gamma - 1)(M'_1)^2 + 2}. \quad (\text{C.13})$$

$$\frac{T_2}{T_1} = 1 + ((M_1')^2 - 1) \frac{2(\gamma - 1)}{(\gamma + 1)^2} \frac{\gamma(M_1')^2 + 1}{(M_1')^2}. \quad (\text{C.14})$$

The normal shock relations Eqs. (C.10,C.12-C.14) were worked out independently by Rankine (1870) and Hugoniot (1889) and are known as the Rankine-Hugoniot relations [58].

### C.3 LIMIT OF AN INFINITELY STRONG SHOCK

In this section the behavior of the Rankine-Hugoniot relations are shown for the incident shock strength tending to infinity. The intensity of the shock can be characterized by the upstream relative Mach number  $M_1'$ . Taking the limits of Eqs. (C.10), (C.13) and (C.14) as  $M_1' \rightarrow \infty$  gives

$$\frac{p_2}{p_1} = 1 + \frac{2\gamma}{\gamma + 1} [(M_1')^2 - 1] \implies \frac{2\gamma}{\gamma + 1} (M_1')^2, \quad (\text{C.15})$$

$$\frac{\rho_2}{\rho_1} = \frac{u_1'}{u_2'} = \frac{(\gamma + 1)(M_1')^2}{(\gamma - 1)(M_1')^2 + 2} \implies \frac{\gamma + 1}{\gamma - 1}, \quad (\text{C.16})$$

$$\begin{aligned} \frac{T_2}{T_1} &= 1 + ((M_1')^2 - 1) \frac{2(\gamma - 1)}{(\gamma + 1)^2} \frac{\gamma(M_1')^2 + 1}{(M_1')^2} \\ &\implies (M_1')^2 \frac{2\gamma(\gamma - 1)}{(\gamma + 1)^2}. \end{aligned} \quad (\text{C.17})$$

This shows that as the strength of the shock tends to infinity,  $p_2/p_1$  and  $T_2/T_1$  tend to infinity with  $(M_1')^2$ , but that the compression is limited to  $\rho_2/\rho_1 = 4$  for a monatomic gas ( $\gamma = 5/3$ ) and  $\rho_2/\rho_1 = 6$  for a diatomic gas ( $\gamma = 7/5$ ).

### C.4 BASICS OF DETONATION THEORY

In Sec. 13.3 results for DDT are shown and therefore an introduction to deflagration and detonation is given here. There are two distinct mechanisms for the propagation of combustion. In one, termed deflagration, the chemical reaction propagates through a gaseous mixture of fuel and oxidants due to diffusion of heat and species from the burning gas to that which is still unburned. Typical flame propagation is of the order of cm/s. A flame in a hydrogen/oxygen mixture has one of the fastest propagating velocity and propagates at about 9 m/s, while a flame in a mixture of 6% methane/air is one of the slowest propagating at about 5 cm/s. Another type of mechanism for the propagation of combustion involves shock waves, termed detonation. The shock wave compresses and heats the gas as it passes through the shock front so that the

temperature of the combustible gas mixture behind the shock increases. If the shock wave is sufficiently strong, the rise in temperature behind the shock may be sufficient to initiate combustion. The shock wave will then ignite the gas mixture as it moves through the mixture [64]. Typical propagation velocity of the combustion in this case is some hundreds to some thousands of m/s.

Mallard and LeChatelier [72] were the first to suggest compression as being a mechanism for combustion propagation. The thermodynamic analysis was later carried out by Chapman [14] and Jouguet [41] (CJ) in the early nineteen hundreds. In the CJ theory, a detonation wave is represented as a shock wave (infinitely thin) with energy release inside the wave front. This theory was then improved by Zel'dovich [123] and independently by von Neumann [115] and Döring [25] to account for deflagration (a wave of finite thickness) and become known as the ZND detonation theory.

Before continuing with detonation theory, it is first useful to construct a  $p, v$  diagram, where  $v = 1/\rho$  is the specific volume, for a shock traveling in an inert ideal gas with constant specific heats. The curve relating pre and post shock conditions on a  $p, v$  diagram passing through initial state  $p_1, v_1$  is called the Hugoniot or shock adiabat curve [124] and is depicted in Fig. C.3 as curve H1. The relation between an arbitrary point  $p, v$  on curve H1 is given by

$$\frac{p}{p_1} = \frac{(\gamma + 1)v_1 - (\gamma - 1)v}{(\gamma + 1)v - (\gamma - 1)v_1}, \quad (\text{C.18})$$

which is found by combining the continuity (C.2), momentum (C.3), and energy (C.4) equations and by plugging in the ideal gas relation for equation of state (C.5). Note that curve H1 does not extend beyond point  $v_1$ , as a physically possible shock is always a compression shock and therefore specific volume must decrease.

#### c.4.1 Zel'dovich-Neumann-Döring detonation theory

The ZND theory is described first as it is more general than the CJ theory. When a shock passes a point, reaction begins at that point and continues for time  $\tau_r$  until all the gas at that point is burned. As the shock strength increases  $\tau_r$  decreases on account of increasing reaction rates with increasing temperature. Therefore, a chemical reaction zone of width  $l_r = u_s \tau_r$ , where  $u_s$  is the speed of the shock, will move with the shock. The detonation wave is then taken to be the shock wave together with the reaction zone.

A second Hugoniot curve depicted by H2 is shown in Fig. C.3. The offset between H1 and H2 represents the difference between the enthalpy of unburnt reactants (depicted by H1) and burnt products (depicted by H2). H2 always lies above H1, because after combustion a higher temperature is reached and the gas pressure is therefore greater than it would be in the unburned gas for the same specific volume.

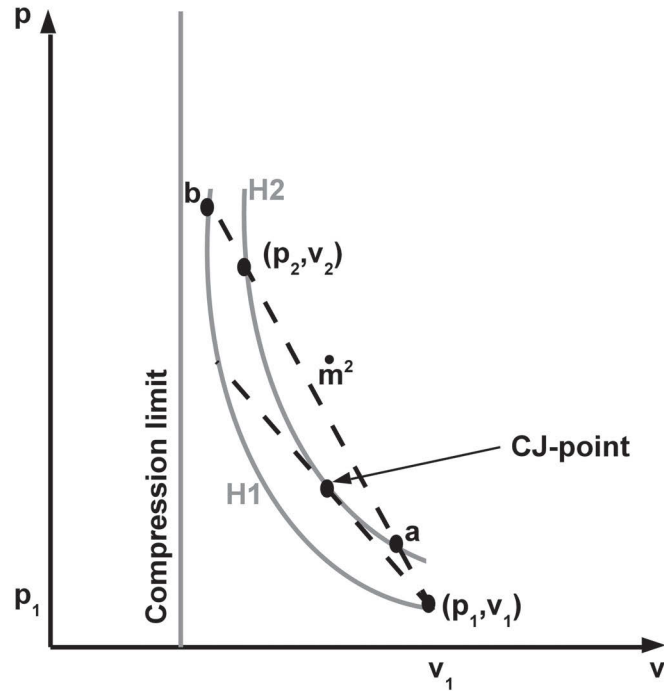


Figure C.3: A  $p, v$  diagram. H1 and H2 are the Hugoniot curves of the unburnt and burnt mixtures respectively.

To determine the final state of the gas, a curve that connects curve H1 and H2 needs to be drawn. To achieve this, combine the continuity (C.2) and momentum (C.3) equation to arrive at

$$\dot{m}^2 = (u'_1 \rho_1)^2 = \frac{p_2 - p_1}{v_1 - v_2}. \quad (\text{C.19})$$

This is the mass flux density (also termed Rayleigh line) and as it is a consequence of only the continuity and momentum equation, it holds not only for the initial unburnt and final shocked and burnt gas mixture, but for all intermediate states as well. In Fig. C.3 this is depicted by the straight line marked  $\dot{m}^2$  going through both H1 and H2. It is clear from the plot that the higher the final pressure, the larger the slope and the higher the mass flux density is.

Putting all the pieces together. The leading front of the detonation wave is a true shock wave moving into an unburned mixture denoted by point  $(p_1, v_1)$  in Fig. C.3. The gas is compressed and heated along curve H1 to a state denoted by point b. As chemical reaction begins in the compressed gas, the gas expands and pressure decreases moving downwards along line  $\dot{m}^2$ . This proceeds until combustion is complete, the final state of the gas being represented by point  $(p_2, v_2)$ . The lower crossing of line  $\dot{m}^2$  with curve H2, point a, cannot be reached for a gas in which combustion is caused by compression and heating in a shock wave [64]. The lower point is termed weak end state, while the upper point is termed strong end state.

### c.4.2 *Chapman-Jouget detonation theory*

The CJ theory begins by realizing that of all the Rayleigh lines drawn starting from point  $(p_1, v_1)$  in Fig. C.3, only the tangent has a single common point (point CJ) with line H2. It was then verified, that of all the possible Rayleigh lines, only the one crossing at point CJ was characterized by steady-state propagation. The steady state condition means that the shock front and the plane of the end of reaction propagate at the same velocity [22]. The theory then goes on to reason that to preserve steady-state motion, the shock wave responsible for detonation ignition must not be weakened by rarefaction waves appearing behind the detonation. This requires that the products behind the detonation travel at supersonic speeds as rarefaction waves move in the products with the local velocity of sound [26]. Therefore, a detonation wave propagates at the speed of sound particular to each gas mixture and initial state.

If the detonation is caused by a shock wave, which is produced by some external source and is then incident on the gas, any point on the upper part of the curve H2 may correspond to the detonation. If the detonation is due to the combustion itself, the detonation corresponds to the CJ point.





The Darrieus-Landau (DL) instability model described in Sec. 5.3.2 is the first demonstration of a strategy for incorporating flow acceleration effects into ODT. Another such effect is the shock-turbulence interaction (STI) in Sec. 12.1.2. To provide context for these formulations and related model extensions, the formal basis for incorporating these effects into ODT is explained.

Focusing on DL specifically, the instability can be viewed from either a kinematical or a dynamical viewpoint. Kinematically, dilatation at a curved flame surface produces streamwise acceleration on one side of the flame and deceleration on the other (see Appendix B.2). This instability mechanism cannot be captured on the 1D ODT domain. The failure of ODT to capture the instability kinematically does not violate any conservation laws. Thus, the absence of this mechanism in ODT does not indicate any internal model inconsistency. Nevertheless, to achieve the best possible model representation of turbulent combustion, it is desirable to incorporate a treatment of the DL instability.

This is done by adopting a dynamical viewpoint. Consider a fluid parcel that is accelerated by flame dilatation. Viewed in the accelerating reference frame, the fluid is subject to a d'Alembert force that is formally the negative of the gravitation force in the context of the Rayleigh-Taylor (RT) instability [54]. Accordingly, the response of the fluid parcel to acceleration can be analyzed by supposing instead that it is subject to the corresponding gravitational field. If there is density variation within the fluid parcel in the direction aligned with gravity, then density increase in the direction opposite to the orientation of the gravity vector implies gravitational instability. In other words, an instability exists if dilatation is accelerating light fluid into heavy. This is a formal statement of the conceptual analogy between the DL instability (or dilatational effects more generally) and the RT instability.

In this context, ODT provides a dynamical pathway to represent the instability. The likelihood of a prospective eddy event is based on 'available energy,' a construct that incorporates the net change in gravitational potential energy caused by the eddy. The DL analog of this potential-energy contribution is shown in Eq. (5.14). In this manner, the ODT DL contribution can increase the intensity of a turbulent flow or initiate turbulence in a non-turbulent flow.

The need for this approach is related to the instantaneous nature of an ODT eddy. The corresponding fluid parcel in a 3D physical flow executes an eddy motion during some finite time interval. During this time interval, it is subject to any accelerations generated by the surrounding flow field and it can respond accordingly. In contrast, an ODT eddy is instantaneous and therefore is not subject to displacement by dilatation-induced acceleration. Therefore ODT does not automatically provide a mechanism for eddies to be influenced by dilatational flow, hence the introduction of the DL model in Sec. 5.3.2, and the introduction of other such treatments.

The underlying concept is that the effect of dilatation on ODT is modeled as reference-frame acceleration of ODT eddies. Importantly, this concept is applied on a cell-by-cell basis within the range of the eddy, as indicated by the spatial variation of the acceleration within the integrand of in Eq. (5.14).

Though the d'Alembert's principle allows for modeling acceleration effects in ODT and drawing an analogy between dilatational and gravitational acceleration, the two forms of acceleration are not treated fully equivalently within ODT. In a gravitational field, the eddy-induced change of gravitational potential energy implies an equal-and-opposite change of kinetic energy, where the kinetic energy change is implemented during an ODT eddy event. This conserves total energy assuming there is an inexhaustible reservoir of gravitational potential energy. In contrast, the notional 'dilatational potential energy' change implied by Eq. (5.14) does not correspond to any external inexhaustible potential energy source. Therefore, the DL potential energy change is not based on an external energy source analogous to the gravitational potential energy reservoir. The consequence is that energy conservation requires that no kinetic energy change corresponding to the potential energy change should be applied.

## DETAILS OF COMPRESSIBLE NUMERICAL IMPLEMENTATION

---

The starting point for the compressible formulation is the set of variable density zero-Mach-number equations in one spatial dimension in a Lagrangian framework on an adaptive grid developed in [66]. Here the formulation in [66] is followed and the necessary changes to the equations to include finite-Mach-number effects are made.

### E.1 BALANCE EQUATIONS

The Eulerian transport equations, Eqs. (11.1 - 11.4), are rewritten with the eddy terms  $\overline{\epsilon\epsilon}$  ignored in order to focus on the time advancement between eddy events as

$$\frac{D}{Dt}\rho = -\rho\frac{\partial u_1}{\partial x}, \quad (\text{E.1})$$

$$\frac{D}{Dt}u_i = -\frac{1}{\rho}\frac{\partial p}{\partial x}\delta_{i1} + \frac{1}{\rho}\frac{\partial \sigma_{i1}}{\partial x}, \quad (\text{E.2})$$

$$\frac{D}{Dt}Y_s = \frac{\dot{\omega}_s}{\rho} - \frac{1}{\rho}\frac{\partial j_s}{\partial x}, \quad (\text{E.3})$$

$$\frac{D}{Dt}h = -\frac{1}{\rho}\frac{\partial q}{\partial x} + \frac{1}{\rho}\frac{Dp}{Dt} + \frac{1}{\rho}\sigma_{i1}\frac{\partial u_i}{\partial x}. \quad (\text{E.4})$$

In the present context, the material derivative  $D/Dt$  is defined as  $D/Dt \equiv \partial/\partial t + u_1\partial/\partial x$ .

Next, the formulation for  $Dp/Dt$  is shown. First, the equation of state is rewritten in the form  $p = \rho RT \sum_{s=1}^{n_s} Y_s/M_s$ , where  $M_s$  is the molecular weight of species  $s$ . Taking the material derivative of this equation gives

$$\frac{Dp}{Dt} = \frac{RT}{\bar{M}}\frac{D\rho}{Dt} + \frac{\rho R}{\bar{M}}\frac{DT}{Dt} + \rho RT \sum_{s=1}^{n_s} \frac{1}{M_s} \frac{DY_s}{Dt}. \quad (\text{E.5})$$

The material derivatives on the right hand side of Eq. (E.5) are evaluated using the transport equations for density (E.1), for species mass fraction (E.3) and for temperature using  $h = h(T, Y_s)$  to obtain

$$\frac{Dh}{Dt} = \frac{\partial h}{\partial T} \frac{DT}{Dt} + \sum_{s=1}^{n_s} \frac{\partial h}{\partial Y_s} \frac{DY_s}{Dt} = c_p \frac{DT}{Dt} + \sum_{s=1}^{n_s} h_s \frac{DY_s}{Dt}. \quad (\text{E.6})$$

Here,  $c_p$  is the specific heat capacity at constant pressure. The relation  $\frac{\partial h}{\partial Y_s} = h_s$  has been used and is found by taking the partial derivative of the enthalpy  $h = \sum_{s=1}^{n_s} h_s Y_s$  with respect to  $Y_s$ . Solving for  $DT/Dt$  gives

$$\frac{DT}{Dt} = \frac{1}{c_p} \frac{Dh}{Dt} - \frac{1}{c_p} \sum_{s=1}^{n_s} h_s \frac{DY_s}{Dt}. \quad (\text{E.7})$$

Plugging Eqs. (E.3) and (E.4) into Eq. (E.7) gives

$$\frac{DT}{Dt} = \frac{1}{\rho c_p} \left( -\frac{\partial q}{\partial x} + \frac{Dp}{Dt} + \sigma_{i1} \frac{\partial u_i}{\partial x} \right) + \frac{1}{\rho c_p} \sum_{s=1}^{n_s} h_s \left( \frac{\partial j_s}{\partial x} - \dot{\omega}_s \right). \quad (\text{E.8})$$

Plugging Eqs. (E.1), (E.3), and (E.8) into Eq. (E.5), and solving for  $Dp/Dt$  yields

$$\frac{Dp}{Dt} = -\gamma p \frac{\partial u_1}{\partial x} + \gamma p \Psi, \quad (\text{E.9})$$

where  $\gamma$  is the ratio of specific heats,  $\gamma = c_p/c_v = c_p/(c_p - R)$ , and  $\Psi$  is given by

$$\begin{aligned} \Psi = & \frac{1}{\rho c_p T} \left( -\frac{\partial q}{\partial x} + \sigma_{i1} \frac{\partial u_i}{\partial x} + \sum_{s=1}^{n_s} h_s \left( \frac{\partial j_s}{\partial x} - \dot{\omega}_s \right) \right) \\ & - \frac{\bar{M}}{\rho} \sum_{s=1}^{n_s} \frac{1}{M_s} \left( \frac{\partial j_s}{\partial x} - \dot{\omega}_s \right). \end{aligned} \quad (\text{E.10})$$

## E.2 SPATIAL DISCRETIZATION

Consider now the 1D domain. A finite volume formulation is used, where space is discretized into  $N$  computational cells of size  $\Delta x_k$  where  $k \in \{0, 1, 2, \dots, N-1\}$ . Note that, due to the mesh adaption algorithm,  $N$  is not constant in time. Properties are defined to lie at cell centers  $x_k$  and to be uniform within a cell. The boundaries of the  $k^{\text{th}}$  cell are denoted by the subscripts  $k \pm \frac{1}{2}$ . On the adaptive mesh, cell faces move with advecting velocity  $u_1$  so that advective fluxes are eliminated when computing time advancement within mesh cells. Following from this, the material derivatives  $D/Dt$  used up to this point are now written as total derivatives  $d/dt$ . Spatial derivatives appearing in heat, mass, momentum, and energy flux terms are evaluated at cell faces using central differences. On a uniform mesh (but not necessarily on the adaptive mesh) the spatial discretization is second order and for cell  $k$  it is written as

$$\left( \frac{d\phi}{dx} \right)_{k+1/2} = \frac{\phi_{k+1} - \phi_k}{x_{k+1} - x_k}. \quad (\text{E.11})$$

The continuity equation, Eq. (E.1), for the  $k^{\text{th}}$  cell can be reformulated to give

$$\frac{d}{dt}(\rho_k \Delta x_k) = 0, \quad \Rightarrow \quad \rho_k \Delta x_k = \text{constant}. \quad (\text{E.12})$$

This shows that, during time advancement of the partial differential equations, the total mass in a given grid cell remains constant. The three components of the momentum equation, Eq. (E.2), are now written for the  $k^{\text{th}}$  cell as

$$\begin{aligned} \frac{d}{dt}(u_{1,k}) &= \frac{1}{\rho_k \Delta x_k} (\sigma_{11,k+1/2} - \sigma_{11,k-1/2}) - \frac{1}{\rho_k} \left( \frac{\partial p}{\partial x} \right)_k, \\ \frac{d}{dt}(u_{2,k}) &= \frac{1}{\rho_k \Delta x_k} (\sigma_{21,k+1/2} - \sigma_{21,k-1/2}), \\ \frac{d}{dt}(u_{3,k}) &= \frac{1}{\rho_k \Delta x_k} (\sigma_{31,k+1/2} - \sigma_{31,k-1/2}). \end{aligned} \quad (\text{E.13})$$

To limit overshoots, the pressure gradient is chosen using the van Leer slope limiter [112]. This gives

$$\left( \frac{\partial p}{\partial x} \right)_k = \text{ave} \left( \frac{p_k - p_{k-1}}{x_k - x_{k-1}}, \frac{p_{k+1} - p_k}{x_{k+1} - x_k} \right), \quad (\text{E.14})$$

where

$$\text{ave}(A, B) \equiv \frac{A + B}{2} \left( 1 - \frac{(A - B)^2}{A^2 + B^2 + C^2} \right), \quad (\text{E.15})$$

and  $C^2$  is a small constant ( $C^2 \ll 1$ ). The balance equations for species mass fractions, Eq. (E.3), and energy, Eq. (E.4), are discretized to obtain

$$\frac{d}{dt}(Y_{s,k}) = -\frac{1}{\rho_k \Delta x_k} (j_{s,k+1/2} - j_{s,k-1/2}) + \frac{\dot{\omega}_{s,k}}{\rho_k}, \quad (\text{E.16})$$

$$\begin{aligned} \frac{d}{dt}(h_k) &= -\frac{1}{\rho_k \Delta x_k} (q_{k+1/2} - q_{k-1/2}) + \frac{1}{\rho_k} \left( \frac{dp}{dt} \right)_k + \\ &\frac{1}{\rho_k \mu_k} \left( \frac{4}{3} \left( \frac{\partial u_1}{\partial x} \right)_{k+1/2}^2 + \left( \frac{\partial u_2}{\partial x} \right)_{k+1/2}^2 + \left( \frac{\partial u_3}{\partial x} \right)_{k+1/2}^2 \right). \end{aligned} \quad (\text{E.17})$$

### E.3 TEMPORAL DISCRETIZATION

Equations (E.2 - E.4) are numerically time advanced using standard first-order finite-difference discretization using an acoustic CFL time-step constraint. The interfaces are fully Lagrangian, therefore the interface position must also be

advanced by the algorithm in conjunction with the changing cell pressures and densities. The cell interface position  $x_{k+1/2}$  satisfies

$$\frac{dx_{k+1/2}}{dt} \equiv u_{1,k+1/2}, \quad (\text{E.18})$$

where the velocity at the cell interface is found by linear interpolation between the velocities of the two neighboring cells:  $u_{1,k+1/2} = \left(\frac{\partial u_1}{\partial x}\right)_{k+1/2} \cdot (x_{k+1/2} - x_k) + u_{1,k}$ . Given the solution at time  $t$ , denoted by superscript  $n$ , the equation for the cell interface at the next time level,  $t + \Delta t$ , denoted by superscript  $n + 1$  is

$$x_{k+1/2}^{n+1} = x_{k+1/2}^n + \Delta t \cdot u_{1,k+1/2}^n. \quad (\text{E.19})$$

From the new cell interface positions, the cell sizes and the cell center positions are updated:

$$\Delta x_k^{n+1} = x_{k+1/2}^{n+1} - x_{k-1/2}^{n+1}; \quad x_k^{n+1} = \frac{x_{k+1/2}^{n+1} + x_{k-1/2}^{n+1}}{2}. \quad (\text{E.20})$$

The pressure update of Eq. (E.9) is solved using operator splitting. This is done because as it will be shown, the first part in Eq. (E.9),  $\gamma p \frac{\partial u_1}{\partial x}$ , can be updated in a conservative manner rather than through standard finite differencing that is performed for the second part in Eq. (E.9),  $\gamma p \Psi$ . The pressure at  $n + 1$  is then the sum of the pressure change due to volume change ( $\widehat{\Delta p}_k$ ), the pressure change due to reaction/diffusion/viscous work ( $\widetilde{\Delta p}_k$ ), and the current pressure

$$p_k^{n+1} = \widehat{\Delta p}_k \Big|_n^{n+1} + \widetilde{\Delta p}_k \Big|_n^{n+1} + p_k^n. \quad (\text{E.21})$$

First, the pressure change due to the second part of Eq. (E.9),  $\gamma p \Psi$ , is found using standard first-order finite differencing, giving

$$\widetilde{\Delta p}_k \Big|_n^{n+1} = \Delta t \cdot \gamma_k^n p_k^n \Psi_k^n. \quad (\text{E.22})$$

Then, the first part of Eq. (E.9),  $\gamma p \frac{\partial u_1}{\partial x}$ , is evaluated in a conservative manner using the assumptions that the gas is an ideal gas and the process is adiabatic and thermodynamically reversible (i.e. infinitesimal changes). Under these assumptions,

$$p V_{cv}^\gamma = \text{constant} \quad \longrightarrow \quad d(p V_{cv}^\gamma) = 0. \quad (\text{E.23})$$

The change in pressure due to a volume change is then

$$\widehat{\Delta p}_k \Big|_n^{n+1} = p_k^n \left( \left( \frac{\Delta x_k^n}{\Delta x_k^{n+1}} \right)^{\gamma_k^n} - 1 \right). \quad (\text{E.24})$$

Although the temporal discretization in Eq. (E.24) is only first-order accurate due to the temporal update of  $\Delta x_k^{n+1}$ , it is a conservative method and is preferred to taking the derivative in the first part of Eq. (E.9). It can now be shown that Eq. (E.23) is equivalent to the first term in Eq. (E.9) by expanding and rearranging Eq. (E.23) to obtain

$$V_{cv}^\gamma \frac{d\widehat{p}}{dt} + p\gamma V_{cv}^{\gamma-1} \frac{dV_{cv}}{dt} = 0 \quad \longrightarrow \quad \frac{d\widehat{p}}{dt} = -p\gamma \frac{\partial u_1}{\partial x}, \quad (\text{E.25})$$

where

$$\frac{1}{V_{cv}} \frac{dV_{cv}}{dt} = \frac{\partial u_1}{\partial x}. \quad (\text{E.26})$$

Similarly, the energy equation, Eq. (E.4), is time advanced in two steps. First, the standard finite-difference step is performed by setting  $\left(\frac{dp}{dt}\right)_k^n = \left(\frac{\widehat{\Delta p}}{\Delta t}\right)_k^n$  to obtain

$$\begin{aligned} \widetilde{\Delta h_k} \Big|_n^{n+1} = \\ \Delta t \cdot \left( -\frac{1}{\rho_k^n} \left( \frac{\partial q}{\partial x} \right)_k^n + \frac{1}{\rho_k^n} \left( \frac{\widehat{\Delta p}}{\Delta t} \right)_k^n + \frac{1}{\rho_k^n} \left( \sigma_{i1} \frac{\partial u_i}{\partial x} \right)_k^n \right), \end{aligned} \quad (\text{E.27})$$

Then, on further manipulation of Eq. (E.23) and making use of the relation  $dh = V_{cv} dp / \rho$  (derived from the 1<sup>st</sup> law of Thermodynamics for an adiabatic process), The change of enthalpy resulting from a volume change is written as

$$dh = -\frac{1}{\rho} p\gamma dV_{cv} \longrightarrow \int_t^{t+\Delta t} dh = -\frac{1}{\rho} (pV_{cv}^\gamma)^\gamma \int_t^{t+\Delta t} \frac{1}{V_{cv}^\gamma} dV_{cv}, \quad (\text{E.28})$$

so that after integrating

$$\widehat{\Delta h_k} \Big|_n^{n+1} = -\frac{p_k^n \Delta x_k^n}{\rho_k^n} \frac{\gamma_k^n}{1-\gamma_k^n} \left( \left( \frac{\Delta x_k^{n+1}}{\Delta x_k^n} \right)^\gamma - 1 \right). \quad (\text{E.29})$$

Finally, solving for the enthalpy at time step  $n + 1$  gives

$$h_k^{n+1} = \widehat{\Delta h_k} \Big|_n^{n+1} + \widetilde{\Delta h_k} \Big|_n^{n+1} + h_k^n. \quad (\text{E.30})$$





The mechanism of turbulence generation by a shock is termed the Richtmyer-Meshkov (RM) instability, analogous to the buoyancy-driven Rayleigh-Taylor (RT) instability and the dilatation-driven Darrieus-Landau (DL) instability. To identify the shock-turbulence-interaction (STI) contribution to the ODT rate expression, it is convenient to start from the general form of the DL contribution,

$$E^{DL} = \int_{x_0}^{x_0+l} \alpha(f(x)) \cdot K(x) \cdot [\rho(f(x)) - \bar{\rho}] dx, \quad (F.1)$$

where  $\bar{\rho}$  is chosen to be the eddy average of  $\rho(f(x))$  so that  $E^{DL}$  vanishes if  $\rho(f(x))$  is uniform in  $x$  within the eddy. In Eq. (F.1),  $\alpha(x)$  and  $\rho(x)$  are based on the post-triplet-map system state, consistent with the convention that the argument  $x$  of  $K$  is the post-map location corresponding to the fluid displacement  $K(x)$ .

DL is the acceleration analog of the gravitational potential energy change induced by a triplet map in a buoyant stratified flow (see Appendix D). Accordingly, it implies an equal and opposite change of the available kinetic energy, so it is subtracted from the available kinetic energy in the rate expression. In the general case involving both spatially distributed dilatations and nominally discontinuous shocks, both the DL contribution and the analogous STI contribution should be included in the rate expression in this manner.

Suppose that a candidate eddy spanning the interval  $[x_1, x_2]$  contains a shock at location  $x_s$  within the eddy interval. (As explained later, the STI contribution analogous to Eq. (F.1) is applied only if the shock passed through the eddy recently but is not presently within the eddy, so the explanation here is only a conceptual illustration. Therefore some of the details here will not apply to the implemented procedure.) Then  $\alpha(f(x))$  is nonzero only at  $x=x_s$ , so the specialization of Eq. (F.1) to the shock-driven case can be written as

$$E^{STI} = K(x_s) \cdot [\rho(f(x_s)) - \bar{\rho}] \cdot \int_{x_1}^{x_2} \alpha(f(x)) dx. \quad (F.2)$$

Evaluation of  $\rho$  at  $x_s$  is ambiguous because  $\rho$  is discontinuous there. This is addressed shortly. Meanwhile consider

$$\int_{x_1}^{x_2} \alpha(f(x)) dx = \int_{x_1}^{x_2} \frac{du_1(f(x))}{dt} dx, \quad (F.3)$$

where the integrand is nonzero only at  $x_s$ , so the integral can be over any interval containing  $x_s$ . Since only the singular shock behavior is considered here,

in practice the integral should be over a small interval  $[x_-, x_+]$  containing  $x_s$  so that only the shock mechanism is represented. Now  $\int_{x_-}^{x_+} \frac{du_1(f(x))}{dt} dx$  is written as  $\frac{d}{dt} \int_{x_-}^{x_+} u_1(f(x)) dx$ . Assume that the shock propagates toward positive  $x$  with velocity  $u_s$ , and that  $u_1 = u_-$  ( $u_+$ ) at  $x$  less (greater) than  $x_s$ . Then  $\frac{d}{dt} \int_{x_-}^{x_+} u_1(f(x)) dx = u_s(u_- - u_+)$ . Substitution of this into Eq. (F.2) gives

$$E^{STI} = u_s \cdot (u_- - u_+) \cdot K(x_s) \cdot [\rho(f(x_s)) - \bar{\rho}]. \quad (F.4)$$

The evaluation of  $\rho(f(x_s))$  is based on the physical consideration that shocks directly generate turbulence only when they encounter pre-existing density variations or jumps. So  $\rho(f(x_s))$  is defined in a way that gives  $E^{STI}=0$  if the density within the eddy interval is uniform on each side of the shock, where those uniform values are denoted  $\rho_-$  and  $\rho_+$ , respectively. Namely, the definition

$$\rho(f(x_s)) = \frac{(f(x_s) - f(x_1))\rho_- + (f(x_2) - f(x_s))\rho_+}{f(x_2) - f(x_1)} \quad (F.5)$$

is adopted, which is equivalent to the definition of  $\bar{\rho}$  for the case of uniformity on each side of the shock. The last factor on the right-hand side of Eq. (F.4) is zero for this case, causing  $E^{STI}$  to be zero, as desired. More generally,  $\rho_-$  and  $\rho_+$  are taken to be density values at locations just behind and just ahead of the shock, respectively, yielding vanishing  $E^{STI}$  in the noted special case, but otherwise  $E^{STI}$  is not forced to vanish.

#### F.1 TIME SCALES

In the limit of infinite speed of sound, there will never be an accepted eddy during the passage of the shock through the domain, so the shock will not affect the flow. This is a case in which the instantaneous eddy map is unphysical, as it makes shocks slow rather than fast relative to eddy processes. Therefore the finite duration of physical eddies needs to be incorporated. To do this, the eddy time scale  $\tau$  times an adjustable coefficient  $\theta_{STI}$  defines an eddy time duration  $t_e$  as  $t_e = \tau \cdot \theta_{STI}$ . A candidate eddy sampled at time  $t$  is deemed to have existed since  $t - t_e$ , so every shock that was in the eddy range during  $[t - t_e, t]$  is deemed to interact with the eddy. Within this framework, the shock is potentially no longer within a sampled eddy interval. The question then arises as to at what location to calculate the  $E^{STI}$  influence on an eddy. The choice is made that for each shock, the shock-eddy interaction is taken to be the average of Eq. (F.4) over  $x_s$  values within the eddy interval, thus

$$E^{STI} = \frac{u_s(u_- - u_+)}{l} \int_{x_0}^{x_0+l} K(x) \cdot [\rho(f(x)) - \bar{\rho}] dx \quad (F.6)$$

where  $\rho(f(x))$  has the same meaning as in Eq. (F.1). Due to the integration of  $a(x)$  over the eddy interval, the distinction between the pre-map and post-map profiles of  $a$  is immaterial here.  $E^{STI}$  is now closer in form to  $E^{DL}$ .  $E^{STI}$

is further modified by taking the absolute value of Eq. (F.6) which has the implication that STI increases the likelihood of turbulence for both L/H and H/L interfaces. This is physically correct and contrary to the DL model that enhances turbulence for L/H and mitigates turbulence for H/L interfaces in accordance with the analogy to RT instability. Additionally, because there is no basis for viewing the shock as an energy source, a tunable coefficient  $C_s$  is introduced. The final form of the STI model is then

$$E^{STI} = C_s \left| \frac{u_s(u_- - u_+)}{l} \int_{x_0}^{x_0+l} K(x) \cdot [\rho(f(x)) - \bar{\rho}] dx \right|. \quad (F.7)$$

This quantity is evaluated for each of the shocks that is deemed to interact with the eddy, and these quantities are then summed to obtain the overall effect of shock interactions with the eddy.

## F.2 EDDY IMPLEMENTATION FOR COMPRESSIBLE FLOW

Since a shock that is currently within an eddy is much less likely than a shock no longer in the eddy but within its range during  $[t - t_e, t]$ , any eddy currently containing a shock can be suppressed with no significant effect on the overall statistics of the STI. This is additionally beneficial from an implementation point of view as it eliminates the need to formulate an eddy implementation that does not involve a triplet map. For an eddy currently containing a shock, such an implementation would be needed because it is unphysical to apply the triplet map to a shock, which would create three daughter shocks.

Coupling eddy implementation to prior shocks allows the possibility that many overlapping eddies in a given region interact with the same shock. This is physical because the instantaneous eddies represent motions at various scales that are in fact simultaneous rather than sequential. In this sense, it is more physical to allow shocks to affect eddy events over a range of future times.

A consequence of this implementation is that shock-induced turbulence will persist for some time period after the passage of the shock, a physically correct result.



## BIBLIOGRAPHY

---

- [1] Assessment of Fuel Economy Technologies for Light-Duty Vehicles. Technical Report ISBN 978-0-309-15607-3, National Research Council, 2011.
- [2] Chemical-Kinetic Mechanism for Combustion Applications. Technical report, San Diego Mechanism web page, Mechanical and Aerospace Engineering (Combustion Research), University of California at San Diego (<http://combustion.ucsd.edu>), 2015.
- [3] M. M. Abbott and H. G. van Ness. *Thermodynamics with chemical applications*. McGraw-Hill, New York, 2nd edition, 1972.
- [4] S. Arrhenius. On the influence of carbonic acid in the air upon the temperature of the ground. *London, Edinburgh, and Dublin Phil. Magazine and J. of Sci.*, 41:237–275, 1896.
- [5] Wm. T. Ashurst and A. R. Kerstein. One-dimensional turbulence: Variable-density formulation and application to mixing layers. *Phys. Fluids*, 17:025107, 2005.
- [6] Wm. T. Ashurst and A. R. Kerstein. Erratum: "One-dimensional turbulence: Variable-density formulation and application to mixing layers". *Phys. Fluids*, 21:119901, 2009.
- [7] P. Atkins. *Four laws that drive the universe*. Oxford University Press, New York, 2007.
- [8] G. K. Batchelor. *An introduction to fluid dynamics*. Cambridge University Press, Cambridge, 1967.
- [9] R. W. Bilger, S. H. Starner, and R. J. Kee. On reduced mechanisms for methane-air combustion in nonpremixed flames. *Combust. Flame*, 80:135–149, 1990.
- [10] R. W. Bilger, S. B. Pope, K. N. C. Bray, and J. F. Driscoll. Paradigms in turbulent combustion research. *Proc. Combust. Inst.*, 30:21–42, 2005.
- [11] M. Brouillette. The Richtmyer-Meshkov Instability. *Annu. Rev. Fluid Mech.*, 34:445–468, 2002.
- [12] M. Brouillette and B. Sturtevant. Experiments on the Richtmyer-Meshkov instability: single-scale perturbations on a continuous interface. *J. Fluid Mech.*, 263:271–292, 1994.
- [13] S. Cao and T. Echehki. A low-dimensional stochastic closure model for combustion large-eddy simulation. *J. Turbul.*, 9:1–35, 2008.

- [14] D. L. Chapman. On the rate of explosion in gases. *Philos. Mag.*, 47: 90–104, 1899.
- [15] G. Ciccarelli and S. Dorofeev. Flame acceleration and transition to detonation in ducts. *Prog. Energy Combust. Sci.*, 34:499–550, 2008.
- [16] C. Clanet and G. Searby. First experimental study of the Darrieus-Landau instability. *APS: Physical Review Letters*, 80:3867–3870, 1998.
- [17] P. Clavin. Dynamic Behavior of Premixed Flame Fronts in Laminar and Turbulent Flows. *Prog. Energy Combust. Sci.*, 11:1–59, 1985.
- [18] G. Coppola, B. Coriton, and A. Gomez. Highly turbulent counterflow flames: A laboratory scale benchmark for practical systems. *Int. Geophysics*, 101:3–39, 2013.
- [19] B. Coriton. *Highly turbulent counterflow premixed flames in the flamelet and non-flamelet regimes*. PhD thesis, Yale University, New Haven, 2010.
- [20] N. Darabiha, S. M. Candel, V. Giovangigli, and M. D. Smooke. Extinction of strained premixed propane-air flames with complex chemistry. *Combust. Sci. and Tech.*, 60:267–285, 1988.
- [21] G. Darrieus. Unpublished work presented at La Technique Moderne, and at Le Congrès de Mécanique Appliquée (1945) and (1938).
- [22] W. Davis and C. Fauquignon. Classical Theory of Detonation. *J. de Physique IV*, C4:3–21, 1995.
- [23] B. Denet and P. Haldenwang. A numerical study of premixed flames: Darrieus-Landau instability. *Combust. Sci. and Tech.*, 104:143–167, 1995.
- [24] K. Devlin. *The Millennium Problems: The Seven Greatest Unsolved Mathematical Puzzles of Our Time*. Basic Books, 2002.
- [25] W. Döring. On the detonation process in gases. *Ann. Phys.*, 43:421–436, 1943.
- [26] A. N. Dremin. *Toward Detonation Theory*. Springer, New York, 1999.
- [27] T. Echekki, A. R. Kerstein, and T. D. Dreeben. One-dimensional turbulence simulation of turbulent jet diffusion flames: Model formulation and illustrative applications. *Combust. Flame*, 125:1083–1105, 2001.
- [28] F. E. Fendell. Ignition and extinction in combustion of initially unmixed reactants. *J. Fluid Mech.*, 21:281–303, 1965.
- [29] L. Y. M. Gicquel, G. Staffelbach, and T. Poinso. Large Eddy Simulations of gaseous flames in gas turbine combustion chambers. *Prog. Energy Combust. Sci.*, 38:782–817, 2012.

- [30] V. Giovangigli and M. D. Smoke. Extinction of strained premixed laminar flames with complex chemistry. *Combust. Sci. Tech.*, 53:23–49, 1987.
- [31] C. Glawe, H. Schmidt, A. R. Kerstein, and R. Klein. XLES Part I: Introduction to Extended Large Eddy Simulation. *submitted to J. Comput. Phys.*, 2015.
- [32] C. Glawe, H. Schmidt, A. R. Kerstein, and R. Klein. XLES Part II: From Extended Large Eddy Simulation to ODTLES. *submitted to J. Comput. Phys.*, 2015.
- [33] C. Glawe, F. T. Schulz, E. D. Gonzalez-Juez, H. Schmidt, and A. R. Kerstein. ODTLES simulations of turbulent flows through heated channels and ducts. In *8th Symposium on Turbulence and Shear Flow Phenomena, Poitiers, France*, pages 1–6, August 28 - 30 2013.
- [34] E. D. Gonzalez-Juez, R. C. Schmidt, and A. R. Kerstein. ODTLES simulation of wall-bounded turbulent flows. *Phys. of Fluids*, 23:125102, 2011.
- [35] E. D. Gonzalez-Juez, A. R. Kerstein, and D. O. Lignell. Reactive Rayleigh-Taylor turbulent mixing: A one-dimensional-turbulence study. *Geophys. Astrophys. Fluid Dyn.*, 107:506–525, 2013.
- [36] D. Goodwin. CANTERA: Object-oriented software for reacting flows. <http://www.cantera.org>.
- [37] J. C. Hewson and A. R. Kerstein. Stochastic simulation of transport and chemical kinetics in turbulent CO/H<sub>2</sub>/N<sub>2</sub> flames. *Combust. Theory Model.*, 5:669–697, 2001.
- [38] J. C. Hewson and A. R. Kerstein. Local extinction and reignition in nonpremixed turbulent CO/H<sub>2</sub>/N<sub>2</sub> jet flames. *Combust. Sci. Technol.*, 174:35–66, 2002.
- [39] D. J. Hill, C. Pantano, and D. I. Pullin. Large-eddy simulation and multiscale modelling of a Richtmyer-Meshkov instability with reshock. *J. Fluid Mech.*, 557:29–61, 2006.
- [40] A. C. Hindmarsh. SUNDIALS: Suite of nonlinear and differential/algebraic equation solvers. Technical Report UCRL-JRNL-200037, Lawrence Livermore National Laboratory, 2004.
- [41] E. Jouguet. On the propagation of chemical reactions in gases. *J. Math. Pures Appl.*, 6:347–425, 1905.
- [42] Z. Jozefik, A. R. Kerstein, H. Schmidt, S. Lyra, H. Kolla, and J. H. Chen. One-dimensional turbulence modeling of a turbulent counterflow flame with comparison to DNS. *Combust. Flame*, 162:2999–3015, 2015.
- [43] Z. Jozefik, A. R. Kerstein, and H. Schmidt. Simulation of shock-turbulence interaction in non-reactive flow and in turbulent deflagration and detonation regimes using one-dimensional turbulence. *Combust. Flame*, 164:53–67, 2016.

- [44] Z. Jozefik, A. R. Kerstein, and H. Schmidt. Towards a compressible reactive multiscale approach based on One-Dimensional Turbulence. In *Papers Contributed to the Conference "Active Flow and Combustion Control 2014", Berlin, Germany*. Springer series Notes on Numerical Fluid Mechanics and Multidisciplinary Design, September 10 - 12 2014.
- [45] A. R. Kerstein. Linear-eddy modeling of turbulent transport. II: Application to shear layer mixing. *Combust. Flame*, 75:397–413, 1989.
- [46] A. R. Kerstein. Linear-eddy model of turbulent transport. part 4. structure of diffusion flames. *Combustion Science and Technology*, 81:75–96, 1992.
- [47] A. R. Kerstein. Linear-eddy model of turbulent transport. part 7. finite-rate chemistry and multi-stream mixing. *J. Fluid Mech.*, 240:289–313, 1992.
- [48] A. R. Kerstein. One-dimensional turbulence: Model formulation and application to homogeneous turbulence, shear flows, and buoyant stratified flows. *J. Fluid Mech.*, 392:277–334, 1999.
- [49] A. R. Kerstein and S. Wunsch. Simulation of a stably stratified atmospheric boundary layer using one-dimensional turbulence. *Bound.-Lay. Meteorol.*, 118:325–356, 2006.
- [50] A. R. Kerstein, Wm. T. Ashurst, S. Wunsch, and V. Nilsen. One-dimensional turbulence: Vector formulation and application to free shear flows. *J. Fluid Mech.*, 447:85–109, 2001.
- [51] A. M. Khokhlov and E. S. Oran. Numerical Simulation of Detonation Initiation in a Flame Brush: The Role of Hot Spots. *Combust. Flame*, 119:400–416, 1999.
- [52] A. M. Khokhlov, E. S. Oran, A. Y. Chtehelkanova, and J. C. Wheeler. Interaction of a shock with a sinusoidally perturbed flame. *Combust. Flame*, 117:99–116, 1999.
- [53] A. M. Khokhlov, E. S. Oran, and G. O. Thomas. Numerical Simulation of Deflagration-to-Detonation Transition: The Role of Shock-Flame Interactions in Turbulent Flames. *Combust. Flame*, 117:323–339, 1999.
- [54] G. G. Kleinstein. A note on Taylor's stability rule. *Acta Mech*, 219:371–373, 2011.
- [55] A. N. Kolmogorov. Dissipation of energy in the locally isotropic turbulence. *C.R. Acad. Sci. USSR*, 32:16–18, 1941.
- [56] A. N. Kolmogorov. The local structure of turbulence in incompressible viscous fluids for very large Reynolds numbers. *Dok. Akad. Nauk. USSR*, 30:301–305, 1941.



- [57] N. Krishnamoorthy. *Reaction models and reaction state parameterization for turbulent nonpremixed combustion*. PhD thesis, University of Utah, Salt Lake City, 2008.
- [58] P. K. Kundu and I. M. Cohen. *Fluid Mechanics*. Elsevier Inc., Oxford, 4th edition, 2008.
- [59] L. Landau. *Acta Phys. Chim. USSR*, 19:77–85, 1994.
- [60] C. K. Law and C. J. Sung. Structure, aerodynamics, and geometry of premixed flamelets. *Prog. Energy Combust. Sci.*, 26:459–505, 2000.
- [61] J. Li, Z. Zhao, A. Kazakov, and F. L. Dryer. An updated comprehensive kinetic model of hydrogen combustion. *Int. J. Chem. Kinet.*, 36:566–575, 2004.
- [62] P. A. Libby. Recent research on premixed flames in stagnating turbulence. *Combust. Sci. and Tech.*, 177:1073–1094, 2005.
- [63] M. A. Liberman. Flame, detonation, explosion- when, where and how they occur. In *3rd international disposal conference*. Karlskoga, Sweden, 2003.
- [64] M. A. Liberman. *Introduction to Physics and Chemistry of Combustion*. Springer, Berlin, 2008.
- [65] D. O. Lignell and D. S. Rappleye. One-dimensional turbulence simulation of flame extinction and reignition in planar ethylene jet flames. *Combust. Flame*, 159:2930–2943, 2012.
- [66] D. O. Lignell, A. R. Kerstein, G. Sun, and E. E. Monson. Mesh adaption for efficient multiscale implementation of one-dimensional turbulence. *Theor. Comput. Fluid Dyn.*, 27:273–295, 2013.
- [67] A. Liñán. The asymptotic structure of counterflow diffusion flames for large activation energies. *Acta Astronautica*, 1:1007–1039, 1974.
- [68] J. D. Lindl. *Inertial confinement fusion*. Springer-Verlag, NY, 1998.
- [69] Y. Liu, Y. Q. Chen, J. G. Chen, and R. Yang. *Computational Methods in Engineering and Science*. Springer, Berlin Heidelberg, 2007.
- [70] A. E. Lutz, R. J. Kee, J. F. Grcar, and F. M. Rupley. OPPDIF: A Fortran program for computing opposed-flow diffusion flames. *Sandia National Laboratories Report 96-8243*, 1996.
- [71] S. Lyra, H. Kolla, B. Coriton, J. H. Frank, and J. H. Chen. Counterflow H<sub>2</sub>/air premixed flames under intense turbulence and strain. *submitted to Flow Turb. Combust.*, 2013.
- [72] E. Mallard and H. L. LeChatelier. On the flame propagation velocity in explosive gas mixtures. *Acad. Sci. Comptes Rendus Math.*, 93:145–148, 1881.

- [73] F. E. Marble, G. J. Hendricks, and E. E. Zukoski. Progress towards shock enhancement of supersonic combustion process. *AIAA J.*, 87:1880–1888, 1987.
- [74] G. H. Markstein. Flow disturbances induced near a slightly wavy contact surface, or flame front, traversed by a shock wave. *J. Aero. Sci.*, 24:238–239, 1957.
- [75] R. J. McDermott. *Toward one-dimensional turbulence subgrid closure for large-eddy simulation*. PhD thesis, University of Utah, Salt Lake City, 2008.
- [76] P. A. McMurtry, S. Menon, and A. R. Kerstein. A linear eddy sub-grid model for turbulent reacting flows: applications to hydrogen-air combustion. *Proc. Combust. Inst.*, 24:271–278, 1992.
- [77] G. B. Meir. *Fundamentals of Compressible Fluid Mechanics*. Genick Bar-Meir, Minneapolis, 2006.
- [78] M. R. Meloon. *Models of Richtmyer-Meshkov Instability in Continuously stratified fluids*. PhD thesis, California Institute of Technology, Pasadena, 1998.
- [79] E. E. Meshkov. Instability of the interface of two gases accelerated by a shock wave. *Izv. AN SSSR. Mekhanika Zhidkosti i Gaza*, 4:151–157, 1969.
- [80] E. I. Monson, D. O. Lignell, M. A. Finney, C. Werner, Z. Jozefik, A. R. Kerstein, and R. S. Hintze. Simulation of ethylene wall fires using the spatially-evolving one-dimensional turbulence model. In *Fire Technology, Special Issue on Validation and Fire Modelling*, 2014. doi:10.1007/s10694-014-0441-2.
- [81] Q. Ni, Y. Shi, and S. Chen. Statistics of one-dimensional compressible turbulence with random large-scale force. *Phys. of Fluids*, 25:075106, 2013.
- [82] E. S. Oran and F. A. Williams. The physics, chemistry and dynamics of explosions. *Phil. Trans. R. Soc.*, 370:534–543, 2013.
- [83] T. Passot and A. Pouquet. Numerical simulation of compressible homogeneous flows in the turbulent regime. *J. Fluid Mech*, 118:441–466, 1987.
- [84] N. Peters. The turbulent burning velocity for large scale and small scale turbulence. *J. Fluid Mech*, 384:107–32, 1999.
- [85] N. Peters. *Turbulent Combustion*. Cambridge University Press, Cambridge, 2000.
- [86] T. Poinso and D. Veynante. *Theoretical and Numerical Combustion*. T. Poinso and D. Veynante, Toulouse, 3rd edition, 2011.

- [87] T. Poinso, S. Candel, and A. Trouvé. Application of direct numerical simulation to premixed turbulent combustion. *Prog. Energy Comb. Sci.*, 21:531–576, 1996.
- [88] T. Poinso, T. Kestens, and F. Nicoud. Using computational fluid dynamics to study flow control. *Comput. Meth. Cont. Appl.*, 16:327–46, 2002.
- [89] S. B. Pope. *Turbulent Flows*. Cambridge University Press, Cambridge, 2000.
- [90] S. B. Pope. Small scales, many species and the manifold challenges of turbulent combustion. *Proc. Combust. Inst.*, 32:1–31, 2013.
- [91] N. Punati, J. C. Sutherland, A. R. Kerstein, E. R. Hawkes, and J. H. Chen. An evaluation of the one-dimensional turbulence model: Comparison with direct numerical simulations of CO/H<sub>2</sub> jets with extinction and reignition. *Proc. Combust. Inst.*, 33:1515–1522, 2011.
- [92] B. Ranganath and T. Echekeki. One-dimensional turbulence-based closure with extinction and reignition. *Combust. Flame*, 154:23–46, 1981.
- [93] B. Ranganath and T. Echekeki. An ODT-based closure model in non-premixed combustion. *Prog. Comput. Fluid Dynam.*, 6:409–418, 2006.
- [94] L. Rayleigh. *Investigation of the character of the equilibrium of an incompressible heavy fluid of variable density*, volume 2. Dover, New York, 1900.
- [95] R. D. Reitz. Directions in internal combustion engine research. *Combust. Flame*, 160:1–8, 2013.
- [96] P. H. Renard, D. Thévenin, J. C. Rolon, and S. Candel. Dynamics of flame/vortex interactions. *Prog. Energy Combust. Sci.*, 26:225–282, 2000.
- [97] R. D. Richtmyer. Taylor instability in shock acceleration of compressible fluids. *Comm. Pure Appl. Math*, 13:297–319, 1960.
- [98] R. S. Rogallo. Numerical experiments in homogeneous turbulence. *NASA Technical Memorandum 81315*, NASA Ames Research Center, CA, USA.
- [99] B. Rogg. Response and flamelet structure of stretched premixed methane-air flames. *Combust. Flame*, 73:45–65, 1988.
- [100] B. Rogg and N. Peters. The asymptotic structure of weakly strained stoichiometric methane-air flames. *Combust. Flame*, 79:402–420, 1999.
- [101] A. L. Sánchez, A. Lépinette, M. Bollig, L. Liñán, and B. Lázaro. The reduced kinetic description of lean premixed combustion. *Combust. Flame*, 123:436–464, 2000.

- [102] R. F. Sawyer. Science based policy for addressing energy and environmental problems. *Combust. Flame*, 30:45–56, 2009.
- [103] R. C. Schmidt, A. R. Kerstein, S. Wunsch, and V. Nilsen. Near-wall LES closure based on one-dimensional turbulence modeling. *J. Comp. Phys.*, 186:317–355, 2003.
- [104] R. C. Schmidt, A. R. Kerstein, and R. J. McDermott. ODT: A multi-scale model for 3D turbulent flow based on one-dimensional turbulence modeling. *Comput. Methods Appl. Mech. Eng.*, 199:865–880, 2010.
- [105] K. Seshadri and N. Peters. The influence of stretch on a premixed flame with two-step kinetics. *Combust. Sci. Tech.*, 61:1–42, 1983.
- [106] L. Smarr, J. R. Wilson, R. T. Barton, and R. L. Bowers. Rayleigh-Taylor overturn in supernova core collapse. *Astrophys. J.*, 246:515–525, 1975.
- [107] L. K. Su and N. T. Clemens. Measurements of the three-dimensional scalar dissipation rate field in gas phase planar turbulent jets. *AIAA 97-0074, 35th Aerospace Sciences Meeting, 1997*.
- [108] M. S. Sweeney, S. Hochgreb, M. J. Dunn, and R. S. Barlow. The structure of turbulent stratified and premixed methane/air flames I: Non-swirling flows. *Combust. Flame*, 159:2896–2911, 2012.
- [109] M. S. Sweeney, S. Hochgreb, M. J. Dunn, and R. S. Barlow. The structure of turbulent stratified and premixed methane/air flames II: Non-swirling flows. *Combust. Flame*, 159:2912–2929, 2012.
- [110] G. I. Taylor. The instability of liquid surfaces when accelerated in a direction perpendicular to their planes. *I. Proc. R. Soc. London Ser. A*, 201:192–196, 1950.
- [111] D. M. Valiev, C. K. Law, and J. H. Chen. Turbulence-affected Darrieus-Landau Instability. In *8th US National Combustion Meeting*. Western States Section of the Combustion Institute, May 19-22 2013.
- [112] B. van Leer. On the relation between the upwind-differencing schemes of Godunov, Engquist-Osher and Roe. *SIAM J. Sci. Stat. Comput.*, 5: 1–20, 1984.
- [113] M. Vetter and B. Sturtevant. Experiments on the Richtmyer-Meshkov instability of an air/SF<sub>6</sub> interface. *Shock Waves*, 4:247–252, 1995.
- [114] R. von Mises. *Mathematical Theory of Compressible Fluid Flow*. Academic Press Inc., New York, 1958.
- [115] J. von Neumann. Theory of detonation waves. *Office of Scientific Research and Development (OSRD), Washington, DC.*, Report no. 549, Progress Report no. 238, 1942.

- [116] I. A. Waitz, F. E. Marble, and E. E. Zukoski. An investigation of a contoured wall injector for hypervelocity mixing augmentation. *AIAA J.*, 91:2265–2284, 1991.
- [117] D. C. Wilcox. *Turbulence Modeling for CFD*. DCW Industries, Inc, CA, 2nd edition, 2000.
- [118] F. A. Williams. *Combustion Theory*. Perseus Books, 2nd edition, 1985.
- [119] F. A. Williams. The next 25 years of combustion theory. *Combust. Sci. Technol.*, 98:361–366, 1994.
- [120] F. A. Williams. Progress in knowledge of flamelet structure and extinction. *Prog. Energy Combust. Sci.*, 26:657–682, 2000.
- [121] S. Wunsch and A. R. Kerstein. A stochastic model for high-Rayleigh-number convection. *J. Fluid Mech.*, 528:173–205, 2005.
- [122] C. S. Yoo, J. H. Chen, and R. Sankaran. Direct numerical simulation of a turbulent lifted hydrogen/air jet flame in heated coflow. In *Computational Combustion, 2007 ECCOMAS Thematic Conference*.
- [123] Ya. B. Zel'dovich. On the theory of the propagation of detonation in gaseous systems. *J. Exp. Theor. Phys.*, 10:542–568, 1940.
- [124] Ya. B. Zel'dovich and Yu. P. Raizer. *Physics of Shock Waves and High-Temperature Hydrodynamic Phenomena*. Dover Publications, Inc., New York, 2002.
- [125] Ya. B. Zel'dovich, V. B. Librovich, G. M. Makhviladze, and G. I. Sivashinsky. Development of Detonation In a Non-Uniformly Preheated Gas. *Astron. Acta*, 15:313–321, 1970.
- [126] R. D. Zucker and O. Biblarz. *Fundamentals of gas dynamics*. John Wiley and Sons, Inc., Hoboken, 2nd edition, 2002.



## DECLARATION

---

I hereby certify that this thesis has been composed by me and is based on my own work, unless stated otherwise. No other person's work has been used without due acknowledgement in this thesis. All references and verbatim extracts have been quoted, and all sources of information, including graphs and data sets, have been specifically acknowledged.

Hiermit erkläre ich an Eides statt, dass ich die vorliegende Arbeit selbstständig und nur unter Zuhilfenahme der ausgewiesenen Hilfsmittel angefertigt habe. Sämtliche Stellen der Arbeit, die im Wortlaut oder dem Sinn nach anderen gedruckten oder im Internet verfügbaren Werken entnommen sind, habe ich durch genaue Quellenangaben kenntlich gemacht.

*Cottbus, May 2016*

---

MSc Zoltan Jozefik





#### COLOPHON

This document was typeset using the typographical look-and-feel `classicthesis` developed by André Miede. The style was inspired by Robert Bringhurst's seminal book on typography "*The Elements of Typographic Style*". `classicthesis` is available for both  $\text{\LaTeX}$  and  $\text{\LyX}$ :

<http://code.google.com/p/classicthesis/>

Happy users of `classicthesis` usually send a real postcard to the author, a collection of postcards received so far is featured here:

<http://postcards.miede.de/>